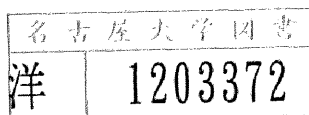


The Global Value of the Hubble Constant
by Observations of Sunyaev-Zel'dovich
Clusters of Galaxies with *ASCA*

Akihiro Furuzawa

Department of Astrophysics, School of Science, Nagoya University

November, 1996



Abstract

Cluster of galaxies is the largest gravitational bound system in the universe and the brightest X-ray emitter. From the velocity dispersion of member galaxies in clusters, it has been clear that clusters contain the large amount of invisible mass, so called 'dark matter', which is about ten times larger than the visible mass. Since the intracluster medium is dissipative, contrary to galaxies in the cluster, the observation of the intracluster medium by X-ray is useful tool to investigate the gravitational mass and dark matter distribution and hence to understand the large scale structure of the universe.

The observation of clusters of galaxies has another importance for the cosmology. This is the observational and traditional approach for cosmology, 'the Hubble constant measurement'. The Hubble constant determines both the expansion timescale and the size of the universe. However, in spite of the fundamental parameter of the cosmology, the measured values are dispersed within factor 2; $50 \text{ km sec}^{-1} \text{ Mpc}^{-1} \sim 100 \text{ km sec}^{-1} \text{ Mpc}^{-1}$. This dispersion has been caused by the various uncertainty; peculiar motion, absolute magnitude of standard candles, the calibration of 'distance ladder' method, underlying physical process and so on.

The derivation from the X-ray and radio cluster observation using the Sunyaev-Zel'dovich effect has advantages; small uncertainty of peculiar motion, clear underlying physical process. Furthermore, the distance to the cluster at the cosmological distance is available.

We analyzed 6 distant clusters of galaxies observed with *ASCA* and obtained accurate averaged temperatures and luminosities. Furthermore, we developed the method of the image analysis using the β model fitting in 2 energy bands including the effect of the XRT PSF, and obtained the structural parameters (θ_c, β) for each cluster.

Using the complete radio data of the Sunyaev-Zel'dovich effect obtained with OVRO 40m single-dish radiometer and X-ray data obtained with only *ASCA* we obtained the 'global' value of the Hubble constant in the universe to be $68 \pm 22 \text{ km sec}^{-1} \text{ Mpc}^{-1}$ from the distances of the clusters of galaxies, A2218, A665 and Cl0016+16 in the redshift range from 0.17 to 0.54 (597 Mpc – 1.3 Gpc assuming $H_0 = 68 \text{ km sec}^{-1} \text{ Mpc}^{-1}$).

It is the first time that the temperature, X-ray flux and the spatially distribution of temperature and density obtained with single mission are used for the Hubble constant determination.

Contents

1	Introduction	1
2	Overview of Clusters of Galaxies	3
2.1	Definision and Classification	3
2.1.1	Catalogue	3
2.1.2	Morphological classification	4
2.2	Optical observation – Galaxy distribution	4
2.3	X-ray observation	6
2.4	Physical process of Clusters of Galaxies observed in the X-ray band	10
2.4.1	Emission mechanism	10
2.4.2	ICM Dynamics	11
2.5	Evolution and Cosmology	12
3	Hubble Constant	14
3.1	What is the Hubble Constant?	14
3.2	Cosmological model	15
3.3	Distance	18
3.4	Review of derivation methods	18
3.5	Sunyaev-Zel’dovich effect	20
3.5.1	Outline	20
3.5.2	Previous results	21
4	<i>ASCA</i> satellite	23
4.1	Overview	23
4.2	Gas Imaging Spectrometer (GIS)	25
4.2.1	Overview	25
4.2.2	Structures and X-ray Detection Mechanism	25
4.2.3	Background Rejection	25
4.2.4	Observation Mode	26
4.2.5	Effective Area of XRT/GIS	26

4.2.6	Gain Corrections	27
4.3	Solid-state Imaging Spectrometer (SIS)	30
4.3.1	Overview	30
4.3.2	Structure and X-ray Detection Mechanism	30
4.3.3	Observation Mode	31
4.3.4	Hot Pixels	33
4.3.5	Echo	34
4.3.6	Dark Frame Error	34
4.3.7	Corrections	34
4.3.8	Light leakage	34
4.4	XRT	35
4.4.1	X-ray reflector and telescope	36
4.4.2	Structure of <i>ASCA</i> XRT	39
4.4.3	XRT calibration	41
5	Analysis of X-ray emission from Clusters of Galaxies	55
5.1	Data reduction	55
5.2	Spectral analysis	56
5.3	Image analysis	58
6	Results of <i>ASCA</i> data analysis of the individual targets	61
6.1	CL0016+16	62
6.1.1	Introduction	62
6.1.2	Observation	62
6.1.3	Results	63
6.1.4	Discussion	64
6.2	A773	69
6.2.1	Introduction	69
6.2.2	Observation	69
6.2.3	Results	69
6.2.4	Discussion	70
6.3	A665	78
6.3.1	Introduction	78
6.3.2	<i>ASCA</i> Observation	78
6.3.3	Results	79
6.3.4	Discussion	80
6.4	A2218	85
6.4.1	Introduction	85
6.4.2	Observation	85

6.4.3	Results	85
6.4.4	Discussion	86
6.5	A1204	92
6.5.1	Introduction	92
6.5.2	Observation	92
6.5.3	Results	92
6.5.4	Discussion	93
6.6	A1413	98
6.6.1	Introduction	98
6.6.2	Observation	98
6.6.3	Results	98
6.6.4	Discussion	99
6.7	Fe-K line analysis – $K\alpha/K\beta$ ratio anomaly ?	105
6.7.1	Introduction	105
6.7.2	Analysis & Results	105
6.7.3	Discussion	107
6.7.4	Summery	107
7	Implication for the Hubble constant	115
7.1	Derivation of H_0	115
7.2	X-ray data	117
7.3	Radio data	119
7.4	Results	120
7.4.1	H_0 determination with the published (θ_c, β) and <i>ASCA</i> C_X	120
7.4.2	H_0 determination with complete data set of our results of Pr , C_X and ΔT_r	121
8	Discussion	125
8.1	Source of the uncertainty	125
8.1.1	Off-axis angle uncertainty (Positional uncertainty of the optical axis)	125
8.1.2	Density and temperature distribution uncertainty	126
8.2	Summary of the derived H_0	128
8.3	Difference from other methods	129
8.3.1	Systematic error in the S-Z effect	130
8.3.2	Systematic error in the distance measurement to Virgo cluster	130
8.3.3	Local and Global value of the Hubble constant	131
8.3.4	Dependence on the cosmological model (Ω_0 q_0)	132
9	Conclusion	133

List of Tables

2.1	Rood-Sastry morphological class	5
2.2	Bautz-Morgan morphological class	5
2.3	Correlation between Rood-Sastry and Bautz-Morgan morphological class	5
2.4	Frequencies of cluster morphological classes	8
3.1	Characteristics of Friedman universe	17
4.1	Time resolution and maximum transferable source intensity of the GIS	26
4.2	Parameters of XRTs in various mission	36
4.3	Off-axis angle of the targets for 'Horn' tuning	45
4.4	Off-axis angle of Cyg X-1 observations for 2nd tuning	48
5.1	Adopted Integration radius (Assuming $H_0 = 50$ and $q_0 = 0$)	56
5.2	Software and Files for data analysis	60
6.1	ICM temperature and X-ray flux of Cl0016+16	65
6.2	Results of Spectral fitting for A773 (N_H fixed)	71
6.3	Results of Spectral fitting for A773 (N_H free)	71
6.4	Spectral fitting result for A665(Integration radius dependence)	80
6.5	A2218 spectral fitting result (Integration radius dependence)	90
6.6	Spectral fit results	93
6.7	Fitting result (Integration radius dependence)	100
6.8	Intensity ratio of He-like $K\alpha$ to H-like $K\alpha$	109
6.9	Intensity ratio of $K\alpha$ line to $K\beta$ line	109
6.10	Effective exposure time and counting rate for each cluster	114
7.1	<i>ASCA</i> X-ray data and C_X , Pr for H_0 determination	118
7.2	Radio Telescopes for S-Z detection	119
7.3	Derived central decrement of the brightness temperature	120
7.4	The Hubble constants obtained with published (θ_c, β)	121
7.5	Hubble constants obtained with our best-fit (θ_c, β)	122
8.1	Computed averaged temperature with the temperature gradient	128

List of Figures

2.1	Examples of the X-ray morphology of several clusters in the classification scheme. Contours show the X-ray surface brightness and are superpose on optical images of the clusters.	9
3.1	The scale factor $R(t)$ of the Friedman universe	17
3.2	The change of the spectrum of blackbody radiation due to scattering by hot Maxwellian electrons	22
3.3	The frequency dependence of thermal S-Z effect and kinematic effect	22
4.1	Appearance of <i>ASCA</i> in orbit	24
4.2	Configuration of instruments	24
4.3	Cross section of the GIS	27
4.4	Schematic view of the GIS system	28
4.5	Quantum efficiency of GIS and Effective area of the XRT + GIS	29
4.6	Cross section of the SIS	30
4.7	Quantum efficiency of the SIS	31
4.8	Top view of SIS chips	32
4.9	Grade definition	33
4.10	Effective Area of XRTs in various mission	35
4.11	Wolter Type system	38
4.12	Schematic view of the XRT	38
4.13	<i>ASCA</i> XRT	40
4.14	Image of point source	41
4.15	The Crab spectrum fitting	44
4.16	GROJ1008 inage and simulation for 'Horn' tuning	46
4.17	Radial profile of GROJ1008 after 'Horn' tuning	47
4.18	Radial profile of Cyg X-1 position 0 and simulation before 2nd tuning	49
4.19	Radial profile of Cyg X-1 position 4 and simulation before 2nd tuning	50
4.20	Radial profile of Cyg X-1 position 0 and simulation after 2nd tuning	51
4.21	Radial profile of Cyg X-1 position 4 and simulation after 2nd tuning	52
4.22	Radial profile of Cyg X-1 position 5 and simulation after 2nd tuning	53

4.23	Radial profile of 3C273 obtained by SIS0 and simulation after 2nd tuning .	54
6.1	CL0016+16 spectrum. Top: GIS, Bottom: SIS	66
6.2	CL0016+16 X-ray brightness contour map	67
6.3	Radial profile of the observed surface brightness for CL0016+16 by SIS0. Solid line is the simulated profile with the bestfit parameters of β model. The Dashed line shows the expected radial profile for a point source. . . .	68
6.4	Confidence level contours for (θ_c, β) obtained by the β model fitting to the SIS0 radial profile. 90% and 99% confidence level contours and the bestfit values obtained by <i>ASCA</i> (cross), <i>ROSAT</i> (box) and <i>Einstein</i> (triangle) are plotted.	68
6.5	A773 spectra. Top: GIS, Bottom: SIS	72
6.6	A773 X-ray brightness contour map	73
6.7	A773 Radial profile (S0)	74
6.8	Confidence level contours for (θ_c, β) obtained by the β model fitting to the SIS0 radial profile. The background level is 0.05 cts/pixel which is averaged from various observations of distant clusters. 90% and 99% confidence level contours and the bestfit values obtained by <i>ASCA</i> (cross). Top:0.5-2.5keV, Bottom:2.5-10keV	75
6.9	Confidence level contours for (θ_c, β) obtained by the β model fitting to the SIS0 0.5-2.5 keV radial profile with different background level. The bestfit values obtained by <i>ASCA</i> (cross). Top: background level = 0.03 cts/pixel, Bottom: background level = 0.07 cts/pixel	76
6.10	Radial dependence of the hardness ratio (2.5-10 keV)/(0.5-2.5 keV).	77
6.11	A665 spectra. Top:GIS, Bottom:SIS	81
6.12	A665 X-ray brightness contour	82
6.13	A665 Radial profile (S0)	83
6.14	Confidence level contours for (θ_c, β) obtained by the β model fitting to the SIS0 radial profile. 90% and 99% confidence level contours and the bestfit values obtained by <i>ASCA</i> (cross). Top:0.5-2.5keV, Bottom:2.5-10keV	84
6.15	A2218 spectra	87
6.16	A2218 X-ray brightness contour map placed on the optical image	88
6.17	A2218 azimuthal averaged radial profile (S0)	89
6.18	Confidence level contours for (θ_c, β) obtained by the β model fitting to the SIS0 radial profile. 90% and 99% confidence level contours and the bestfit values obtained by <i>ASCA</i> (cross). Top:0.5-2.5keV, Bottom:2.5-10keV	91
6.19	A1204 Spectrum Top: GIS, Bottom: SIS	94
6.20	A1204 X-ray brightness contour	95
6.21	Confidence level contours for (θ_c, β) obtained by the β model fitting	96

6.22	Radial dependence of hardness ratio	97
6.23	A1413 spectra. Top:GIS, Bottom:SIS	101
6.24	A1413 X-ray image. The background is not subtracted. Top:GIS, Bottom:SIS	102
6.25	A1413 Radial profile (S0)	103
6.26	Confidence level contours for (θ_c, β) obtained by the β model fitting to the SIS0 radial profile. 90% and 99% confidence level contours and the bestfit values obtained by <i>ASCA</i> (cross). Top:0.5-2.5keV, Bottom:2.5-10keV	104
6.27	A665 spectra around iron K line energy	110
6.28	A1413 spectra around iron K line energy	111
6.29	A1689 spectra around iron K line energy	112
6.30	Simulated integration radius dependence of the intensity ratio	113
7.1	(θ_c, β) dependence of Pr	118
7.2	(θ, β) dependence of ΔT_r for OVRO40 data. Top: Cl0016+16, Middle: A665, Bottom: A2218	123
7.3	(θ, β) dependence of Pr' for OVRO40 data. Top: Cl0016+16, Middle: A665, Bottom: A2218	124
8.1	Summary of the derived H_0	129
8.2	Apparent distance dependence of the Hubble constant due to the use of different cosmological model.	132

Chapter 1

Introduction

Since the earth's atmosphere is highly opaque for X-ray, observations of celestial X-ray sources must be carried out above most of the atmosphere. The first detection of the celestial X-ray emission from the sun was in 1949 by the sounding rocket experiment ([Friedman et al 1951]). After 13 years the improvement of a rocket technology and a sensitivity of X-ray detector, proportional counter, made it possible to detect the X-ray source outside our solar system, Sco-X1([Giacconi et al 1962]).

X-ray astronomy has been developed quickly from 1970's. The first X-ray astronomical satellite *UHURU* was launched in 1970. The *UHURU* X-ray catalogue contains 339 objects. These are binary stars, supernova remnants, Seyfert galaxies and – unexpectedly detected – clusters of galaxies. After that, it became clear that the origin of emission from clusters is thermal emission from a optically thin hot plasma($10^7 \sim 10^8\text{K}$, $\sim 10^{-3}\text{cm}^{-3}$) and it is an intrinsic property of clusters of galaxies.

Cluster of galaxies is the largest gravitational bound system in the universe and the brightest X-ray emitter. From the velocity dispersion of member galaxies in clusters, it has been clear that clusters contain the large amount of invisible mass, so called 'dark matter', which is about ten times larger than the visible mass. Since the intracluster medium is dissipative, contrary to galaxies in a cluster, the observation of the intracluster medium by X-ray is useful tool to investigate the gravitational mass and dark matter distribution and hence to understand the large scale structure of the universe.

Structures in the universe seems to have been born from initial density perturbation and grown up. Though how the perturbation was born and how the perturbation function was expressed are never known, the efforts have been continued to solve those problems by the theoretical simulation of the perturbation growth based on the current dark matter distribution. The simulations also have dependency on cosmological parameters (Ω_0, H_0, Λ). Therefore the study of the current dark matter distribution in galaxies

and clusters give us the clue for the cluster evolution and the cosmological model.

The X-ray observation of clusters of galaxies make another approach for cosmology possible. This is the observational and traditional approach for cosmology, 'the Hubble constant measurement'. Usually the constant is used for the distance estimation from the redshift of objects of which distance can not be measured (Hubble law, see section 3). However, in spite of the fundamental constant of the cosmology, the measured values are distributed within factor 2. This dispersion has been caused by the various uncertainties; peculiar motion, absolute magnitude of standard candles, underlying physical process and so on.

The derivation from the X-ray and radio cluster observation has advantages; small uncertainty of peculiar motion, clear underlying physical process. Furthermore, the distance to a cluster is available at the cosmological distance.

ASCA has a capability to investigate the accurate temperature and spatial distribution which is important for the Hubble constant measurement with clusters of galaxies.

In this thesis, we analyzed the luminous distant clusters of galaxies and measured the distances to those clusters, and finally shows the Hubble constant in the cosmological scale.

Chapter 2

Overview of Clusters of Galaxies

2.1 Definision and Classification

2.1.1 Catalogue

Optical study of large scale structure is mainly investigated by obtaining the distribution of galaxies and distances calculated by the redshift and the Hubble law. Although on the largest scale, the arrangement of matter in the universe is quite uniform, on an intermediate scale, galaxies are found in aggregates bounded gravitationally, so called as cluster of galaxies. They are the largest systems bounded by gravity in the universe. They contain the galaxies ranging a few to thousands and their typical size is roughly 10^{25} cm. Their total masses exceed 10^{48} g.

The first systematic study of clusters of galaxies was done by Abell([Abell 1958]) and statistically complete catalogue was made. Abell clusters of galaxies are used to be named by giving A and then the catalogue number of the Abell's list. This original Abell catalogue have confined to its sky coverage limited to declinations north of -27° which is the southern limit of the Palomar Sky Survey. In 1989, Abell, Corwin and Olwin published the revised catalogue(hereafter ACO catalogue) which included the southern part of the sky([Abell, Corwin & Olowin 1989]). It has been also revised and corrected the northern part of the original catalogue.

The cluster selection criteria are as follow,

- The cluster contains at least 50 galaxies in the magnitude interval m_3 to $m_3 + 2$, where m_3 is the magnitude of the third brightest cluster member.
- These galaxies have to be contained within a circle of radius $R_A = 1.7/z$ arcmin¹. z is the redshift of a cluster. For the cluster whose redshift has not been obtained,

¹In this paper, the Hubble constant will be parameterize $H_0 = 50h_{50}$ km/sec/Mpc. According to this definition, R_A corresponds to $3h_{50}^{-1}$ Mpc. (see chapter 3 about H_0)

it is estimated from the magnitude of the tenth brightest cluster member.

- The estimated cluster redshift z has to be in the range 0.02 to 0.2.

The ACO catalogue contains 4076 clusters. In that catalogue, the galaxy number count within R_A and in the magnitude interval m_3 to $m_3 + 2$, measured redshift and morphological type in the Bautz-Morgan system(see 2.1.2) also listed.

2.1.2 Morphological classification

Spatial distribution of galaxies in clusters shows wide variety. For statistical study of cluster morphology, various systems for the morphological classification were published. Most of them adopt arrangement of brightest member galaxies to classify. The classification scheme of Rood-Sastry system([Rood & Sastry 1971], revised by [Struble & Rood 1987]) and Bautz-Morgan system([Bautz & Morgan 1970]) are listed in Table 2.1 and 2.2. These two and other(not presented here) classification systems are highly correlated and can be connected by a simple, one dimensional sequence as shown in Table 2.3. Regular clusters show highly symmetrical shape and concentration of galaxy distribution at the center. Irregular clusters show little symmetry in shape and central concentration. These clusters often indicate significant subclustering. Regular clusters are considered to be relaxed systems dynamically. On the contrary, irregular clusters seem less evolved systems.

2.2 Optical observation – Galaxy distribution

The existence of the morphological sequence of clusters from irregular to regular clusters (2.1.2) suggested that regular clusters may have undergone some sort of dynamical relaxation. The degree of relaxation can be also tested by the velocity dispersion (σ_r).

The radial component of the velocity (radial velocity; v_r) of a galaxy is obtained from the redshift. The recession velocity of a cluster is defined as the mean of the radial velocities of galaxies in the cluster $\langle v_r \rangle$. The radial velocities of individual member galaxies are distributed around this mean. The dispersion of the radial velocity distribution of cluster member galaxies is defined as the radial velocity dispersion σ_r . σ_r means the root mean square of the radial component of the velocity of the internal motion of each galaxy in the cluster rest frame.

The radial velocity distribution (also velocity dispersion of radial velocity about this mean) is useful to study dynamics and kinematics of the galaxies in the optical observation. In many cluster, it is known that the consistent fit to the observed total distribution function is available adopting the Gaussian distribution with some limitation(excluding high velocity galaxies) and some exceptions(subclustering). The Gaussian velocity distribution found in clusters suggests that they are not fully relaxed to thermodynamical

Table 2.1: Rood-Sastry morphological class

RStype	Description	Example
cD	The cluster dominated by a central cD galaxy. cD galaxies were defined by Mathews, Morgan & Schmidt(1964) as galaxies with the nucleus of a very luminous elliptical galaxy embedded in an extended, amorphous optical halo of a low surface brightness. They are generally found near the center of dense clusters and groups of galaxies.	A2199
B	(binary) The cluster containing a pair of luminous supergiant galaxies	A1656(Coma)
L	(line) The cluster containing at least three of the ten brightest galaxies aligned in a line	A426(Perseus)
C	(core) The cluster with four or more of the ten brightest galaxies settling in the center closely	A2065(Corona Borealis)
F	(flat) The cluster with the flat projected galaxy distribution	A2151(Hercules)
I	(irregular) Irregular distribution of brightest galaxies with no obvious center or core	A400

Table 2.2: Bautz-Morgan morphological class

BMtype	Description	Example
I	The cluster dominated by a single central cD galaxy	A2199
I-II	Intermediate	
II	The cluster containing the brightest galaxy intermediate between cD and normal giant ellipticals	A1656
II-III	Intermediate	
III	The cluster containing no dominant galaxies	Virgo

Table 2.3: Correlation between Rood-Sastry and Bautz-Morgan morphological class

Property	Regular	Intermediate	Irregular
BMtype	I,I-II,II	II,II-III	II-III,III
RStype	cD,B,L,C	L,C,F	F,I

equilibrium but at least partially relaxed systems. In thermodynamical equilibrium, all components of the cluster (intracluster gas and galaxies) would have equal temperature $kT = m\sigma_r^2$, (T is the 'galaxy temperature') and are isothermal. The observation of galaxy velocities in Coma cluster shows the two modal component of velocity dispersion([?]). Though total observed velocity distribution is not consistent with the single Gaussian function because of double peak structure of the distribution, it gives a convenient fit to it using the double Gaussian function. This suggests that there are two components in Coma cluster because of cluster merging or falling. Each of them is in the thermodynamical equilibrium with different galaxy temperature. Then the Coma cluster is at least partially relaxed system.

Regular clusters have symmetric smooth spatial distribution of galaxies and concentrated core. Unfortunately, none of isothermal models can represent the distribution exactly in terms of simple analytic functions. However, King(1962) showed that following analytic function is a reasonable approximation to the inner portions of an isothermal distribution,

$$n_{gal}(r) = n_{gal,0} \left(1 + \left(\frac{r}{r_c} \right)^2 \right)^{-\frac{3}{2}} \quad (2.1)$$

$$\sigma(b) = \sigma_0 \left(1 + \left(\frac{b}{r_c} \right)^2 \right)^{-1}$$

where $n_{gal}(r)$ is the spatial volume density of galaxies at a distance r from the center of cluster, r_c is the radius of cluster core(core radius) and $\sigma(b)$ is the projected surface density at a projected radius b .

Using the distribution of galaxies and velocity dispersion, total mass of cluster can be determined by the virial theorem. Typical total mass is estimated to be $\sim 10^{15} M_\odot$ and about 10 times larger than the visible(sum of the galaxies mass in a cluster) mass. From the comparison between the virial mass and visible mass, the existence of unobservable binding mass is necessary. This unobservable mass is so called 'dark matter'.

2.3 X-ray observation

Before launch of *Einstein* satellite, instruments for X-ray observations were the non-imaging gas proportional counters. Then the X-ray astronomy progressed mainly by the X-ray spectroscopy with low energy resolution.

The first detection of X-ray from the cluster of galaxies was performed in 1971 with *UHURU*. The properties of the X-ray emission associated with clusters obtained with *UHURU* from 1971 to 1976 are as follow,

- Clusters of galaxies are the most common bright extragalactic X-ray sources.
- Clusters are extremely luminous in their X-ray emission with luminosities ranging $\sim 10^{43} \sim 10^{45} \text{ ergs s}^{-1}$.
- X-ray emission associated with clusters are extended. The size found from the *UHURU* observations ranges from 200 to 300 kpc.
- X-ray spectra show no strong evidence for photo-absorption unlike the spectra of the compact sources associated with discrete sources either in nuclei of galaxies or stellar sources within our own galaxy.
- X-ray emission is not time variable.

These last three results suggested that the emission was truly diffuse, and not the emission from discrete sources. However, in those early days, the distinction between thermal and non-thermal spectra can not be made unambiguously.

The discovery of line emission from highly ionized iron in the X-ray spectra of clusters suggested that the origin of X-ray emission is thermal process ([Mitchell et al. 1976], [Serlemitsos et al. 1977]). The line feature can be represented by the blend of He-like(Fe^{24+}) and H-like(Fe^{25+}) K_{α} emission lines at the energy of 6.7keV and 6.9keV, respectively. Furthermore, iron K_{β} line was also detected. Relative intensities of various lines from the same element make it possible to diagnose the physical state and environment of the hot plasma. Then the X-ray emission was originated by hot and optically thin plasmas filled in the intracluster space, so called intracluster medium(ICM).

OSO-8 Ariel 5 and *HEAO-1* observations of clusters made large sample of the X-ray luminosity and temperature, and showed that the X-ray luminosity is highly correlated with the ICM temperature; $Lx \sim kT^3$ ([Mitchell et al. 1977], [Mitchell et al. 1979], [Mushotzky et al. 1978]).

After 1970's, the satellite with the X-ray telescopes, such as *Einstein*, *EXOSAT* and *ROSAT*, enabled us to map the morphology of emission in the X-ray band below 4 keV and made great progress. Especially *Einstein* launched in 1978 was the first satellite with focusing optics and made quite large sample of the brightness map of clusters. *ROSAT* has excellent spatial resolution and observed the substructure in the brightness distribution. But with these imaging missions, the spectral information (e.g. temperature, abundance) was not available accurately because of the limited energy band. Japanese X-ray satellite *GINGA* which was operated during 1987-1991, had Large Area proportional Counters (LAC). Since that detector had quite low background and high efficiency in the broad band of 2-20keV, *GINGA* observations of clusters of galaxies provided the averaged temperature with good accuracy even though that has no spatial information. *GINGA* also provide the accurate metal abundance. The metal abundance of rich clusters is $0.2 \sim 0.5$ times of

solar value. The heavy elements are produced by nucleo-synthesis in the core of the star. This suggests that ICM is the mixture of primordial gas and ejecta from galaxies.

The shape of the gravitational potential of the bright clusters were roughly estimated, using the simple models of density distribution of intracluster gas, deduced from X-ray images below 4keV and averaged temperature. The mass of the X-ray emitting intracluster matter is equal to or greater than the luminous mass.

Observations with X-ray focusing optics enabled us to classify clusters by the X-ray morphology. Spectral observations with non-imaging device add informations of ICM state to that classification.

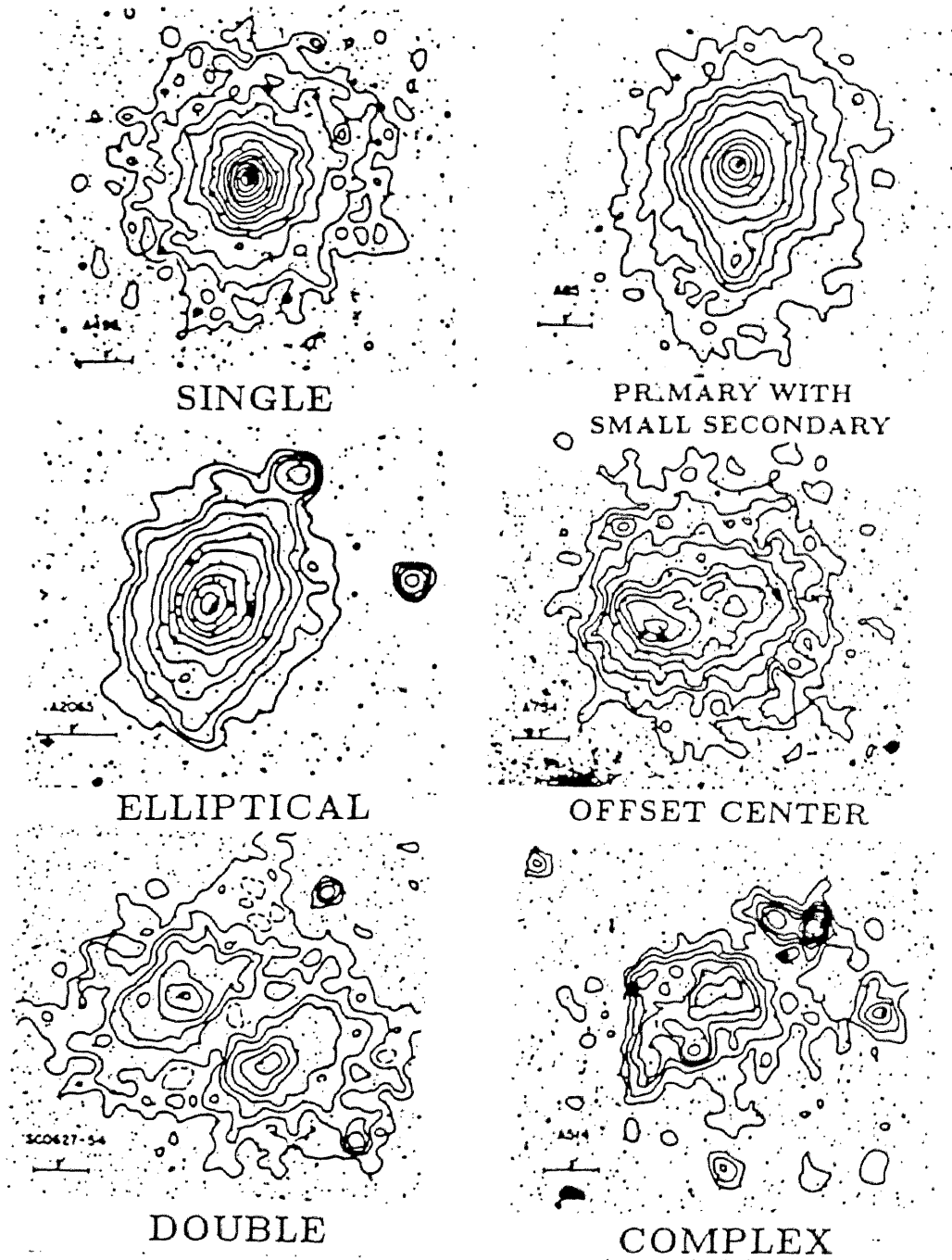
Jones and Forman (1991) analyzed *Einstein* observations of 208 clusters and proposed the classification scheme for the X-ray morphology based on the frequency and size of the substructure. They defined seven cluster morphological classes. Six of these are illustrated in Figure 2.1. The seventh class is one in which the X-ray emission is relatively weak and dominated from galaxies.

Table 2.4 shows the name of the class, the number of clusters in each class, the percent of the sample in that class and the mean X-ray luminosity for the class. Clusters with the smooth and concentrated brightness distribution (S, O and E) have large luminosity. They are considered as the evolved system. However, there is a large fraction of clusters ($\sim 20\%$) with complex and multiple-peaked structures (type C, D and P). Clusters classified as the type E and O with high temperature ($kT \geq 5\text{keV}$) show the large core radius. If clusters with the smooth profile and the large core radius are presently undergoing mergers, the percentage of clusters with substructures rises to about 40 % ([Jones & Forman 1991]). They indicate that the cluster potential is still evolving.

Table 2.4: Frequencies of cluster morphological classes

Class	Example	Number	Percent	$\langle L_X \rangle$ (erg/s)
S (single symmetric peak)	A401	120	56	2.9×10^{44}
O (offset center)	A2319	10	5	4.5
E (elliptical)	A2256	31	14	3.1
C (complex, multiple structures)	A514	27	13	1.0
D (double, roughly equal components)	A98	13	6	2.2
P (primary with a small secondary)	A85	7	3	2.0
G (primarily galaxy emission)	A2666	7	3	0.04

Figure 2.1: Examples of the X-ray morphology of several clusters in the classification scheme. Contours show the X-ray surface brightness and are superpose on optical images of the clusters.



2.4 Physical process of Clusters of Galaxies observed in the X-ray band

2.4.1 Emission mechanism

An X-ray energy spectrum from clusters consists of continuum emission and line emission. To examine the physical condition of intracluster medium (ICM) from the X-ray spectrum, it is necessary to study emission processes of thin hot plasma.

The continuum emission from a thin hot plasma is due to three processes, thermal bremsstrahlung (free-free emission), recombination (free-bound) and two-photon decay of meta-stable levels. At the high temperatures such as ICM ($kT > \text{a few keV}$), the major process is the thermal bremsstrahlung. The spectrum of thermal bremsstrahlung from electrons which obey a Maxwellian distribution is presented as ([Kato 1978])

$$\frac{dP_{ff}}{dE} = AZ^2 n_e n_Z \overline{g_{ff}}(E, T) e^{-\frac{E}{kT}} \text{ergs/sec/keV/cm}^3 \quad (2.2)$$

where E and kT are the energy of an emitted photon and the electron temperature in keV, respectively, n_e and n_Z are the electron number density and the ion density, respectively, Z is the ionic charge, $\overline{g_{ff}}$ is the average Gaunt factor which corrects for quantum mechanical effects, and A is a constant value. Using the equation 2.2, the electron temperature kT can be obtained by fitting the continuum shape of a observed energy spectrum.

In the case of low temperature ICM below a few keV, the line emission from various elements in some ionization state comes into prominence. Since the intensity of line emission is proportional to the ion density. Then populations of ionization states are important. The ion density of ionic stage Z is obtained by solving a set of equations,

$$\frac{dn_Z}{dt} = S_{Z-1} n_e n_{Z-1} - S_Z n_e n_Z - \alpha_Z n_e n_Z + \alpha_{Z+1} n_e n_{Z+1} \quad (2.3)$$

where S_Z is the total ionization coefficient including direct collisional ionization and autoionization from ionic stage Z to stage $Z + 1$, and α_Z is the total recombination coefficient including radiative and dielectronic recombination from stage Z to stage $Z + 1$. The condition $\frac{dn_Z}{dt} = 0$ is the 'collisional ionization equilibrium (CIE)'.

For characterizing the ionization degree, following parameter are used,

$$\tau \equiv \int_0^T n_e dt \quad (2.4)$$

where T is a time passed from the time when a heating is occurred. The collisional ionization state can be achieved with $\tau \sim 10^{12}$. For a typical cluster, it takes 30 Myr to become CIE in the central region ($n_e \sim 0.001 \text{ cm}^{-3}$). Since this is much less than the

age of cluster, the plasma will be assumed to be in CIE. Under the condition of CIE, the electron density dependence can be eliminated from the equation 2.3. Then the ionization state of a CIE plasma depends only on the electron temperature.

The emission model of thin hot plasma in CIE including line emission has been calculated by various authors; Raymond and Smith (1977), Kaastra and Mewe (1993), Masai (1984), and so on. These models are able to describe the emission line related to the K-shell electron of various elements. However, there is ambiguity in the prediction of the emission lines related to the L-shell electrons because of the difficulty of calculation. The plasma in a high temperature ICM (\geq a few keV) shows the lack of L line emission because ions are highly ionized and only K-shell electrons are left. Therefore the ambiguity is not critical in our study of ICM.

2.4.2 ICM Dynamics

The time required for a sound wave in the ICM to cross the cluster size is $\sim 10^9$ yr and shorter than the Hubble time ($\sim 10^{10}$ yr). Then, Unless the ICM experience the rapid gravitational potential change, heating or cooling, the ICM will be in the hydrodynamic equilibrium.

Assuming such equilibrium and spherical symmetry in ICM, the dynamical equation is described as,

$$\frac{1}{\rho} \frac{dP}{dr} = -\frac{GM(r)}{r^2} \quad (2.5)$$

where $\rho(r)$ is the mass density of ICM, P is the pressure and $M(r)$ is the binding mass within the radius r from the center of cluster (including the darkmatter). If the gas is an ideal gas, the equation 2.5 can be modified to,

$$M(r) = -\frac{rkT}{\mu m_p G} \left(\frac{d \log \rho}{d \log r} + \frac{d \log T}{d \log r} \right) \quad (2.6)$$

where μ is the mean mass per particle in the gas in unit of the proton(mean molecular weight), m_p is the proton mass.

Apparently from equation 2.6, the total mass estimation is very sensitive to the temperature distribution rather than the density profile.

The member galaxies are bounded in the same gravitational potential. Assuming the orbit of galaxy in the cluster is not disturbed by other galaxies (the galaxies are less interactive with each other), the equation 2.5 can be rewritten for the galaxies (section 2.2),

$$\frac{1}{n_{gal}} \frac{d(n_{gal}\sigma_r^2)}{dr} = -\frac{GM(r)}{r^2} \quad (2.7)$$

where σ_r is the velocity dispersion of member galaxies in the cluster. Combining the equation 2.5 and 2.7, and assuming the isothermal condition, the spatial distribution of gas can be expressed using galaxy distribution function,

$$\begin{aligned} n_g(r) &\propto n_{gal}^\beta(r) \\ n_g(r) &= n_{g,0} \left(1 + \left(\frac{r}{r_c}\right)^2\right)^{-\frac{3}{2}\beta} \\ \beta &\equiv \frac{\mu m_p \sigma_r^2}{kT} \end{aligned} \quad (2.8)$$

where β is the square of the ratio of galaxy to mass specific energy.

Using the equation 2.8 and isothermal condition, it is possible to predict the X-ray surface brightness distribution. The volume emissivity of ICM is expressed as,

$$\epsilon = n_g^2 \Lambda(T) \quad (2.9)$$

where $\Lambda(T)$ is the X-ray emission at unit electron density. The surface brightness S_x at the projected radius b measured from the center of cluster is as follows,

$$\begin{aligned} S_X(b) &\propto \int_b^\infty \frac{\epsilon(r) 2r dr}{(r^2 - b^2)^{1/2}} \\ &\propto S_{X,0} \left(1 + \left(\frac{b}{r_c}\right)^2\right)^{-3\beta + \frac{1}{2}} \end{aligned} \quad (2.10)$$

The equation 2.10 is commonly used for evaluation of the observed surface brightness distribution and most of the clusters with smooth brightness profile are relatively well fit by this model. However, in the case of regular-XD clusters, there are significant residuals from the model around the central strong peak in the brightness distribution.

2.5 Evolution and Cosmology

The comparison of various parameters between nearby and distant clusters may provide the information of cluster evolution. Efforts to find the evolutionary effect of clusters by the comparison has been made. However, any evolutionary effect has not been reported except for the total X-ray luminosity function(XLF), since the temperature and abundance

of distant clusters have never been obtained because of the low sensitivity and the narrow band path of the detection system.

Some groups have reported a decrease in the amplitude of the X-ray luminosity function with redshift, in other words, the number of luminous clusters decrease with redshift. This means the X-ray cluster is still in the evolving stage ([Edge et al. 1990], [Henry et al. 1992], [Castander et al. 1995]).

The present X-ray morphology of clusters also used for the test of cosmological models. Because the initial density fluctuation in the early universe has grown up to the hierarchical structure in the current universe, the X-ray morphology and darkmatter morphology is the key leading to the solution of the evolution. Then models with various functions of the initial density fluctuation, various kinds of darkmatter (cold dark matter; CDM, hot dark matter; HDM and so on) and various cosmological model (Ω_0 and Λ ; see chapter 3) has been tested by comparison of the simulated evolved clusters with the observed cluster morphology ([Crone, Evrard & Richstone 1994], [Kaiser 1991a], [Kaiser 1991b]).

The X-ray observation of clusters of galaxies provides the another and more fundamental approach to the cosmology introduced in the next chapter.

Chapter 3

Hubble Constant

3.1 What is the Hubble Constant?

Most of galaxies have the redshift rather than blueshift. This means that most of objects are running away from us. This is due to the expansion of the universe. Edwin Hubble measured distances various objects including the extragalactic realm. Hubble's approach was generally a three step process: 1. find distances to local group galaxies from Cepheids, 2. use the brightest star criterion, which he calibrated in the local group, to extend the scale to more distant field galaxies and the Virgo cluster, and 3. use the total magnitude of the galaxy, together with the luminosity function calibrated in step 2, to arrive statistically at distances for galaxies with measured redshifts. This is called as 'distance ladder' method and the object of which an absolute magnitude can be deduced such as the Cepheid is called as 'the standard candle'. They are used for the distance measurement at present. Finally, he found the velocity - distance relation. This relation can be expressed as,

$$v_r = H_0 r \quad (3.1)$$

where v_r is the recession velocity(or the Hubble flow), r is a distance from us to a object and H_0 is the Hubble constant.

While the recession velocity is easy to measure by the redshift of emission lines¹, the measurement of a distance to a object is difficult (see section 3.4). Usually, the distance to a object of which distance can not be measured is estimated from the equation 3.1. Therefore the Hubble constant determines the distance to objects.

The Hubble constant also give us the time scale of the age and the size of the universe. Assuming the recession velocity has been constant during the expansion, the time passed from the beginning of expansion t is,

¹The Hubble flow velocity of the object which is extremely closed to us is very small in comparison to the peculiar motion or the locally systematic motion (e.g. Virgo infall). Then the recession velocity has a ambiguity for the closest objects. (see section 3.4)

$$t = \frac{r}{v_r} = \frac{1}{H_0} \quad (3.2)$$

Assuming $H_0 = 50$ km/sec/Mpc, the time scale is 2×10^{10} yr. Using this timescale, the size of the universe is $tc = c/H_0 \sim 1.8 \times 10^{28}$ cm (~ 6 Gpc).

Actually, the distance to a object at a cosmological distance, the age and the size of universe have the dependency on the cosmological model as shown in the next session.

3.2 Cosmological model

In order to obtain H_0 , the distance r and recession velocity v have to be measured independently. Correctly, since the expansion speed could be changed with time and depend on the cosmological model, we have to treat them with the cosmological model to derive H_0 using the distant($z \sim 1$) objects.

In the isotropic and homogeneous universe, the line element can be described as the function of r in the polar coordinate (r, θ, ψ) ,

$$ds^2 = c^2 dt^2 - R^2(t) \left(\frac{dr^2}{1 - kr^2} + r^2(d\theta^2 + \sin^2 \theta d\psi^2) \right) \quad (3.3)$$

where t is cosmic time, $R(t)$ is the radius of curvature or scale factor of the universe and k is the curvature index; $k = -1, 0, 1$. This is called the Robertson and Walker metric. When the Robertson and Walker metric is used with Einstein's field equations, following equations are obtained,

$$\frac{3\dot{R}^2}{R^2} + \frac{3kc^2}{R^2} = \frac{8\pi G}{c^2} \rho c^2 + \Lambda c^2 \quad (3.4)$$

$$\frac{\ddot{R}}{R} = \frac{\Lambda c^2}{3} - \frac{4\pi G}{3} \left(\rho + \frac{3P}{c^2} \right)$$

where ρ is the density ($\rho(t)$), P is the pressure of matter and radiation ($P(t)$) and Λ is the cosmological constant. Customarily the following definitions are used,

$$\begin{aligned} H_0 &\equiv \frac{\dot{R}_0}{R_0} \\ q_0 &\equiv -\frac{\ddot{R}_0}{R_0 H_0^2} \\ &= -\frac{1}{H_0^2} \left[\frac{\Lambda c^2}{3} - \frac{4\pi G \rho_0}{3} - \frac{4\pi G P_0}{c^2} \right] \end{aligned} \quad (3.5)$$

$$\Omega_0 \equiv \frac{\rho_0}{\rho_c}$$

$$\rho_c \equiv \frac{3H_0^2}{8\pi G}$$

where subscription 0 denote the present value, H_0 is the Hubble constant, q_0 is the deceleration parameter, Ω_0 is called the density parameter and ρ_c is called the critical density. According to this definition, H is the rate of expansion and is variable with time (the value at the present time is H_0).

Using these parameters and assuming $P = 0$, equation 3.4 can be expressed as,

$$3H_0^2 \left(\frac{1}{2}\Omega_0 - q_0 \right) = c^2\Lambda \quad (3.6)$$

$$H_0^2 \left(\frac{3}{2}\Omega_0 - q_0 - 1 \right) = \frac{kc^2}{R_0^2}$$

When $\Lambda = 0$, the relation between q_0 and ρ_0 is easily expressed as,

$$q_0 = \frac{1}{2}\Omega_0 \quad (3.7)$$

Then $R(t)$ (and the distance derived with $R(t)$) can be expressed with H_0 and Ω_0 .

The characteristics of the universe (so-called Friedman universe) in the case of $\Lambda = 0$ are listed in Table3.1 and Figure3.1.

When $\Lambda \neq 0$, the deceleration parameter becomes,

$$q_0 = \frac{1}{2}\Omega - \frac{c^2\Lambda}{3H_0^2} \quad (3.8)$$

In this case, to determine $R(t)$ (and distance), it is necessary to decide H_0 , Ω_0 and Λ .

Figure 3.1: The scale factor $R(t)$ of the Friedman universe. t_0 is the age of the universe

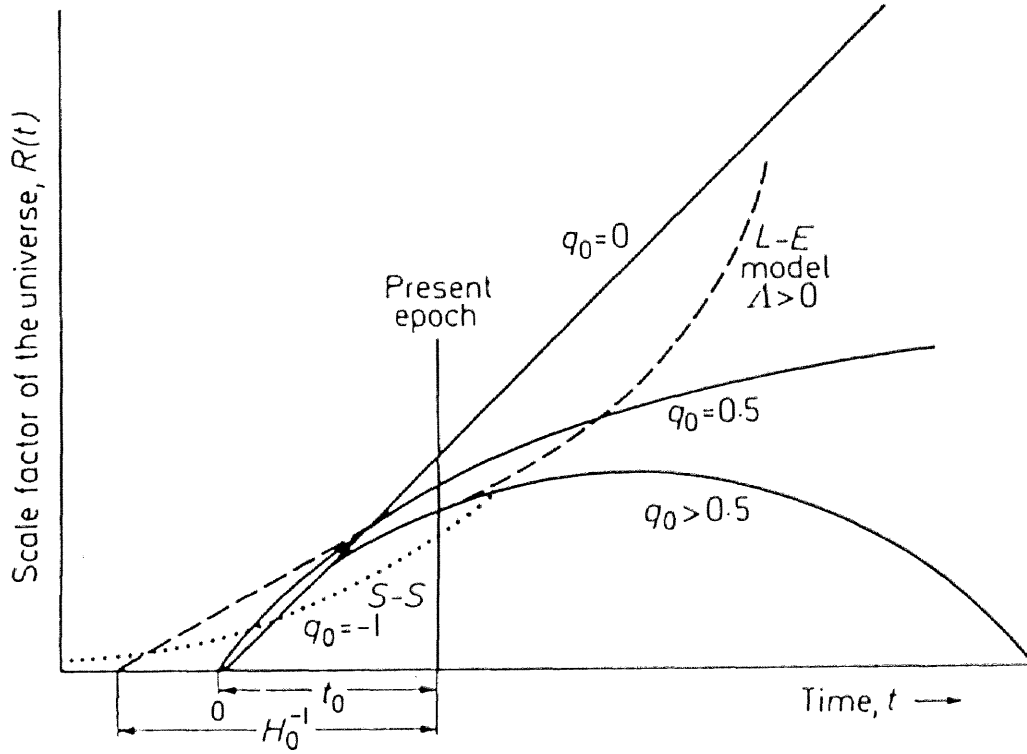


Table 3.1: Characteristics of Friedman universe

k		$R(t)$	q_0	Ω_0	Age
+1	elliptical closed space (Total energy < 0)	Oscillating (Oscillat- ing universe)	> 0.5	> 1	$< \frac{2}{3}H_0^{-1}$
0	flat Euclidean space (Total energy $= 0$)	continuously expand- ing (Einstein-de Sitter universe)	$= 0.5$	$= 1$	$= \frac{2}{3}H_0^{-1}$
-1	hyperbolic open space (Total energy > 0)	continuously expand- ing (Milne universe)	< 0.5	< 1	$> \frac{2}{3}H_0^{-1}, < H_0^{-1}$

3.3 Distance

While the redshift can be obtained simply, the distance has several definitions for the measuring method. Among these, two definitions of distance are used; Luminosity distance and Angular diameter distance (see chapter 3.4).

Definitions of the luminosity distance D_L and the angular diameter distance D_A are as follows,

$$D_L = \sqrt{\frac{L}{4\pi f}} \quad (3.9)$$

$$D_A = \frac{l}{\Delta\theta}$$

where L is the luminosity, f is the observed flux, l is the diameter and $\Delta\theta$ is the angular size of l . The distance to the object closed to us ($z \ll 1$) is approximately,

$$D_L \sim D_A \sim \frac{cz}{H_0} \quad (3.10)$$

However, for distant objects, $z \sim 1$, the energy reduction due to the redshift (factor $(1+z)^{-1}$), the time interval difference between at emitter and at observer (factor $(1+z)^{-1}$), and the effect of space curvature $R(t)$.

Considering these effects, D_L is expressed as,

$$D_L = \frac{cz}{H_0} \left[1 + \frac{z(1-q_0)}{1+q_0z+(1+2q_0z)^{1/2}} \right] \quad (3.11)$$

For D_A , the effect of the energy reduction and difference of the time interval does not exist. Then,

$$\begin{aligned} D_A &= \frac{D_L}{(1+z)^2} \\ &= \frac{cz}{H_0(1+z)^2} \left[1 + \frac{z(1-q_0)}{1+q_0z+(1+2q_0z)^{1/2}} \right] \end{aligned} \quad (3.12)$$

3.4 Review of derivation methods

There are three ways to measure the distance to a object,

1. Parallax
2. Absolute luminosity – observed flux relation

3. Absolute size – observed angular size relation

The 1st method is the most reliable direct distance measurement. But it is only applicable to a closest object to the solar system. Using the 2nd and 3rd methods, it is necessary that the absolute luminosity or absolute size of object have been known. Then the distance measurement method is equivalent to the estimation method of absolute luminosity or size from other observable parameters.

Cepheid Variable

The most accurate mean for the estimation of an absolute luminosity is 'Period - Luminosity' relation (P-L relation) of Cepheids. Cepheids are massive young and variable stars of which luminosities are $10^3 \sim 10^5$ brighter than the Sun. The period of variability can be converted to the luminosity. The relationship is well calibrated. Though it is easy to find out it because of its variability, Cepheids are not luminous to observe it in galaxies at the distance of several tens Mpc.

SNe Ia

The way which is applicable for the distance measurement using a more distant object is the use of Type Ia super novae (SNe Ia) ([Branch & Tammann 1992] and references therein). SN Ia is observable to ~ 400 Mpc. It is known from observations that the peak of the absolute magnitude of SNe Ia is almost constant. Then if the peak apparent magnitude is obtained by the light curve fitting to the template curve, the distance can be obtained from the comparison between the apparent and absolute magnitude. The peak absolute magnitude of SNe Ia can not be measured directly. Then the absolute magnitude has been calibrated using the distance of the host galaxy of SN Ia obtained with Cepheid variables. Recently, some authors suggested that the peak absolute magnitude is not constant and depends on the details of the shape of light curve ([Riess, Press & Kirshner 1995]), intrinsic color of an individual SN ([Höflich & Khokhlov 1996]), color or Hubble type of the parent galaxy ([Branch, Romanishins & Baron 1996]).

Tully-Fisher relation

There is the relation between the absolute magnitude and the 21cm line width of the spiral galaxy and it is used for distance measurement. The relation is called as 'the Tully-Fisher relation'. This is also applicable to ~ 100 Mpc. Though it is necessary to calibrate the zero level of the Tully-Fisher relation using Cepheids distance for the absolute distance measurement, it is the best method for the determination of the relative distance.

Current status

Recently, Hubble Space Telescope (HST) deep observations have enable us to measure Cepheid distances of galaxies in the Virgo and Fornax clusters([Freedman et al. 1994]). Freedman et al. (1994) observed 12 Cepheids in the Virgo cluster galaxy M100 by HST. They assumed that M100 is at the same distance as Virgo cluster core and derived the Hubble constant of $H_0 = 80 \pm 8 \text{ km sec}^{-1} \text{ Mpc}^{-1}$ with the recession velocity of Virgo cluster ;1404 km/s. However the peculiar velocity of the observed galaxies is not negligible in comparison to the Hubble recession velocity, leading to a additional uncertainty in H_0 .

In contrary to the Cepheids distance, SNe Ia distance provide the small value of the Hubble constant; $H_0 \sim 50$ ([Sandage et al. 1996], [Schaefer et al. 1996]).

3.5 Sunyaev-Zel'dovich effect

3.5.1 Outline

The Sunyaev-Zel'dovich effect arises from inverse-Compton scattering of the cosmic microwave background radiation by thermal electrons in a intra-cluster gas at temperature T_g (equal to the electron temperature T_e) ([Sunyaev & Zel'dovich 1981]).

On average, an inverse-Compton scattering causes a photon energy to increase by an amount proportional to $kT_e/m_e c^2$, where k is the Boltzmann constant, m_e is the rest mass of the electron, c is the speed of light and T_e is the electron temperature which is equal to T_g . If the number of scattering is large, the spectrum of the cosmic microwave background is distorted by the energy gain due to the inverse-Compton scattering definitely (figure 3.2).

This effect is observed as the reduction in the brightness of the microwave background radiation in the Rayleigh-Jeans region as seen in the low frequency band in figure 3.2.

The decrement of the brightness temperature (ΔT_r) is proportional to the product of the inverse-Compton scattering depth through the cluster and mean energy change of a scattering photon which is proportional to the electron temperature, and is hence expressed with the electron density n_e and temperature as

$$\frac{\Delta T_r}{T_r} \sim -\frac{2}{m_e c^2} \sigma_T \overline{n_e k T_g} l \quad (3.13)$$

where T_r is the temperature of the microwave background, and $\overline{n_e k T_g}$ is the average value of $n_e k T_g$ along that line of sight and l is the diameter of the cluster. The thermal bremsstrahlung X-ray flux F_X from the cluster scales as

$$F_X \propto \frac{L_X}{D_L^2} \propto \frac{\overline{n_e^2 (k T_g)^{1/2}}}{D_L^2} V \quad (3.14)$$

where V is the volume of the cluster, $\overline{n_e^2 k T_g^{1/2}}$ is the bremsstrahlung emissivity averaged over the cluster volume V and D_L is the luminosity distance. The volume $V \propto (D_A \theta)^2 l$, where D_A is the angular diameter distance and θ is the angular size of the cluster, then we will have D_A ($l = D_A \theta$) from the equation 3.13 and 3.14 with iso-thermal and spherically symmetric assumption. Assuming Ω_0 and q_0 , the H_0 can be derived from the relation between D_A and θ .

The motion of the scattering medium relative to the reference frame defined by microwave background also cause the change of the brightness temperature,

$$\frac{\Delta T_{rK}}{T_r} \sim -\frac{v_r}{c} \sigma_T \overline{n_e} l \quad (3.15)$$

where ΔT_{rK} is the decrement of brightness temperature due to the kinematic effect and v_r is the peculiar radial velocity. The observed ΔT_r includes the kinematic effect ΔT_{rK} and the thermal effect described above. The kinematic effect causes the change of the temperature of the blackbody radiation and dose not change the shape of spectrum. Then the frequency dependence of kinematic effect is different from the dependence which the thermal effect has (figure 3.3). Then the multiple frequency observation of ΔT_r make it possible to distinguish both effects. However, since the ratio of the kinematic to thermal effect is $0.11(v_r/1000\text{km/sec})(kT_g/8\text{keV})$ in the Rayleigh-Jeans limit, the kinematic effect is smaller than the thermal effect, especially for hot clusters.

The use of Sunyaev-Zel'dovich effect ([Sunyaev & Zel'dovich 1981]) is a fundamentally different way to derive the Hubble constant by 'standard candles' and the 'distance ladder' method because it relies on the use of the basic physical process instead of the local calibration of empirical relationships.

3.5.2 Previous results

A clear decrement of brightness temperature were found from several clusters e.g. CL0016+16, A665, A2218, A2163, A773 and A1413 ([Birkinshaw 1991], [Birkinshaw, Hughes & Arnaud 1991], [Birkinshaw & Hughes 1994], [Wilbanks *et al.* 1994], [Grainge *et al.* 1993], [Grainge *et al.* 1996]). X-ray observations of A665 and A2218 has been performed with *Einstein* for the spatial distribution of the density and with *GINGA* for the spatially averaged temperature of hot plasma. They gave H_0 of 51 ± 17 and $65 \pm 25 \text{ km sec}^{-1} \text{ Mpc}^{-1}$ ([Birkinshaw, Hughes & Arnaud 1991], [Birkinshaw & Hughes 1994]). Another *ASCA* observation of A2163 also gave an estimation of H_0 ranging between 42 and 100 $\text{km sec}^{-1} \text{ Mpc}^{-1}$ ([Markevitch *et al.* 1994], [Markevitch *et al.* 1996]).

Figure 3.2: The change of the spectrum of blackbody radiation due to scattering by hot Maxwellian electrons ($T_r \ll T_g$). The solid line shows the spectrum of blackbody radiation with the temperature T_r . The dashed line shows the distorted spectrum due to the inverse-Compton scattering by hot Maxwellian electrons with the temperature T_g

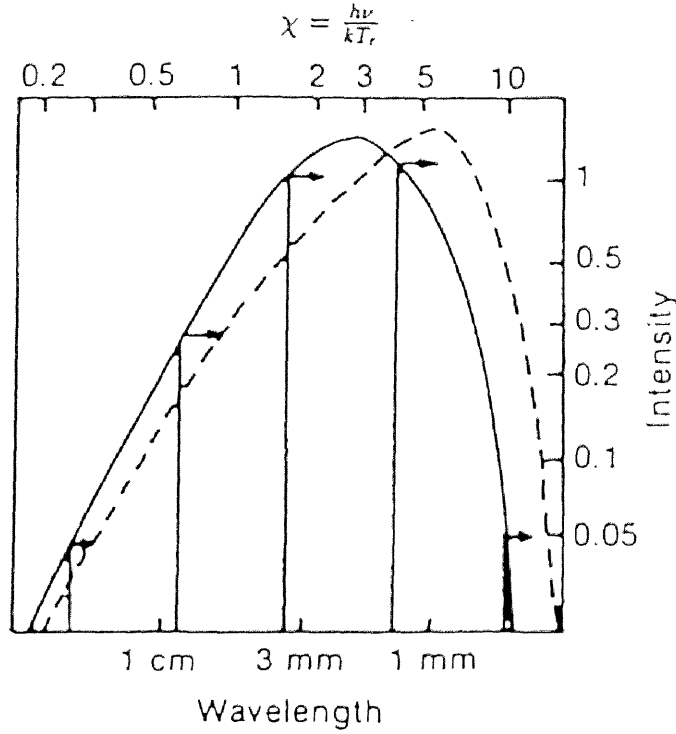
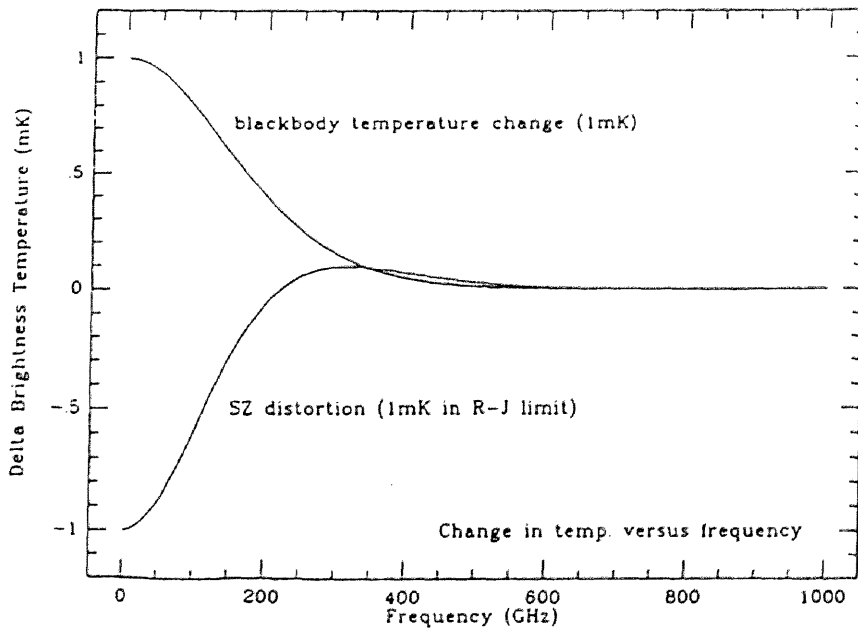


Figure 3.3: The frequency dependence of thermal S-Z effect and blackbody temperature change assumed to be 1mK (kinematic effect). Actually, kinematic effect is about 10 times smaller than the thermal S-Z effect.



Chapter 4

ASCA satellite

4.1 Overview

ASCA is the fourth Japanese X-ray astronomy satellite subsequent to *Hakucho*, *Tenma* and *Ginga* ([Tanaka, Inoue & Holt 1994]). *ASCA* was launched from the Kagoshima Space Center (KSC) by the M-3S-II rocket on February 20, 1993 and kicked into a orbit. The orbit is a near-circular with a perigee of 520 km and an apogee of 625 km, period about 96 min. and inclined with 31° . *ASCA* carries four identical X-ray telescopes (XRTs) at the top of an extensible optical bench (EOB), two Gas Imaging Spectrometers (GISs) and two Solid state Imaging Spectrometers (SISs) on that focal plane (figure 4.2). During the launch, EOB was retracted and solar paddles attached to the spacecraft body were folded up. *ASCA* with extending EOB and unfolded solar paddles in the orbit has an appearance like 'flying- bird', which is the origin of the name of "*ASCA*" in Japanese¹ (figure 4.1).

The spacecraft weight is 417 kg and its length is 4.7 m along the telescope axis. It is three-axis stabilized. The coordinate system on the satellite is defined as; Z axis is the direction of XRT, Y axis is the perpendicular direction to the solar paddle and X-axis is the perpendicular axis to other axes. *ASCA* has the four-axis momentum wheels and three-axis magnetic torquers and the attitude has been controlled by these actuators. The attitude sensors; 2 star trackers, non-spin type sun angle sensor, three axis geomagnetic aspect sensors and five-axis redundant gyros, have monitored the spacecraft attitude, and stabilize the Z-axis of the satellite above actuators. The absolute pointing accuracy is approximately 1 arcmin. and stability is about a few tens arcsec.

From April to October 1993, *ASCA* in the performance verification phase (PV phase) observed objects for scientific importance and the in-flight calibration of the spacecraft and the instruments. After this term, *ASCA* has opened to guest observers.

¹There is another statement that *ASCA* is the acronym of "Advanced Satellite for Cosmology and Astrophysics"

Figure 4.1: Appearance of ASCA in orbit

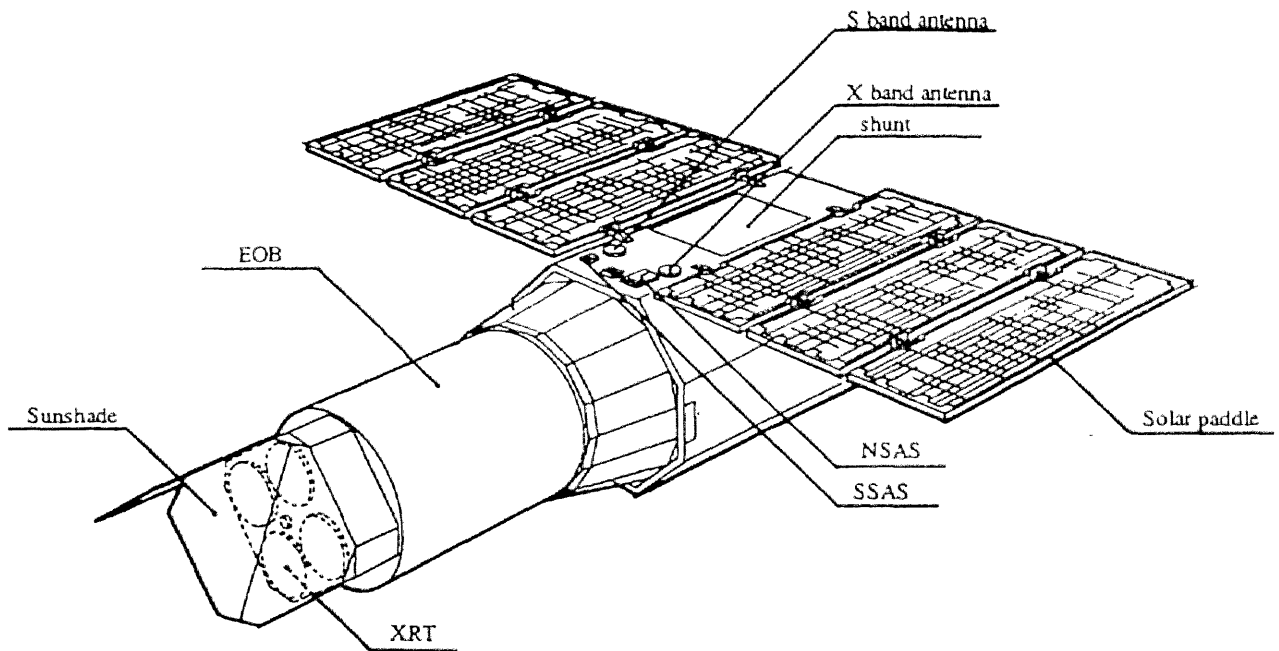
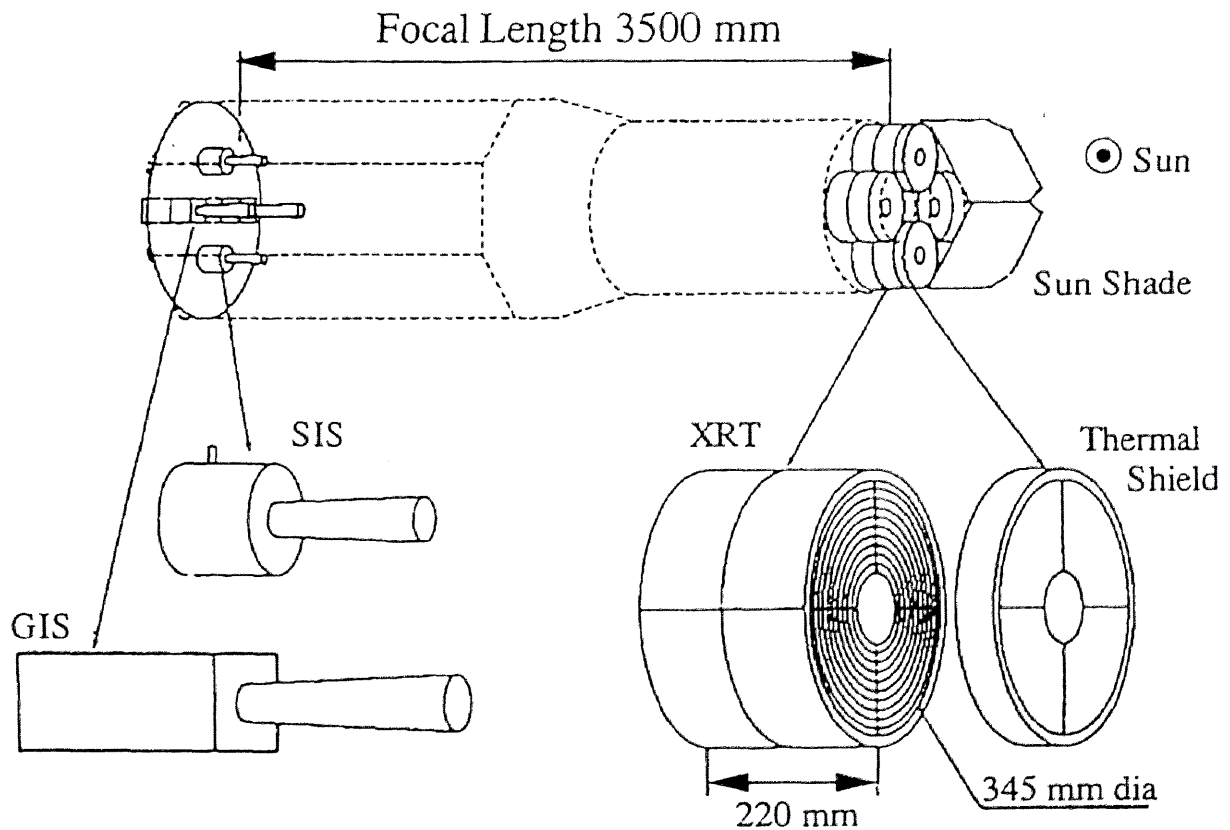


Figure 4.2: Configuration of instruments



4.2 Gas Imaging Spectrometer (GIS)

4.2.1 Overview

The GISs were developed mainly by the Tokyo University, ISAS, Tokyo Metropolitan University with collaborators at Institute of Physical and Chemical Researches (RIKEN), Kyoto University, and GSFC. The gas scintillation proportional counter was successfully carried on Tenma named SPC(Scintillation Proportional Counter; [Koyama et al. 1984]) and opened the new window of Fe Line Astronomy. The GIS consists of two detectors (GIS-2 and GIS-3) with the main electronics called GIS-E.

The advantage of GIS is its large FOV ($\sim 1^\circ$), excellent time resolution (61 s), and high sensitivity above 5keV energy region.

4.2.2 Structures and X-ray Detection Mechanism

Figure 4.3 shows the cross section of the GIS. The length and weight of on sensor is 58 cm and 4.2 kg, respectively. Figure 4.4 shows the schematic view of the GIS sensor system and photon detection. The X-rays collected by the XRT are detected by a gas cell containing Xe gas. For the entrance window of the gas cell, they adopted an innovative solutions in achieving a large effective area and a much improved soft X-ray efficiency: 10 μm thick Be foils of 65 mm diameter. Primary electrons produced by an X-ray drift toward the middle mesh under a weak electric field. The electrons then enter the emission region and accelerated by a stronger parallel electric field, giving rise to scintillation UV photons($\lambda \sim 1770 \text{ \AA}$) by repeatedly exciting xenon atoms. Unlike gas proportional counters, the electron multiplication does not take place, resulting the energy resolution to be twice better than that of the gas proportional counter ($E/\Delta E \sim 7 @ 1 \text{ keV}$).

The ultraviolet photons leave the gas cell through a fused quartz window, to be detected by the imaging photo-multiplier tube(IPMT). The pulse height information is extracted from the last dynode of the IPMT, while the position information is carried by outputs from two sets of multiwire anodes (16 for X direction and 16 Y direction). A charge-sensitive amplifier is attached to each of the 32 anodes. In order to calculate the position from these 32 anode signals, onboard CPU(80C286) is used.

4.2.3 Background Rejection

In orbit, the background rejection is carried out via a rise-time(RT) discrimination and a spread(SP) discrimination. The SP discrimination was enabled on May 28 1993. Therefore, we should take care the date of observation. It can reduce the non X-ray events appeared the edge of the detectors and is important to be set for the studies of extended or diffuse sources. The onboard RT acceptance window is set to be rather loose, which

Table 4.1: Time resolution and maximum transferable source intensity of the GIS

Mode	Bit rate	Time resolution		Max. source intensity
		Timing bits		
		0 bit	10 but	
PH	H	62.5 ms	61 μ s	256 c/s
	M	500 ms	61 μ s	256 c/s
	L	2 s	61 μ s	256 c/s
PCAL	H	31.25 ms		32 c/s
	M	250 ms		4 c/s
	L	1 s		1 c/s
MPC	H	0.5 s	1.95 ms	1024 c/s
	M	4.0 s	15.6 ms	256 c/s
	L	16 s	62.5 ms	64 c/s

can be tightened further on ground in the course of data analysis. By using this tight RT window, the non X-ray background can be reduced to be ~ 10 % while the X-ray is lost only 1 % ([Ohashi et al. 1996]). Applying SP discrimination after RT discrimination, ~ 85 % of non X-ray background can be rejected and its count rate within a radius of $17'$ is $(5 - 9) \times 10^{-14}$ c/s/cm² /keV in 1-10 keV([Makishima et al. 1996])

4.2.4 Observation Mode

There are different telemetry modes for the GIS; the pulse height(PH) mode, the multi-channel pulse count(MPC) mode, the position calibration(PCAL) mode, and the memory check mode. We usually use PH mode in the normal observation. PH mode is fully CPU-based data mode. After calculating the event position and applying the SP and so on, the CPU assigns each accepted event 32 telemetry bits. The 32 bits are a combination of sensor ID, pulse height, X and Y positions, rise time, spread of light signal, and the event arrival timing measured by the hard-wired logic. The bit assignment is adjustable; the nominal assignment is 1-10-8-8-5-0-0 bits. Time resolution and maximum source intensity for various observation modes are summarized in Table 4.1.

4.2.5 Effective Area of XRT/GIS

Figure 4.5 shows the effective area of the combination of XRT and GIS. The detection efficiency at low energy part is determined with the thickness of Be entrance window. Blow 0.7 keV energy regions, the efficiency is less than 10 % and almost all the flux

are due to a low-energy tail coming down from higher energy regions caused by partial absorption of primary electrons at the Be window([Inoue et al. 1978]).

4.2.6 Gain Corrections

Each sensor has the ^{55}Fe isotope (~ 0.3 c/s/GIS) attached to the edge of the entrance window to monitor the stability of the gain. The gain exhibits a temperature dependence of about 1 % per degree and a position dependence up to 20 %. These have been calibrated in orbit down to 1 %([Makishima et al. 1996]). We, usually, correct the GIS by using temp2gain to compensate the gain change due to the detector temperature. The gain is corrected for the peak of Mn- K_{α} to be 500 channel.

Figure 4.3: Cross section of the GIS

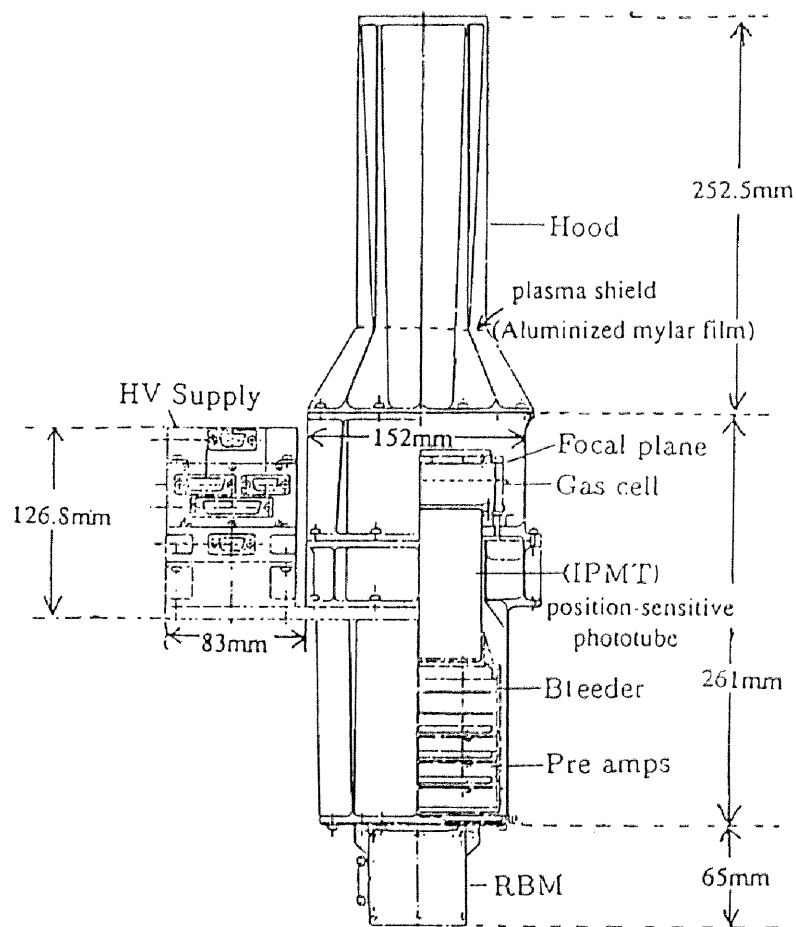


Figure 4.4: Schematic view of the GIS system

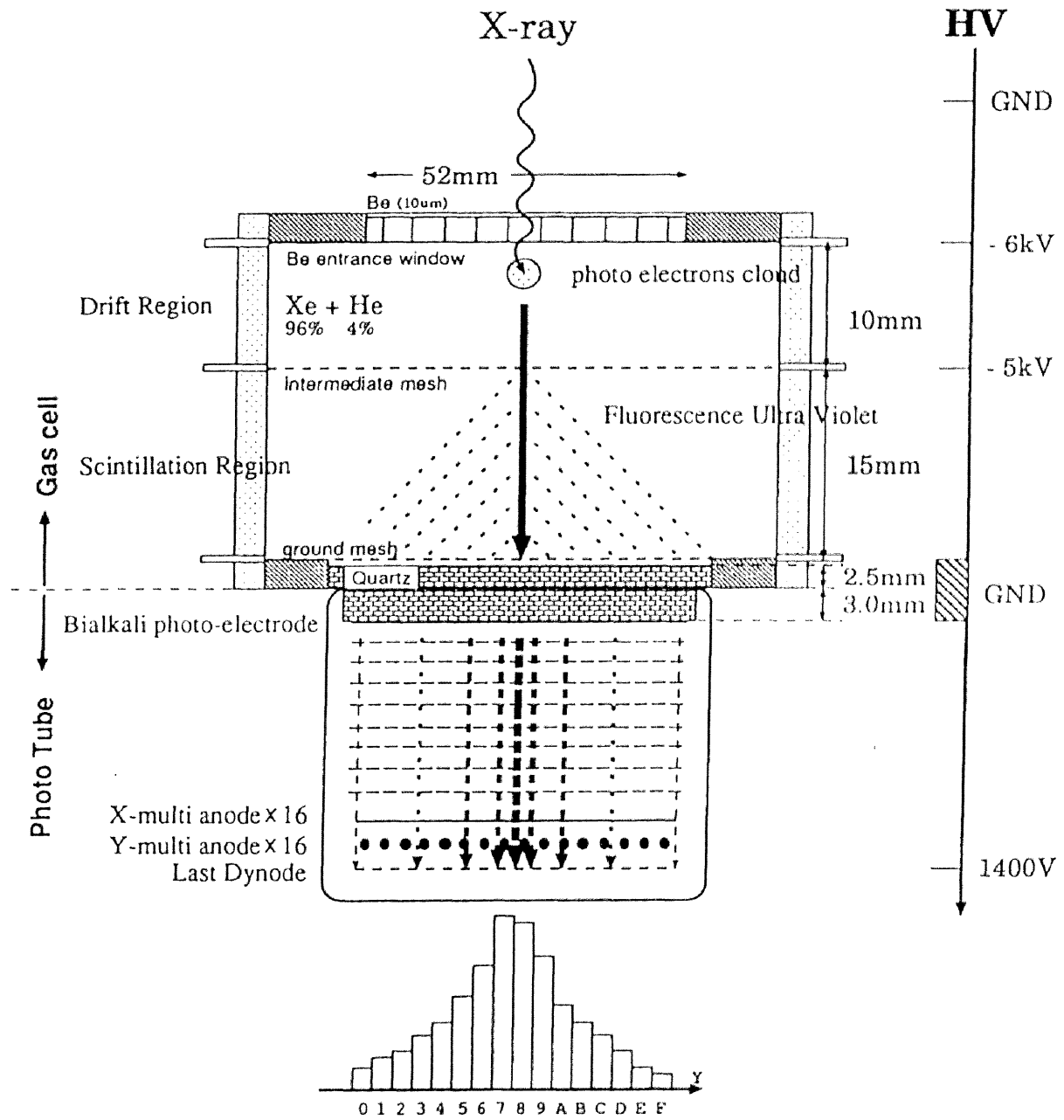
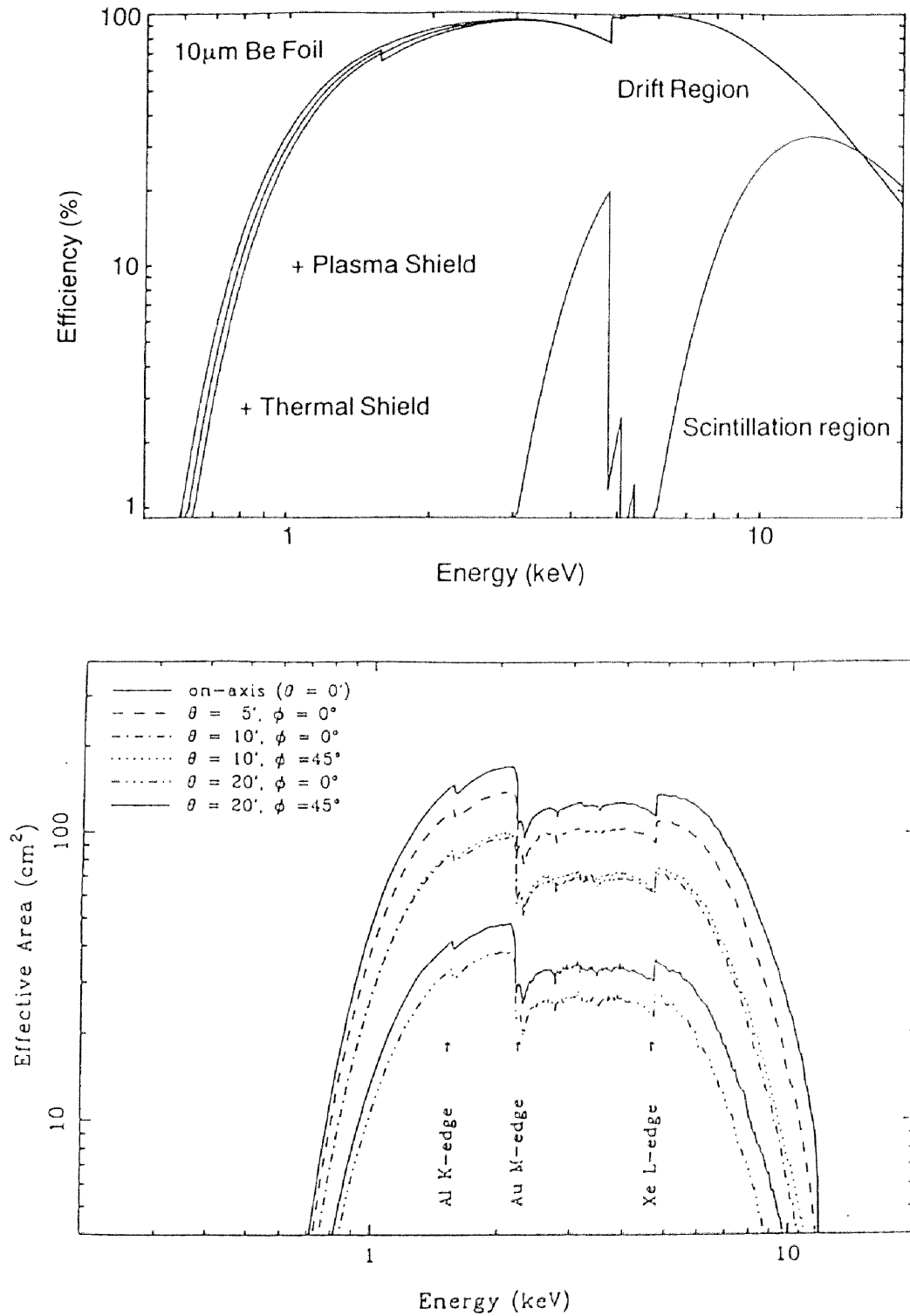


Figure 4.5: Quantum efficiency of GIS (Top) and Effective area of the XRT + GIS(Bottom)



4.3 Solid-state Imaging Spectrometer (SIS)

4.3.1 Overview

The Solid-state Imaging Spectrometer (SIS) experiment is the first X-ray detector in orbit that utilizes CCDs (charge coupled devices) in the photon counting mode. It was jointly developed by Massachusetts Institute of Technology (MIT), Pennsylvania State University, ISAS and Osaka University. The experiment consists of two detectors (SIS0 and SIS1), an analog electronics unit (SIS-AE), and a digital processing unit (SIS-DE) which is combined with the spacecraft data processor.

4.3.2 Structure and X-ray Detection Mechanism

Each SIS detector is made up of four CCD chips of 11 mm square each developed in the MIT Lincoln laboratory, to achieve a $22\text{ mm} \times 22\text{ mm}$ square area for X-ray detection. This covers a $22' \times 22'$ square region on the sky. Each chip has 4096 by 4096 pixels of $27\text{ }\mu\text{m}$ square each, and a depletion layer about $30\text{ }\mu\text{m}$ thick which ensures an improved efficiency for harder X-rays than conventional CCDs. Figure 4.6 shows the cross section of the SIS.

Figure 4.6: Cross section of the SIS

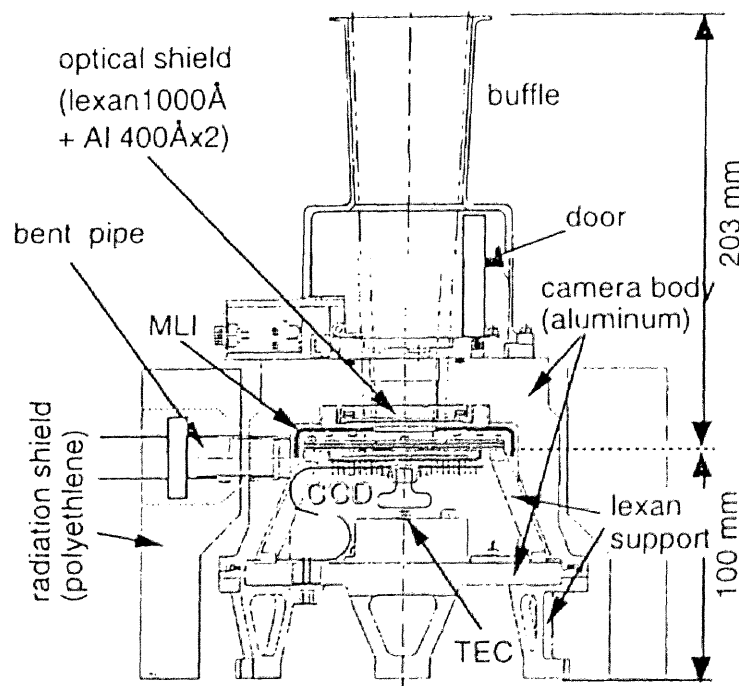
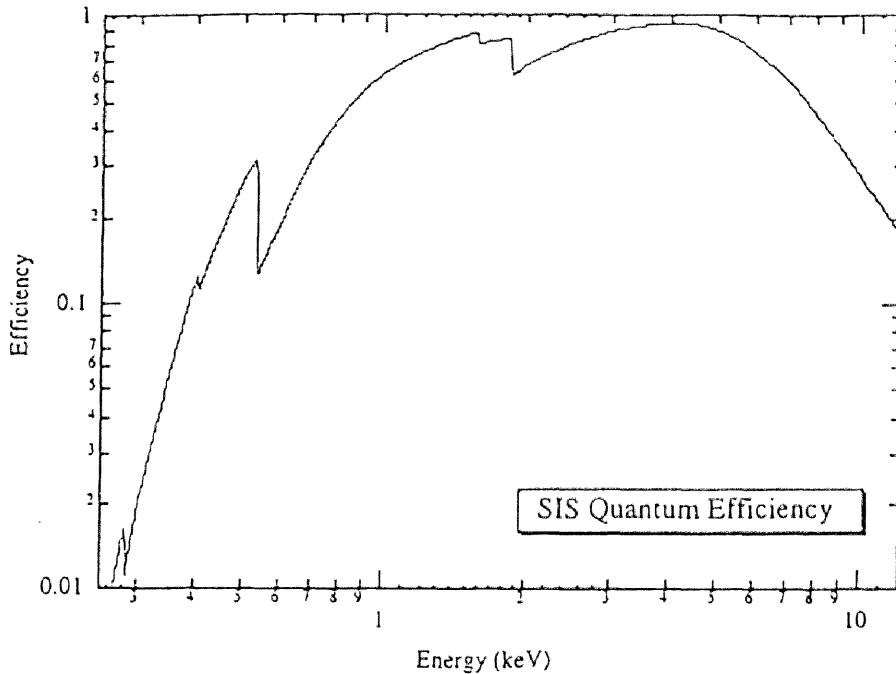


Figure 4.7 illustrates the quantum efficiency of the SIS as a function of X-ray energy. Thus the SIS sensitivity covers approximately $0.4 \sim 10\text{ keV}$. Thermal noise in the SIS

detectors is suppressed by electronically and radiatively cooling the CCD chips and pre-amplifiers down to -60°C . Thus the SIS achieves an FWHM energy resolution of about 150 eV over the whole energy range; this is the best energy resolution ever achieved by non-dispersive X-ray spectrometers so far put into orbit.

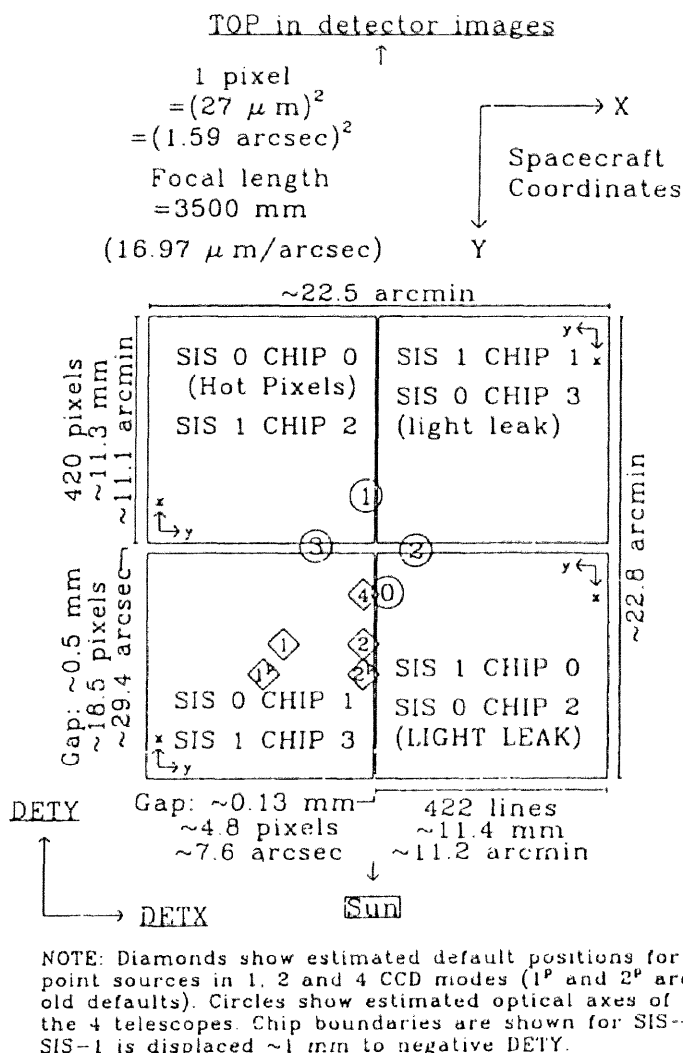
Figure 4.7: Quantum efficiency of the SIS



4.3.3 Observation Mode

In order to perform proper photon-counting spectroscopy, the CCD frame must be scanned and read out fast enough so that event pile up (i.e. one pixel receiving more than one X-rays) is virtually negligible. Since the read out cycle is usually limited by the telemetry capacity, the SIS performs an extensive on-board CPU processing to compress the information. Instead of sending data from all the pixels to ground, the SIS basically picks up only those pixels in which the charge exceeds a certain threshold, and sends out their addresses and pulse heights. Moreover to handle targets with different X-ray intensities and angular sizes under different telemetry rates, the SIS uses four different clocking modes; 1-CCD, 2-CCD, and 4-CCD modes. In the n -CCD mode ($n = 1, 2, 4$), data from n chips for each detector are read out. In the 1-CCD mode, e.g., the usable field of view becomes limited to a quarter of the detector, but the event pile up becomes least severe so that we can use slower telemetry rates and observe brighter sources than in other clocking modes. Figure 4.8 shows the source position in the 1-CCD, 2-CCD and 4-CCD clocking mode.

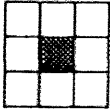
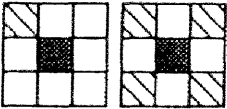
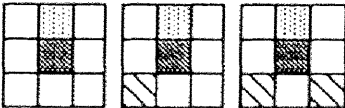
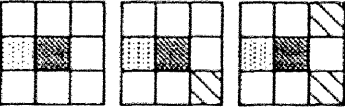
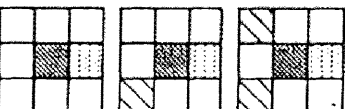
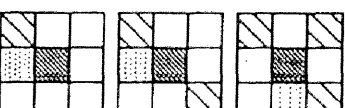
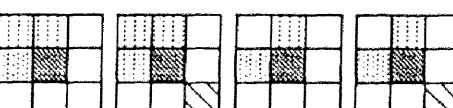
Figure 4.8: Top view of SIS chips






The electrons produced in the depletion layer by an X-ray photon may be split into several adjacent pixels. The pattern of charge splitting over 3 by 3 pixels is called 'event grade'. (When the charge is spread over more than 3 by 3 pixels, the event is rejected by the on-board CPU as a background event.) In order to cope with the splitting of normal X-ray events, the SIS incorporates several data selection modes. For example in so called 'faint mode', information on a certain pixel with event detection is always accompanied by similar information on the eight surrounding pixels. We can then examine the event ground on ground, and restore the total pulse height if necessary. In so called 'bright mode', the on-board CPU automatically recognizes the charge splitting pattern, and sends the total pulse height only for events with specified even grades. Figure 4.9 shows the definition of the grade corresponded to the charge splitting patterns. The faint

mode requires a larger telemetry capacity, but provides more information than the bright mode. Actually we can convert the faint mode data into the bright mode data on ground, but the reverse is impossible.

Figure 4.9: Grade definition

Grade definition	examples
S = Perfect Single (Grade 0)	
S+ = S + Detouched Corners (Grade 1)	
V = Vertical Single-Sided Split + Detouched Corners (Grade 2)	
L = Left Single-Sided Split + Detouched Corners (Grade 3)	
R = Right Single-Sided Split + Detouched Corners (Grade 4)	
P+ = Single-Sided Split with Touched Corners (Grade 5)	
L+Q = L Shape and Square Shape + Detouched Corners (Grade 6)	

-  A maximum level pixel larger than an event threshold
-  A pixel larger than a split threshold which is included for the pulse height computation
-  A pixel larger than a split threshold which is not included for the pulse height computation

4.3.4 Hot Pixels

Lattice defect in the silicon substrate causes a lower resistance in the insulation of electrode of particular pixels. It leads to a supurious background spectrum similar to a real X-ray event. Such defected pixels are called as hot pixels. Discarding of the hot pixel event can be easily done because number of readout is abnormally frequent from hot pixels compared with normal X-ray events. After the launch of the satellite, number of hot

pixels are increasing. This is thought to be due to an increase of lattice defect induced by the charged particles in orbit.

4.3.5 Echo

"Echo" is the phenomenon where some specific fraction of a pixel's pulse height(PH) leaks to the PH of the next readout pixel. Because PH and grade of an event is calculated using the PH of event's in 3×3 pixels, echo affects both the grade and energy of each photon event in a non-linear fashion. The echo values are different between the two sensors and ranging 1–2 % (Otani & Dotani 1994).

4.3.6 Dark Frame Error

"Dark Frame Error"(DEF) is the difference between the real zero level of pixels and that estimated by the on-board software. On-board software calculate "zero level" for each 16×16 pixels subsection by averaging the PH of pixels whose PH lies between -40 ADU and 40 ADU($1 \text{ ADU} \sim 3.5\text{eV}$). DEF mainly arise from asymmetric distribution of PH around zero, and is influenced by the charges generated by X-ray photons, charged particles, and optical light leakage on the CCD chips(Otani & Dotani 1994).

4.3.7 Corrections

Corrections for effects of each and DEF can be done for only Faint mode data. For the Bright and Fast mode data, corrections for those is impossible, since in these mode, data were already processed on-board determining the grade of event before the data acquisition at the ground station. However, we can estimate the effects in the mode from the Faint mode observations and incorporate it in the response matrices.

4.3.8 Light leakage

The light leaked from optical blocking filter shine the part of chip 2 and chip3 for SIS0. It presumably caused by a damage in the optical blocking filter. This affects the dark current of the CCD, and causes a subtle change in the energy to pulse-height relation.

4.4 XRT

Before *ASCA*, three major astronomical satellites; *Einstein* ([Van Speybroeck 1979], *EXOSAT* ([de Korte et al. 1981]) and *ROSAT* ([Aschenbach 1988]) are equipped with X-ray telescopes and have investigated the X-ray imaging study. However, these observations were restricted within narrow, and low energy band. Then these instruments have no capability to observe iron K line emission around 7 keV and obtain accurate spectral parameters, especially temperature above a few keV. In order to enable to cover the iron K line energy, the incident angle of photon should be twice smaller than that of previous mirrors and the aperture of the mirrors should be large to collect enough photons.

ASCA XRT was fabricated in collaboration between NASA Goddard Space Flight Center (GSFC), Nagoya University and ISAS. Though the XRT has moderate spatial resolution, about 3 arcmin. in half power diameter (HPD), it covers wide energy range up to 10 keV with large collecting area of $\sim 120 \text{ cm}^2$ at 7 keV (figure 4.10, Table 4.2). Thus, *ASCA* makes it possible to investigate the spatially resolved spectrum for the mapping of iron line intensity, and temperature for the first time.

Figure 4.10: Effective Area of XRTs in various mission

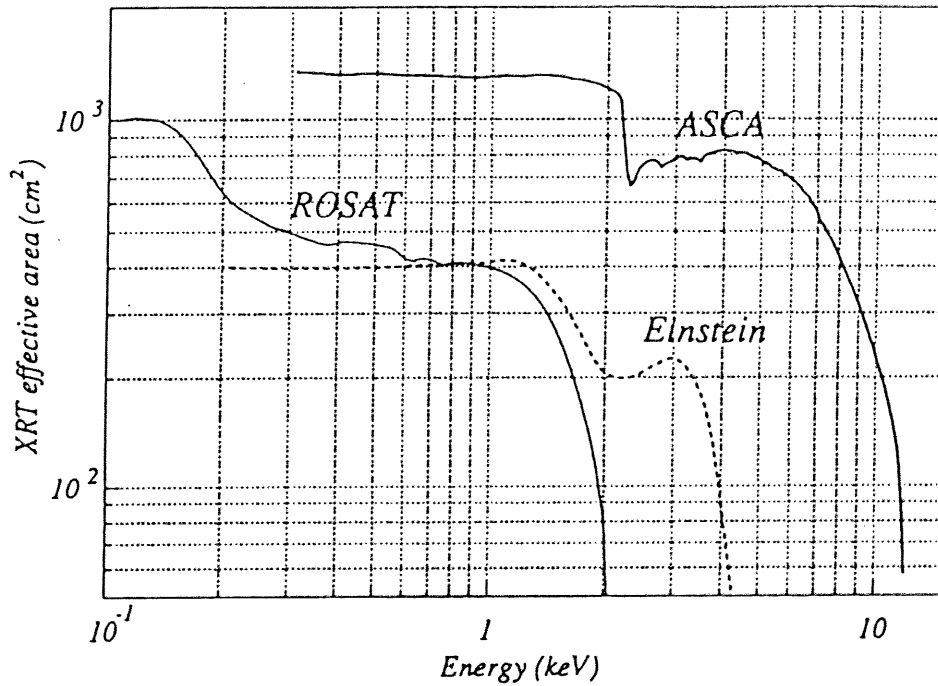


Table 4.2: Parameters of XRTs in various mission

	<i>Einstein</i>	<i>EXOSAT</i>	<i>ROSAT</i>	<i>ASCA</i>
Weight	500 kg	14kg (2 set)		40kg (4 set)
Focal length	3.4m	1.1m	2.4m	3.5m
Inner(Outer) Diameter	330(560)mm	220(278)mm	466(835)mm	120(344)mm
Mirror fabrication	polish	replica	polish	multi-nested thin foil mirror
Mirror substrate	Glass	Be	Glass	Al foil
Mirror thickness	~20mm	3.5mm	~30mm	0.135mm
Mirror surface	Ni	Au	Au	Au
Number of nest	4	2	4	120
Incident angle	0.7 ~ 1.2°	1.5, 1.8°	1.3, 2.4°	0.24 ~ 0.70°
Effective area(1keV)	~400cm ²	~70cm ² (2 set)	~300cm ²	~1200cm ² (4 set)
(7keV)	—	—	—	~ 450cm ² (4 set)
Spatial resolution	6arcsec.	5arcsec.	3arcsec.	180arcsec.

4.4.1 X-ray reflector and telescope

There is a critical reflection angle depending on the surface material of a mirror and photon energy. Sufficient reflectivity can be expected when the incident angle of photons (measured from mirror surface so-called grazing angle) is smaller than the critical angle. The X-ray reflectivity decreases rapidly above the critical angle.

The interaction of X-rays with matter can be expressed by the complex index of refraction of reflector in classical description;

$$n = 1 - \delta - i\beta \quad (4.1)$$

where δ describes a phase change and β is a factor related to absorption. δ and β are dependent on the photon energy and the surface material. For the reflection at the boundary between materials of the refraction indices n_1 and n_2 , there is the correlation between the incidence angle θ_1 and refraction angle θ_2 measured from surface (Snell's law);

$$n_1 \cos \theta_1 = n_2 \cos \theta_2 \quad (4.2)$$

And reflection coefficients for p and s polarization are given by Fresnel equations;

$$r_p = \frac{n_1 \sin \theta_2 - n_2 \sin \theta_1}{n_1 \sin \theta_2 + n_2 \sin \theta_1} \quad (4.3)$$

$$r_s = \frac{n_1 \sin \theta_1 - n_2 \sin \theta_2}{n_1 \sin \theta_1 + n_2 \sin \theta_2}$$

The reflectivity is given by $R_s = r_s r_s^*$ and $R_p = r_p r_p^*$, where the asterisk denotes the complex conjugate. For unpolarized X-rays, the reflectivity is $R = (R_s + R_p)/2$.

Now we consider the reflection at the boundary between vacuum ($n_1 = 1$) and the surface material matter ($n_2 = n$). Since the real part of the refraction index of the matter is less than unity as indicated in the equation 4.1 in the X-ray band, θ_2 is less than θ_1 . Then when θ_1 is smaller than critical angle (θ_c), θ_2 becomes zero. Ignoring the absorption, the equation 4.2 is modified as,

$$\cos \theta_c = 1 - \delta \quad (4.4)$$

Since δ is much less than unity, $\cos \theta_c \sim 1 - \theta_c^2/2$. Then,

$$\theta_c = \sqrt{2\delta} \quad (4.5)$$

where θ_c is the critical angle. For example, the critical angle of gold at 6 keV is about 0.75° .

Thus, to focus on X-rays, it is necessary to use the grazing incidence reflection. Several X-ray grazing incidence focusing systems have been proposed and realized so far; Kirkpatrick-Baez type systems, the Wolter type systems and so on. Among these, most useful for the X-ray astronomy is the Wolter-type systems. There are three types of Wolter system. All systems consist of two aspherical reflectors and photons are focused by two reflections. Wolter type I and II both utilized a paraboloid and a hyperboloid with common focus. For type I, the reflections take place on the inside surfaces of each mirror, and for type II, the reflection occurs on the inside of the paraboloid mirror and outside of the hyperboloid mirror. Wolter type III consists of confocal paraboloid and ellipsoid (figure 4.11). These systems have small collecting area because of grazing incidence. In order to gain large effective area, the incident angle should be large or telescope set should be nested. Then for the astronomy, nested Wolter type I telescopes of coaxial and common focus mirror shells have been used. *ROSAT* and *Einstein* have four nests of telescope shells, and *EXOSAT* carried a pair of two telescopes nested. However, these telescopes have limitation of low energy band because of still large incidence angle.

The increase of the number of nest is not efficient because of the obscuration by the edges of thick mirror substrates. For *ASCA* XRT, which is improved version of the BBXRT (Broad Band X-ray Telescope) flown on a US Space Shuttle mission in December 1990, the aluminum thin foil substrate has been adopted to avoid excessive edge obscuration by multi-nesting. Since it is impossible to hold concave figure of thin foil, it is the conical

approximation of the Wolter type I optics. While the XRT has large effective area in broad band, it has moderate spatial resolution ([Serlemitsos 1988]).

Figure 4.11: Wolter type I, II, and III telescope systems

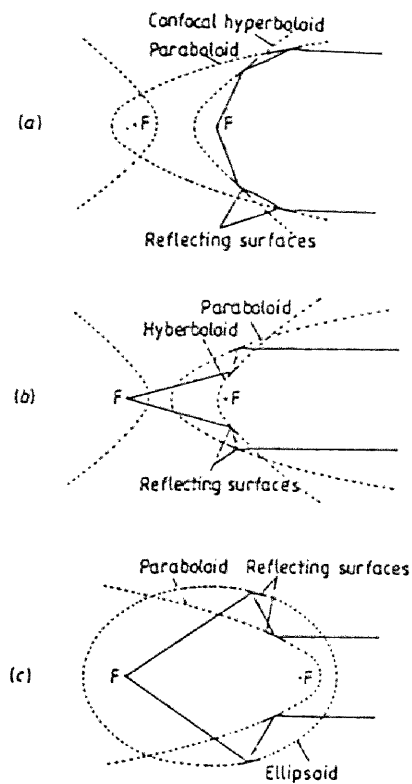
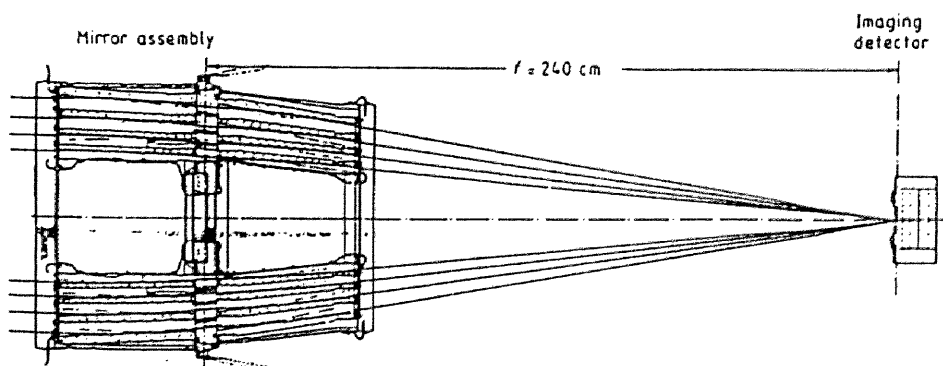


Figure 4.12: Schematic view of the XRT



4.4.2 Structure of ASCA XRT

The XRT aperture is an annulus with inner and outer diameters of 120 and 345 mm respectively and filled by 120 foils. The conical foil shaped by heat forming is coated with 10 μm Acrylic lacquer layer to reduce the surface roughness and with 500 Å Au layer above it on the reflection surface. The XRT consists of four quadrants (figure 4.13). In each quadrant housing, the foils are supported at top and bottom edges by the grooves on the 13 radial support bars (alignment bars). Each side of quadrant are closed by the side wall. A part between 2 alignment bars or alignment bar and housing side wall is called as 'sector' and identified by the number from 1 through 14. The sector No. 1 and No. 14 (each side edge of quadrant) are masked, because the both sides edge of foils are not supported and shows bad image quality. Gaps between quadrants are also masked. Then XRT produces the point source image with cusp-like peak and broad skirt which looks like four leaves (figure 4.14).

In front of the XRT, thermal shield is attached. If the XRT is exposed to cold space, the temperature of XRT becomes cooler than other instruments. This may induce contaminating on the reflector surface by the volatile material from the rest of the spacecraft. This may also cause a top-to-bottom temperature gradient in the XRT. These problems would degrade the reflectivity and image quality. To prevent thermal radiation, a very thin film has been placed, which is named as the thermal shield (figure 4.13). The thermal shield is aluminized Polyethylene Terephthalate (PET) film supported by a 0.15 mm thick stainless steel support mesh with 3 mm pitch. It is specially developed by TORAY Co. Ltd, to thickness of 0.22 and 0.54 μm for the SISs and GISs respectively. On the outer surface of the film, the 300 Å aluminum has been coated for the reduction of thermal emissivity and protecting from atomic oxygen bombardment.

The thickness of aluminum coating was measured using transmission of He–Ne laser. The thickness of PET was evaluated by the the weight measurement of film and the X-ray transmission.

Figure 4.13: *ASCA* XRT; Top left shows overlooking of the complete *ASCA* XRT, Top right is the top view of a quadrant, Bottom shows the top view of the complete XRT.

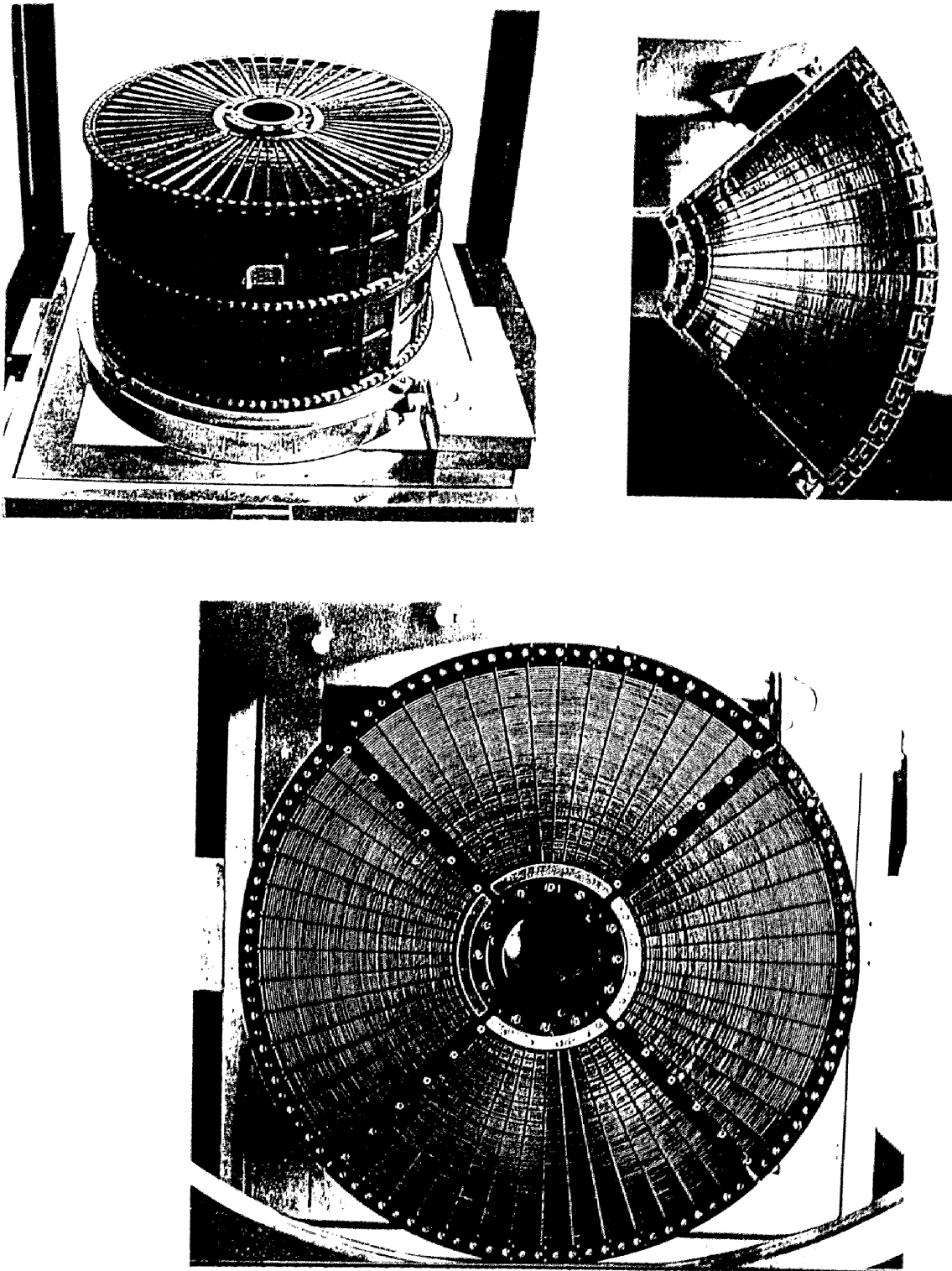
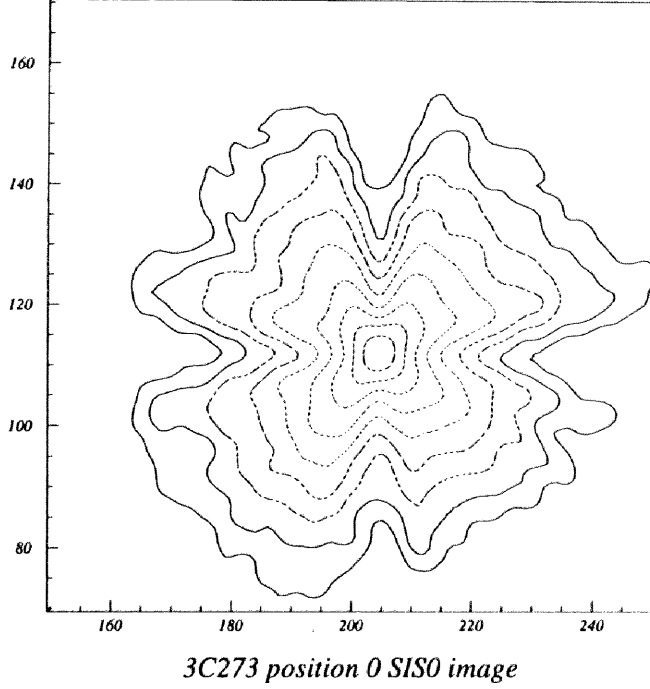


Figure 4.14: Image of point source



4.4.3 XRT calibration

To specify the XRT performance, the response function of XRT should be obtained. The response function can be expressed by following functions,

$$S_{eff}(E, \theta, \phi) \times F_{psf}(x, y; E, \theta, \phi) \quad (4.6)$$

$$\int \int_S F_{psf}(x, y; E, \theta, \phi) = 1$$

where S_{eff} is the effective area, F_{psf} is the point spread function (PSF), (x, y) are position on the focal plane, (θ, ϕ) are off-axis angle of an object measured from telescope axis and phase angle measured from the boundary of quadrants respectively, and E is incident photon energy.

Measuring S_{eff} and F_{psf} for the all situations of (E, θ, ϕ, x, y) is impossible. Then the S_{eff} and F_{PSF} are given by the ray-tracing simulation which is able to reproduce the measured data.

The investigation of the XRT performance on the ground was carried out at various facilities. The reflectivity (and optical constants) around the Au M absorption edge energy (near 2.2 keV) of foil mirrors was measured at the Ultra Violet Synchrotron Orbital

Radiation facility (UVSOR) of the Institute for Molecular Science (Okazaki, Japan). The quadrants and assembled XRT performance (Effective area, PSF and off-axis dependence of them) was measured at the 30m beam line at ISAS (Sagamihara, Japan) 300 m beam line at White Sands (N. M., USA). The details of pre-flight calibration have been published elsewhere ([Kunieda et al. 1993], [Serlemitsos et al. 1995], [Tsusaka et al. 1993], [Tsusaka et al. 1995]). Then in this paper, we describe the in-flight calibration and ray-tracing simulation.

Ray-tracing Program

To reproduce the XRT performance, the following parameters previously described are included in the ray-tracing program,

1. XRT design parameters
 - (a) XRT housing shape
 - (b) Foil thickness
 - (c) Foil length
 - (d) Top and bottom radii of all foil mirrors (the design value of groove position)
 - (e) Masked region
2. Foil mirror parameters
 - (a) Foil positioning error (groove position)

It causes the image shift and the peak broadening with limitation of groove width.
 - (b) Micro-roughness

It causes the energy dependent scattering tail of focal plane images.
 - (c) mm-scale Figure error

It causes the large scale peak broadening due to the fluctuation of normal vector on the mirror surface.
 - (d) sub-mm-scale Figure error

It causes the peak broadening (in small scale).
3. Reflectivity parameter
 - (a) Optical constants (δ, β)

These parameters had been tuned using ground based measurement data. The purposes of in-flight calibration were the confirmation whether the the XRT performance has been changed or not, and the adjustment of the optical constants.

Effective area adjustment

There is no reliable optical constant δ in the whole energy range of 0.5 – 10 keV because of the difficulties of absolute reflectivity measurements. Below 2 keV, most reliable δ has been published by Henke et al. (1982)² and in the range of 2 – 4 keV, δ was obtained from the absolute reflectivity measurement at UVSOR. For the higher energies (> 4 keV), we used δ obtained from the semi-empirical relation for δ derived from Henke's table, interpolating measurements 2 – 4 keV and reflectivity measurements at the discrete energies; 1.49 (Al-K), 4.5 (Ti-K) and 8.0 (Cu-K) keV, we have prepared a set of optical constants for the ray-tracing program. On the contrary, it is easy to obtain the reliable β since the measurement of β is directly obtained from absorption co-efficients. Then the β in the published data by Henke et al. (1982) were used in the ray-tracing program except 0.2 – 0.35 keV.

To adjust the optical constant δ at the energies above 4 keV, the high quality observed Crab nebula spectrum has been used. The Crab nebula has been known that it has ~ 3 arcmin. extension, constant flux and a simple energy spectrum. That spectrum can be explained by a power law function with photo-electric absorption with previous observations. The Crab nebula is too bright to observe by SIS. Therefore the adjustment of XRT response has been done using GIS data.

The adjustment procedure is as follows,

1. Calculate expected spectrum with GIS and XRT response³ for the Crab spectrum determined by previous experiments
2. Make δ change to eliminate the residuals of observed spectrum from expected one
3. Iterate (1) and (2)

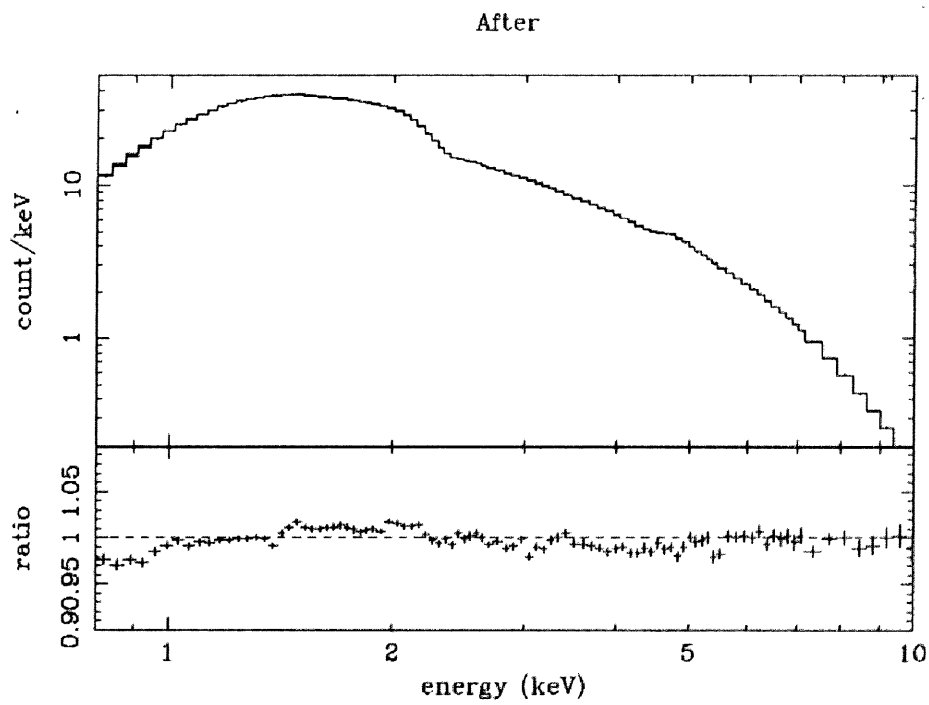
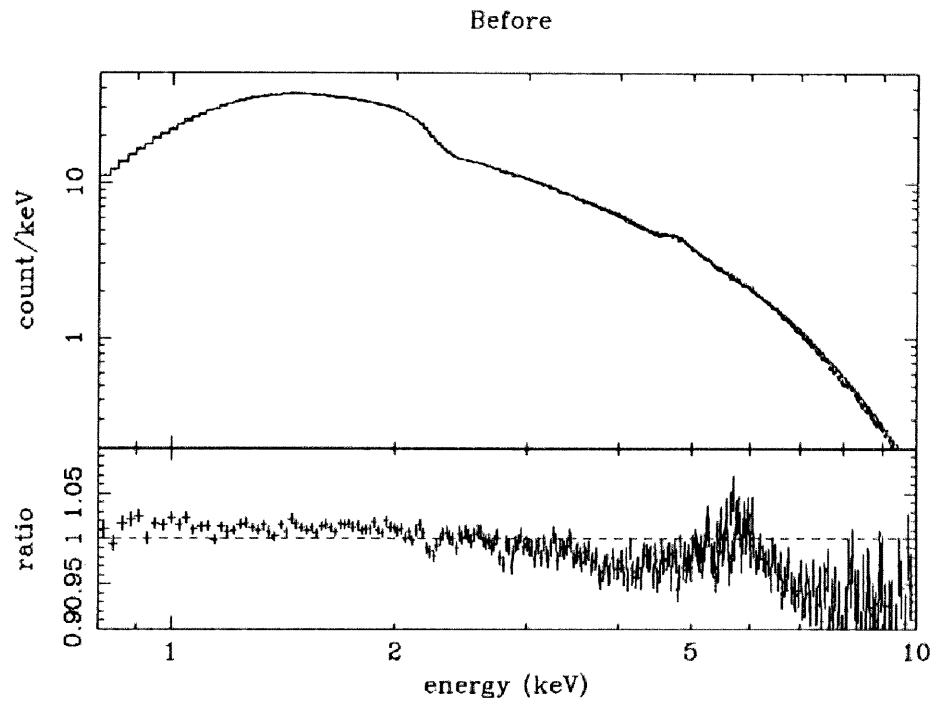
The details of the adjustment have reported by Tsusaka (1994?) and Watanabe (1995). At present, the residuals have been less than 2% using the effective area table; `xrt_ea_v2_1.fits`. However, the ambiguity due to the uncertainty of the extension of the Crab nebula and off-axis angle during the observation is still remained. This may cause 5% discrepancy. Then this is the accuracy of the effective area table⁴(figure 4.15).

²Recently, these constant has been revised ([Henke, Gullikson & Davis 1993]). However, at present, the revised constants has not been used in the ray-tracing program.

³We assumed the point source.

⁴At the current status of the standard analysis tools, `xrt_ea_v2_1.fits` has not been released yet officially. Then guest observers uses the filter called 'ARFFILTER' has been used. This filter make the effective area table change to eliminate the structure appeared in the residuals obtained by the Crab spectrum fitting with the current version of the effective area table; `xrt_ea_v2_0.fits`.

Figure 4.15: The results of the Crab spectrum fitting. Top: before adjustment, Middle: after 1st adjustment (xrt_ca_v1_1.fits), Bottom: after 2nd adjustment (xrt_ca_v2_1.fits).



PSF adjustment

Since the ray-tracing program for *ASCA* XRT had been developed to reproduce the average performance of XRT, azimuthal dependence of PSF was not considered except for the quadrant boundaries and masked area. As the first step, the parameters of image blurring (parameters 2 - (b), 2 - (c), 2 - (d)) had been tuned by the radial distribution of flux averaged over the azimuthal angles. However, high quality GIS images of Cyg X-1 obtained in PV phase revealed the extended profile at both sides of the quadrant boundary, so-called 'Horns' (figure 4.16). The azimuthal information becomes necessary to investigate an asymmetric intensity distribution of diffuse sources such as clusters of galaxies.

Sector No. 2 and 13 in each quadrant mainly contribute to producing the image at both sides of the quadrant boundary. As noted in section 4.4.2, the foils have free ends and the image produced in the sector No. 1 and 14 are much broader than those of other sectors. Since the figure error is still large even in the sector No. 2 and No. 13, the 'Horns' seem to appear. This figure error seems to be seen in large scale. Then the parameters of mm-scale figure error (2 - c) in the sector No.2 and 13 have been given to be 6 times larger than those of other sectors. The parameter tuning was done using the image of GROJ 1008 observed near the optical axis of the XRT. For tuning, the GIS images were used because GIS has larger field of view and capability to observe bright sources. The off-axis angles of observations are listed in Table 4.3.

After 'Horn' tuning, while the discrepancy of radial profile of 'Horn' still remains, it reduced to 20 \sim 40 % (figure 4.16). For further investigations to reproduce the 'Horn' profile, it seems to be necessary to consider the characteristics of each XRT. This tuning also improved the radial profile averaged over whole azimuthal angles. The systematic discrepancy became less than 10 % (figure 4.17).

Next, we compared the simulated profile with the Cyg X-1 image observed at larger off-axis angle than GROJ (6 arcmin. \sim 17 arcmin., table 4.4). Cyg X-1 had been observed at six different positions in the field of view till the tuning phase. The attitude of spacecraft was stable when Cyg X-1 was observed at position 0, 4 and 5, while the attitude is not stable and systematically shifted at the position 1, 2 and 3 observations. Then we used the data of position 0, 4 and 5 observations. The off-axis angle of observations are listed

Table 4.3: Off-axis angle of the targets for 'Horn' tuning

Targets	GIS-2	GIS-3
3C273	5.6'	9.7'
GROJ1008	0.9'	4.6'

Figure 4.16: 'Horn' tuning. Top : GROJ1008 GIS image, Middle : Simulated image before tuning, Bottom : Simulated image after tuning

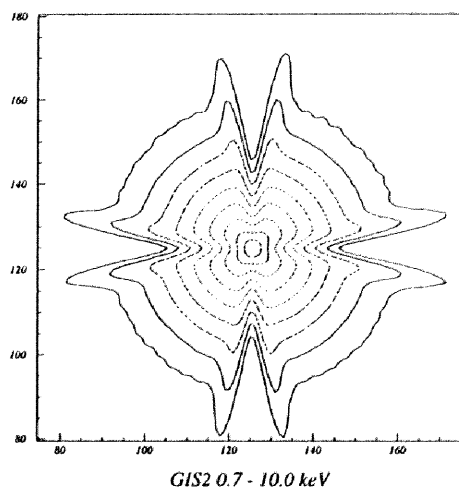
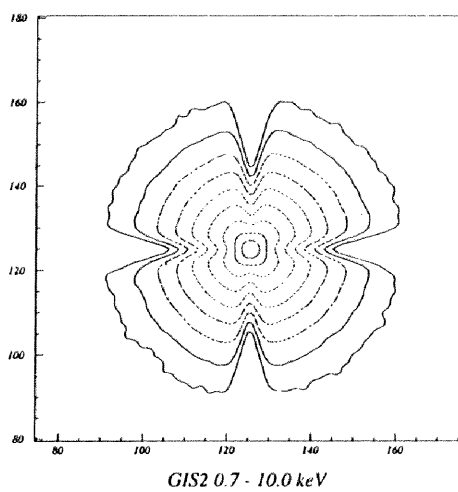
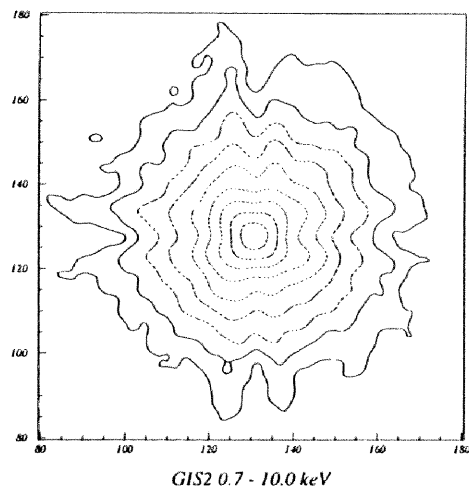
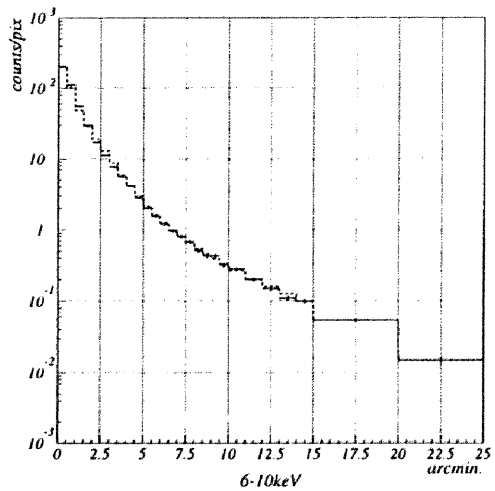
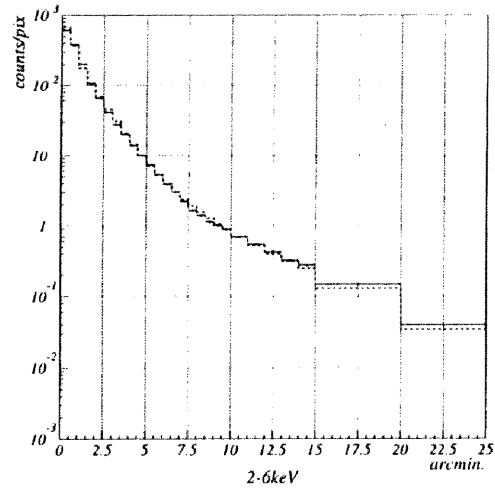
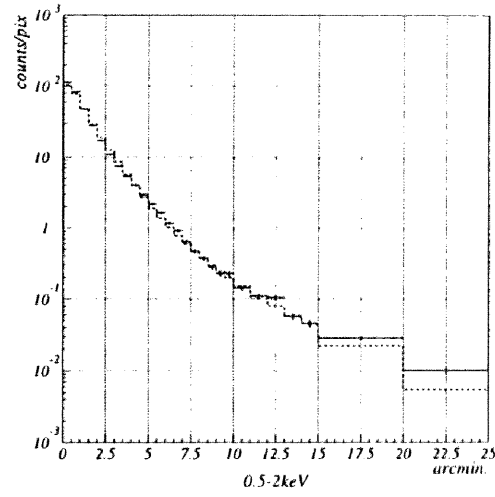


Figure 4.17: Radial profile of GROJ1008 (G2) after tuning. The perpendicular axis shows the brightness (counts/pixel) and the horizontal axis shows the radius from the image peak. Crosses are the observed data and dashed lines are the simulated profiles. TOP : 0.5 - 2 keV band Middle : 2 - 6 keV band, Bottom : 6 - 10 keV band



in Table 4.4.

In comparison to the Cyg X-1 radial profile excluded the 'Horn', the discrepancy between the data and the simulation is less than 10 % within the radius of 10 arcmin. at all energies and off-axis angles. At larger radii than 10 arcmin., the observed profiles show the systematic excess from simulated profiles and the systematic excess become large at larger radii from 10 % at 15arcmin. to 20 % at 20arcmin. (figure 4.18) for the position 0 observation. At larger off-axis angles (position 4 and 5), the systematic excess becomes large at the radii larger than 10 arcmin. (30 ~ 50 %) in the all energy band (figure 4.19). Then we re-tuned the parameter 2 – (c) for the sector No. 3 – 12. After the second tuning, the systematic excess seen in large off-axis angle observations (position 4, 5) has been reduced to 20% at radii smaller than 15 arcmin. (figure 4.20, 4.21, 4.22).

For SIS, we used 3C273 data obtained by 1 CCD mode. While the reliable radial profile is available only within 6 arcmin (for 1CCD mode) due to the small field of view of 1CCD (11 mm \times 11 mm), there is no broadening effect due to the detector in different to GIS. The observed radial profile averaged over all azimuthal angles is good agreement with the simulation of 3C273 within the radius of 6 arcmin. The discrepancy is less than 10 % (figure 4.23).

Table 4.4: Off-axis angle of Cyg X-1 observations for 2nd tuning

Position	GIS-2	GIS-3
P0	8.1'	5.8'
P4	17.0'	12.8'
P5	12.9'	12.7'

Figure 4.18: Radial profile of Cyg X-1 position 0 and simulation before 2nd tuning. Top Left : GIS2 2 - 6 keV band, Bottom Left : GIS2 6 - 12 keV band, Top Right : GIS3 2 - 6 keV band, Bottom Right : GIS3 6 - 12 keV band

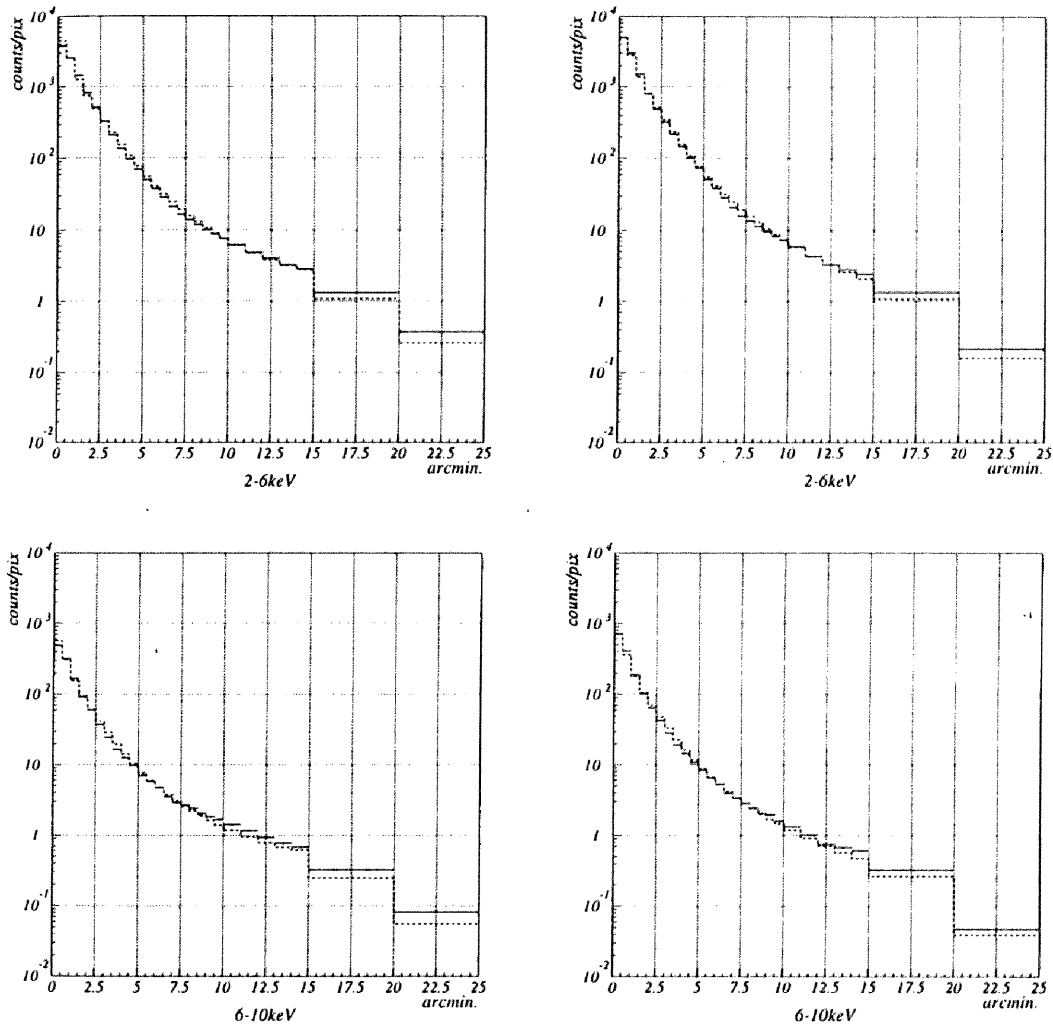


Figure 4.19: Radial profile of Cyg X-1 position 4 and simulation before 2nd tuning. Top Left : GIS2 2 - 6 keV band, Bottom Left : GIS2 6 - 12 keV band, Top Right : GIS3 2 - 6 keV band, Bottom Right : GIS3 6 - 12 keV band

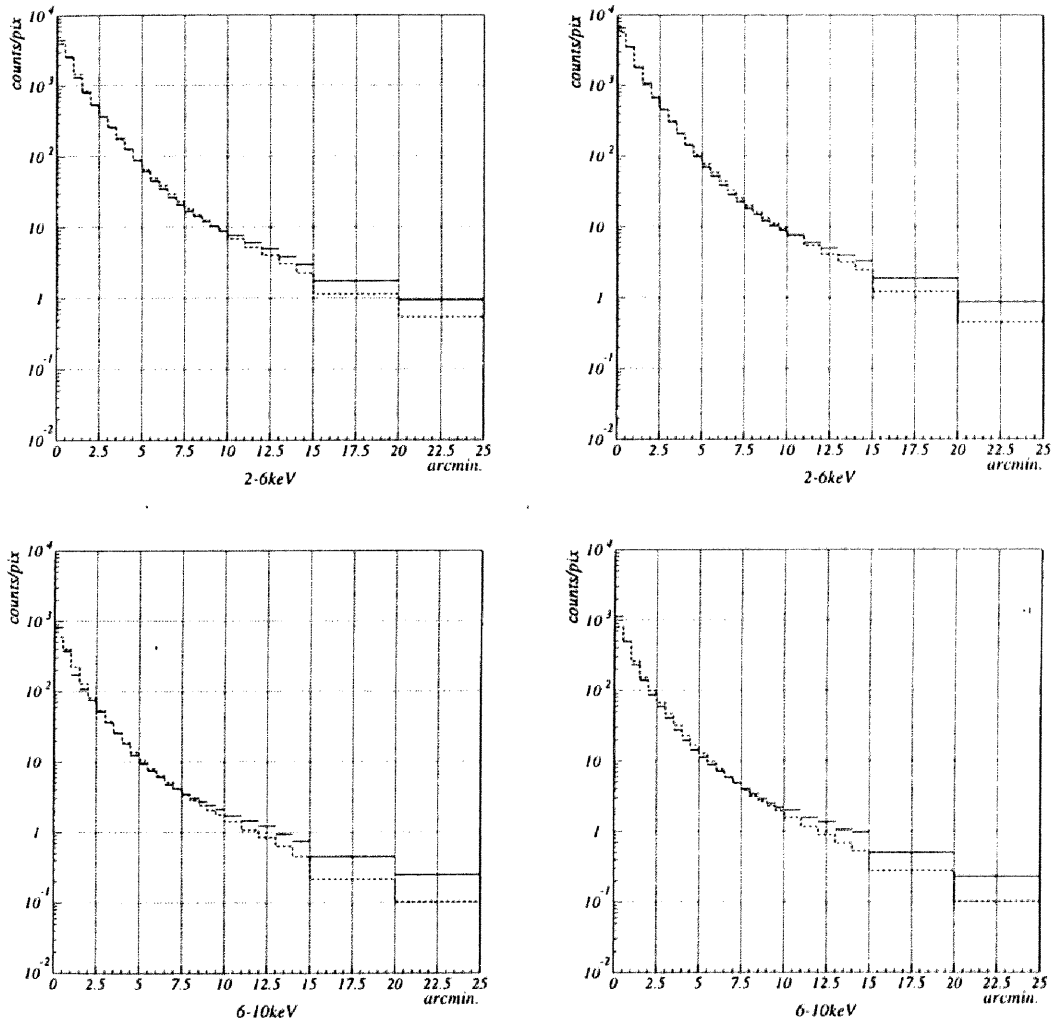


Figure 4.20: Radial profile of Cyg X-1 position 0 and simulation after 2nd tuning. Top Left : GIS2 2 - 6 keV band, Bottom Left : GIS2 6 - 12 keV band, Top Right : GIS3 2 - 6 keV band, Bottom Right : GIS3 6 - 12 keV band

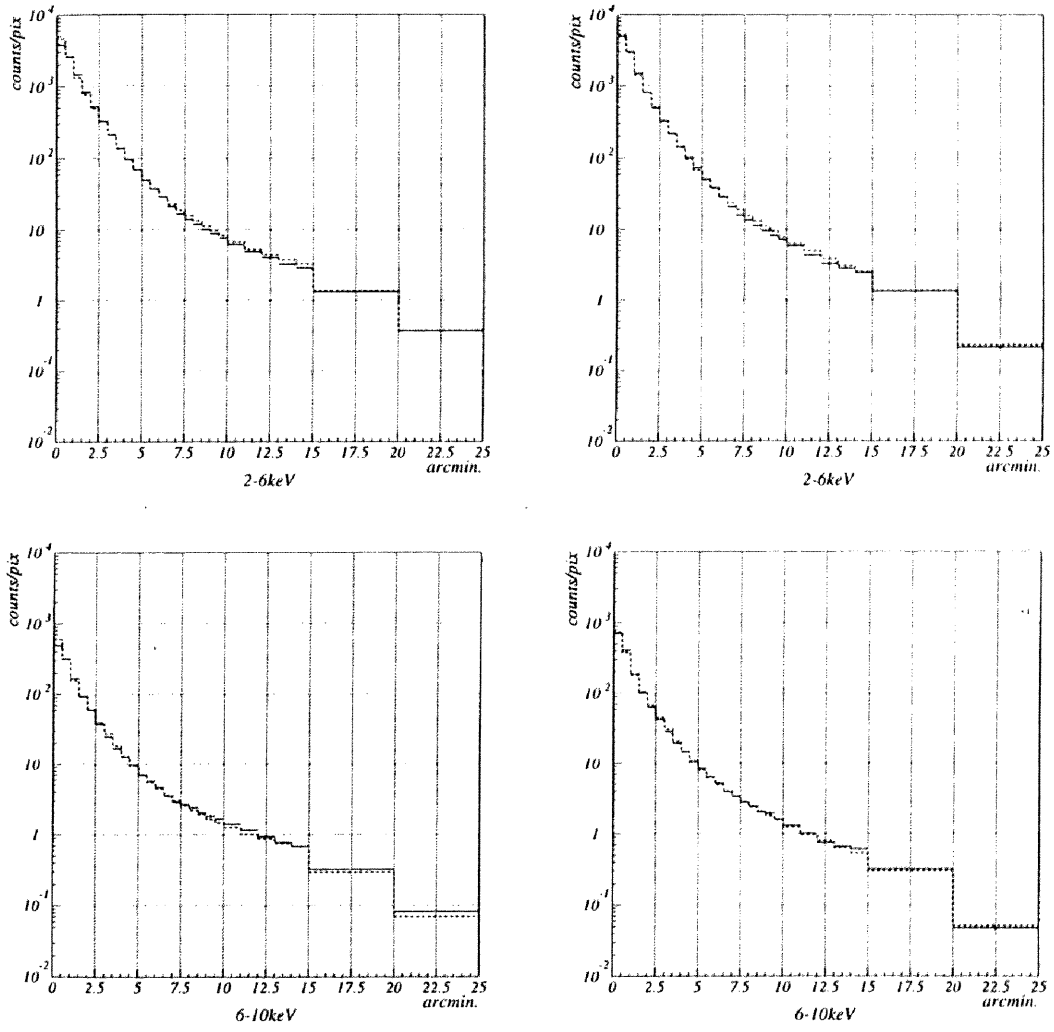


Figure 4.21: Radial profile of Cyg X-1 position 4 and simulation after 2nd tuning. Top Left : GIS2 2 - 6 keV band, Bottom Left : GIS2 6 - 12 keV band, Top Right : GIS3 2 - 6 keV band, Bottom Right : GIS3 6 - 12 keV band

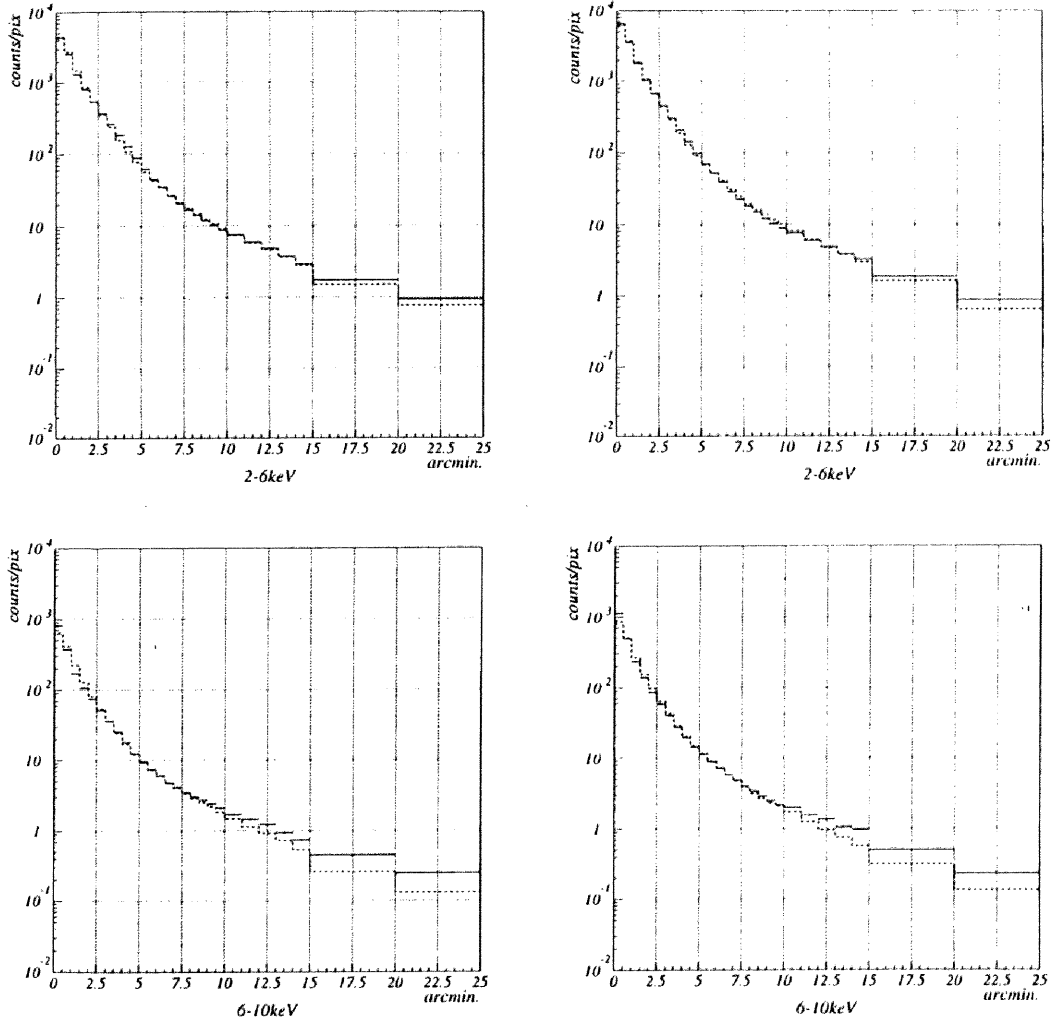


Figure 4.22: Radial profile of Cyg X-1 position 5 and simulation after 2nd tuning. Top Left : GIS2 2 - 6 keV band, Bottom Left : GIS2 6 - 12 keV band, Top Right : GIS3 2 - 6 keV band, Bottom Right : GIS3 6 - 12 keV band

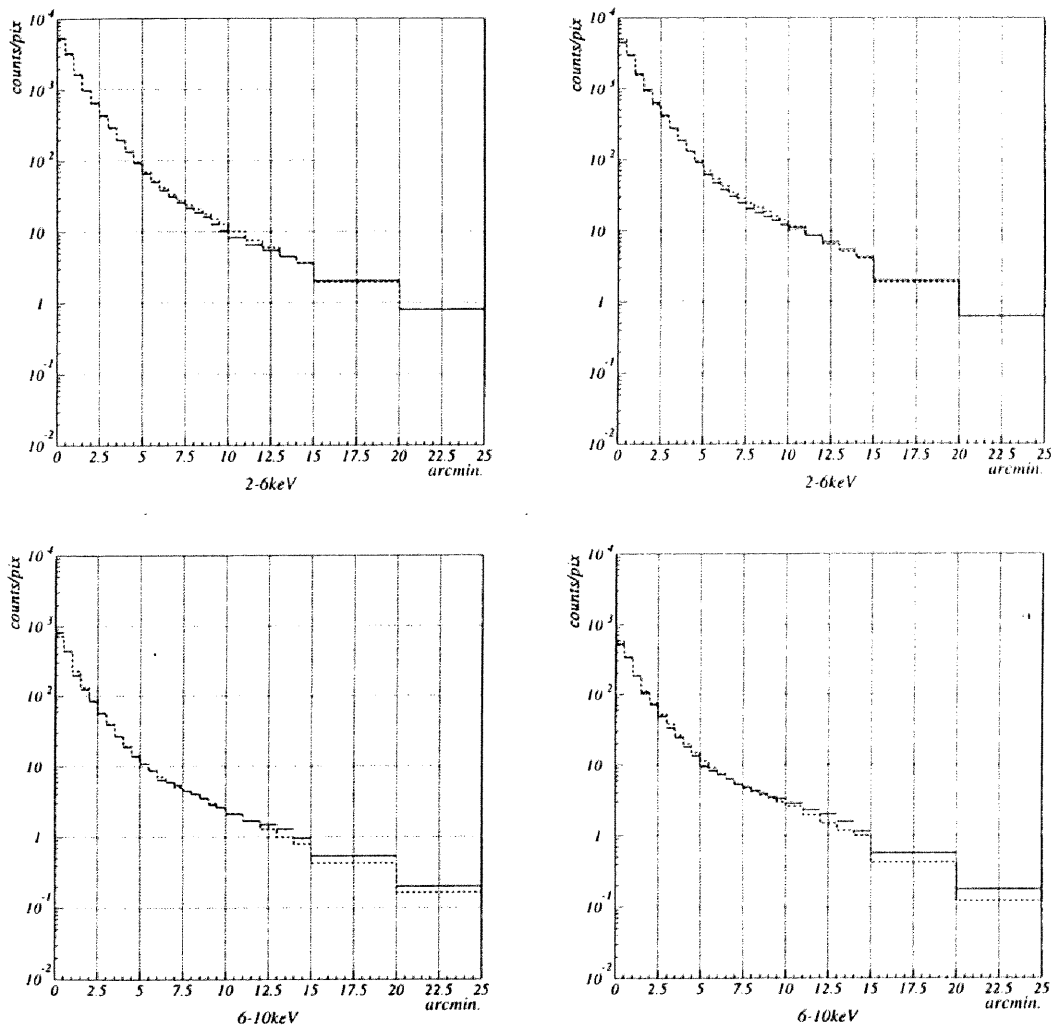
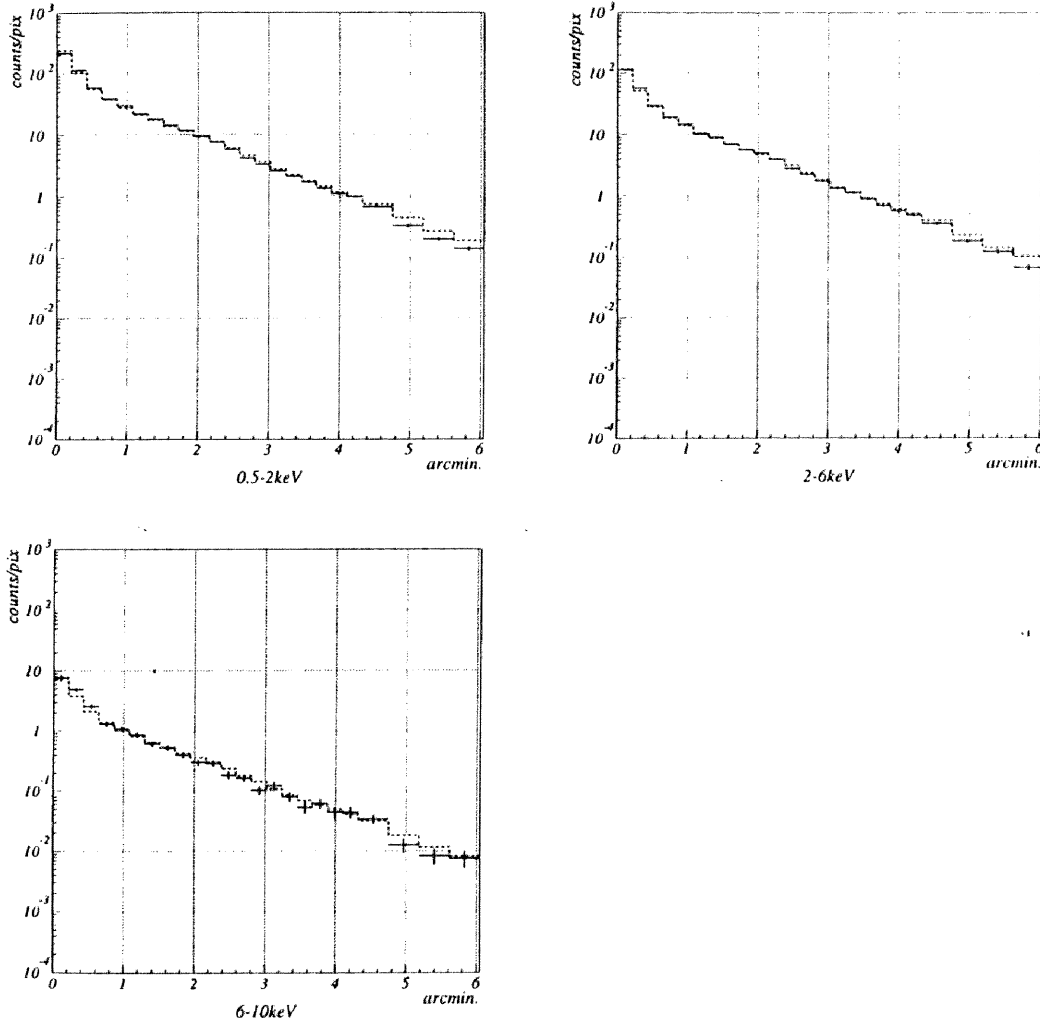


Figure 4.23: Radial profile of 3C273 obtained by SIS0 and simulation after 2nd tuning.
 Top Left : 0.5 - 2 keV band, Top Right : 2 - 6 keV band, Bottom : 6 - 10 keV band



Chapter 5

Analysis of X-ray emission from Clusters of Galaxies

We analyzed *ASCA* data of 6 distant clusters of galaxies by the identical method. In this section, we describe the analysis method.

XSELECT, XSPEC and FTOOLS which are the standard analysis tools developed at Goddard Space Flight Center (GSFC), NASA, are used for data reduction, correction, selection (XSELECT) and spectral fitting (XSPEC). The calibration database and versions of softwares used here are listed in Table 5.2.

5.1 Data reduction

X-ray photons are observed one by one. The output pulse of detector is called as event or count. The raw data after on-board data reduction include non-X-ray events other than the X-ray events.

The non-X-ray events are caused by particles of primary cosmic ray and of secondary produced by high energetic photons. The counting rate of non-X-ray events is well correlated with the cut-off rigidity (COR) for GIS¹. COR is defined as the charged particle's minimum momentum for reaching to the surface of the earth against the electro-magnetic force of terrestrial magnetism at a satellite position. Then COR is described as the function of a satellite position. When the satellite passes through the low COR region in the orbit, the counting rate of non-X-ray events becomes high. Moreover, there is one region called as 'South Atlantic Anomaly (SAA)' in which the density of the charged particle is extremely high. Around this region, the counting rate of non-X-ray events is also high.

The X-ray events include the solar emission scattered by the earth's atmosphere when the earth rim is contained in the field of view. Furthermore, for SIS0, the leakage of

¹For SIS, there is little correlation between COR and the counting rate of non-X-ray events, because CCD has smaller volume than GIS.

optical light has been seen on the detector plane when the angle between the direction of the XRT and that of bright earth rim is small.

In order to avoid the contamination described above, the following data have been selected according to the selection criteria,

- The data obtained at the outside of SAA for both of GIS and SIS.
- The data obtained when COR is less than 6 GeV/c for both of GIS and SIS.
- The data obtained during the elevation is greater than 5° for both GIS and SIS. The elevation is the angle between the direction of XRT and that of the earth surface.
- The data obtained during the elevation from the bright earth is greater than 25° for SIS.

The resultant exposure time after above reduction will be shown in section 6 for each target and summarized in Table 6.10.

5.2 Spectral analysis

In order to obtain the plasma parameters of the hot intracluster medium, the energy spectrum was integrated within a radius centered at the brightness peak of cluster and fitted by the model spectrum. To investigate the azimuthally averaged temperature variation, the results obtained with the several annular integration regions were compared with each other. Adopted boundary radii are 1.5, 3, 6, 9 and 12 arcmin. for GIS and 1.5, 3, 6 arcmin. for SIS. However, for CL0016+16, 3, 6, and 8 arcmin. for GIS and, 3 and 6 arcmin. for SIS have been adopted because of the poor statistics in the small region. Corresponding radii in Mpc units for each target are listed in Table 5.1.

Table 5.1: Adopted Integration radius (Assuming $H_0 = 50$ and $q_0 = 0$)

Target	Redshift	radii (Mpc)
A1413	0.143	0.3, 0.6, 1.2, 1.8, 2.5
A2218	0.171	0.4, 0.7, 1.4, 2.1, 2.8
A665	0.182	0.4, 0.7, 1.5, 2.2, 3.0
A773	0.217	0.4, 0.8, 1.7, 2.6, 3.4
CL0016+16	0.545	1.5, 3.0, 4.1

The integrated spectrum includes the cosmic X-ray background (CXB) and detector internal background. To obtain the X-ray spectrum of the target, these background events have to be subtracted. Since the distant clusters are faint and diffuse X-ray source, it is possible that the results are dependent on the background subtraction method, especially, for CL0016+16. There are two different methods to get background spectra. One is the way to use the background spectra integrated within a circle of 6' radius in the source free sky region of the present field of view. We picked three different center positions at the same off axis angle as that of the source detected position. Another kind of background spectrum is obtained from superposed several different blank field accumulated in much longer exposure for the CXB observations.

Totally, four background spectra were adopted; one of these is integrated in the superposed blank field and others are integrated in source free region of the same field of view of each target. Then we compared the result with each other.

The spectral parameters are obtained by fitting the simulated spectrum for appropriate X-ray emission model to the observed spectrum. In this thesis, Raymond-Smith model in XSPEC were used as the emission model and abundance units $[\text{Fe}]/[\text{H}] = 4.68 \times 10^{-5}$ were used. In this fitting process, the model spectrum is produced by multiplying the intrinsic intensity of emission model by the XRT effective area (which depends on the observed off-axis angle, source brightness distribution and integration region) and detector efficiency (which depends on the position) in each energy bin. For extended source, the XRT response is complicated because the directions of incident photons are not parallel (see Section 4.4).

We used the software 'ASCAARF' included in FTOOLS for making the energy response. This software calculates the XRT and detector efficiency for each pixel in a given brightness distribution and the average of these efficiencies to give the total response. However, in this process, the observed brightness distribution was used for the calculation of the efficiencies. The observed image suffered the energy dependent broadening effect due to the XRT PSF. Then the total efficiency built by above process is overestimated.

For the distant clusters we analyzed here, the angular sizes are far smaller than that of the nearby clusters and similar to the point source. Then we compared the results obtained with the extended source response to that obtained with the point source response². The temperature and abundance obtained with the extended source response are consistent with those obtained with point source response. For the X-ray flux, the extended source response give us about 10~15% higher value than the point source response systematically.

²We used the software 'ASCAARF' and 'JBLDARF' for making the point source response and also compared the results with each other. 'JBLDARF' has been developed by the hardware calibration team in Japan([?]) and distributed from ISAS.

Since it seems that the true value is in between those values, we derived the median of those values as the X-ray flux and 15% of this value as the error of it.

We also deduced the cluster redshift from the line center energy of Fe-K line. For high temperature clusters ($kT > 5$ keV), the light elements (low-Z element) are almost fully ionized and the iron becomes He-like and H-like ion. Then the X-ray emission is well described as the bremsstrahlung and Fe-K line emission. Then we fitted the observed spectra to the model which consists of bremsstrahlung emission and gaussians and derived the line center energy.

5.3 Image analysis

For the spectral analysis, since the distant clusters is faint X-ray source and its spectral data is statistically poor, systematic error due to the change of the off-axis angle is less than the statistical error. For example, the systematic error of the temperature is ~ 0.5 keV. Therefore the instability of attitude control is not serious for our spectral analysis. However, for image analysis, it can affect the evaluation of brightness profile. Then we excluded the data which obtained during the term in which the attitude was systematically shifted from the average above $0.2'$.

Next, in order to examine the energy dependence of brightness distribution, we compared the radial profiles between different energy bands. Considering the photon statistics, we selected the two energy bands; 0.5-2.5keV and 2.5-10.0keV for SIS, 0.7-2.5keV and 2.5-10.0keV for GIS.

For the clusters analyzed in this thesis, most of all show the symmetrical shape on the *ASCA* spatial resolution.³ Then the azimuthally averaged (one dimensional) radial profile were adopted for the image analysis. The peak position of intensity distribution were defined as the center of circle ($r = 1'$) in which flux became maximum.

Since the brightness becomes about one hundredth of peak brightness at the position $8'-10'$ apart from the center and is comparable to the background surface brightness, the background subtraction is important. As same as the method adopted for spectral analysis, we compared the result obtained by the subtraction of superposed blank sky image (normalized with the exposure time) with that obtained by subtracting the averaged brightness in the source free region of the present field of view.

To evaluate the radial profile, β model were used (section 2.4.2, equation 2.10). Because the observed brightness profile are distorted by the extended XRT point spread

³*ROSAT* has better spatial resolution than that of *ASCA*. The brightness distributions obtained by *ROSAT* show the small scale asymmetry.

function which has complicated energy and off-axis angle dependence as shown in section 4.4.3, the observed radial profile can not be compared to the profile of β model immediately. Then we made the template profiles of β model passed through the XRT using the ray-tracing simulation (section 4.4.3). The template profiles are made for the each parameter set ; Energy (1.2, 4.0, 7.0keV), off-axis angle(0, 5, 10, 15arcmin.), phase angle(0, 45 degree), θ_c (0.1arcmin. pitch, 0.1 \sim 5.0 arcmin.) and β (0.02 pitch, 0.5 \sim 1.0).

We calculated the χ^2 's in the (θ_c, β) plane at appropriate energy, off-axis angle and phase angle for the targets, and searched for the parameter set at which χ^2 became minimum. Assuming the bremsstrahlung emission at $kT = 8\text{keV}$, intensity weighted average photon energy at rest frame is 1.4 keV in 0.5-2.5keV band and 5.7keV in 2.5-10keV band, respectively. Then the template profiles of $E = 1.2\text{keV}$ for 0.5-2.5 keV band image and that of $E = 4.0\text{ keV}$ for 2.5-10 keV band image were used. The propriety and uncertainty in this profile evaluation will be discussed in section 8.

Table 5.2: Software and Files for data analysis

Software Versions	
XSPEC	9.00
FTOOLS	3.5.2
JBLDARF	2.10
XRT Raytrace	5.0
Calibration files	
XRT	
EA, PSF	xrt_ea_v2.0.fits, xrt_psf_v2.0.fits (with/without arfilter) xrt_ea_v1.1.fits, xrt_psf_v1.1.fits
GIS	
Tel. def. file	gis2_ano_on_ff_180295.fits, gis3_ano_on_ff_180295.fits
Be map	s2bev1.fits, s3bev1.fits
Grid map	s2gridv3.fits, s3gridv3.fits
Gain history file	gainhist_931101.ghf.v2 (for the targets observed before 1993/11/01) File made by temp2gain version 3.6 (after 1993/11/01)
RTI boundary	rti_gis_1024_040693.fits
SIS	
Tel. def. file	s0_teldef_070294.fits, s1_teldef_070294.fits
Echo correction	sisechos_290296.fits
PHA to PI conversion	sisph2pi_290296.fits
Detector Response Matrix (RMF)	
GIS	gis2v4.0.rmf, gis3v4.0.rmf
SIS (Faint mode)	s0c?g0234p40e0.512v0.8h.rmf, s1c?g0234p40e0.512v0.8h.rmf s0c1g0234p40e0.512v0.8i.rmf, s1c3g0234p40e0.512v0.8i.rmf
(Bright mode)	s0c?g0234p40e1.512v0.8h.rmf, s1c?g0234p40e1.512v0.8h.rmf s0c1g0234p40e1.512v0.8i.rmf, s1c3g0234p40e1.512v0.8i.rmf

Chapter 6

Results of ASCA data analysis of the individual targets

1. Cl0016+16
2. A773
3. A665
4. A2218
5. A1204
6. A1413
7. Fe-K emission line study

6.1 CL0016+16

6.1.1 Introduction

CL0016+16 at redshift 0.541 ± 0.001 ([Koo 1981]) is notable for its extreme richness and its absence of a dominant optical galaxy. The galaxy distribution of CL0016+16 shows NE-SW elongation with an axial ratio of ~ 0.6 and core radius of 46 arcsec. It is classified as Bautz-Morgan type II-III from its galaxy distribution ([Koo 1981]). This cluster is one of the best studied clusters at this high redshift in connection to the Butcher-Oemler effect ([Butcher & Oemler 1978]). This cluster had been considered as the counter example for the Butcher & Oemler effect, since most of galaxies within 3' are very red and old ([Koo 1981], [Butcher & Oemler 1984]). Recent observations revealed that this cluster contains a large fraction of E+A galaxies ([Fabricant, McClintock & Bautz 1991], [Belloni & Röser 1996]). Since these galaxies are considered to have been past a few Gyr after synchronous star formation (starburst), it proved that this cluster is not the counter example for the Butcher-Oemler effect.

CL0016+16 has been known as extremely luminous X-ray cluster. The temperature of ICM in this cluster has not been known, because this cluster detected by instruments with telescopes only. These instruments have limited energy band and a difficulty to decide the temperature. *GINGA* which has a good ability to obtain the temperature could not detect this cluster. The imaging instruments provided the lower limit of temperature from *Einstein* IPC ([White *et al.* 1981]) and the range of 6 to 10 keV from *ROSAT* PSPC ([Neumann & Bohringer 1996]).

Einstein ([White *et al.* 1981]) observation obtained a soft X-ray image. White *et al.* (1981) derived core radius $\theta_c = 30''$ and central surface brightness $l_0 = 3.7 \times 10^{-4}$ ergs $s^{-1} cm^{-2}$ from *Einstein* HRI data using β model. However because of the poor statistics they fixed $\beta = 0.5$. Recent *ROSAT* observation obtained the parameters; $(\theta_c, \beta) = (0.7', 0.74)$ ([Hughes & Birkinshaw 1995]), $(0.83', 0.80)$ ([Neumann & Bohringer 1996]).

6.1.2 Observation

The observation of CL0016+16 was carried out from July 19 through 20 in 1993 at the 2CCD nominal position where the source image comes to the boundary of 2 of four chips of each SIS detector. The angular distance of this source from each optical axis of XRTs ranges is 3.4', 8.4', 6.0' and 6.2' for SIS0, SIS1, GIS2 and GIS3, respectively. GIS worked in the PH mode and SIS worked in the 4CCD Faint and Bright mode. After the data reduction, the resultant exposure time was ~ 36000 sec for GIS and ~ 24000 sec for SIS. Source counting rates were ~ 0.05 cts s^{-1} for GIS and ~ 0.06 cts s^{-1} for SIS within the circle of 3' radius centered on the cluster. Details are listed in Table 6.10.

6.1.3 Results

X-ray spectra

The spectrum obtained from each detector (energy band; 0.7–10 keV for GISs, 0.5–10 keV for SISs) are fitted with Raymond& Smith model incorporated with the neutral hydrogen absorption on the line of sight (figure 6.1) separately. The obtained parameters are consistent with each SIS and GIS detectors. For next step, the same model is applied to each pair of detectors, GIS2+GIS3 and SIS0+SIS1. Though the best fit N_H of $(1.4 \pm 1.0) \times 10^{21} \text{ cm}^{-2}$ for GIS2+3 is slightly larger than that for SISs, the value of $(5.8 \pm 2.9) \times 10^{20} \text{ cm}^{-2}$ obtained with SIS0+SIS1 is very close to the galactic value of $5.0 \times 10^{20} \text{ cm}^{-2}$ decided from radio data. Since SIS has better sensitivity to N_H , the absorption column density is fixed at the galactic value in the following fittings. Then the temperature and abundance obtained from simultaneous fitting for GIS2+3 and SIS0+1 are $8.0_{-0.8}^{+1.0} \text{ keV}$ and $0.11_{-0.11}^{+0.12}$ relative to the cosmic (cosmic : $n(Fe)/n(H) = 4.0 \times 10^{-5}$)(90% confidence uncertainties).

Our result is slightly dependent on the background subtraction method. However, the temperatures from one of the detectors with four different background files showed 3.5% standard deviation. We used the background spectra from the CXB observations for the spectral analysis mentioned above, because it has the best statistics and the other methods also show essentially consistent results.

When we extend the radius of integration, there is a small decrease in the averaged temperature (Table 6.1). It, however, can not be concluded that there is temperature gradient because of relatively large error bars in the present data set. Further investigation of the temperature distribution require longer exposure observations. For the following spectral analysis, we use the data integrated within 6' radius, because of good statistics and the well calibrated response of the telescope system.

As far as line features are concerned, the poor statistics still prevent us from obtaining a definitive answers. For example, iron line feature expected at 6.7keV (rest frame) is not clearly seen. Since iron is the only element which is not fully ionized in such a hot plasma of several keV, its abundance is essentially decided by the equivalent width of the iron K line feature. However the upper limit of the Fe abundance quoted above is not inconsistent with that derived for other high redshift clusters of galaxies([Mushotzky 1996]).

X-ray images

Figure 6.2 shows the X-ray image obtained with SIS0. This image is not background subtracted. Note that the valley like structure in figure 6.2 running from NW to SE is due to lack of data at the boundary of 2 CCD chips. Figure 6.3 is the azimuthal averaged surface brightness distribution of SIS0 image after background subtraction, based on the

background map from the superposed blank field accumulated in much longer exposures for the X-ray background observations. It is clear that the CL0016+16 is more extended than the distribution expected for a point source as shown in figure 6.3 with solid line.

An additional point source is seen at 3.5' away from the cluster center, which coincides with the QSO 0015+162. 30 photons are found within the circle of 1' diameter centered at the AGN. Assuming that all these photons come from the AGN, the intensity of the AGN is less than 0.003 cts s⁻¹. When we integrate the cluster flux within 6' radius, the contamination from this point source is estimated to be 5% based on a detailed ray-tracing of the *ASCA* XRT spatial response function and thus the AGN dose not give a serious impact on the X-ray spectra or structure of the cluster.

For most X-ray bright clusters of galaxies, the X-ray surface brightness distribution looks relatively axially symmetric and the radial profile is well fitted by the iso-thermal β model.

Inspection of the archival *ROSAT* PSPC image of CL0016+16 shows that it is slightly elliptical. A detailed analysis of the cluster by Neumann and Bohringer(1996) confirm this impression. However, The eccentricity is small (0.18) and also well fitted to the spherical symmetric β model.

For this cluster, we could not divide into two energy band in difference to other clusters we analyzed because of the poor statistics. Then we fitted the radial profile obtained by *ASCA* in the energy range 0.5 – 10 keV to the iso-thermal β model.

In figure 6.4, the confidence level contours for 90 and 99% are plotted against the parameters of θ_c and β . The best fit values obtained with *ASCA* $\theta_c = 0.6'$ and $\beta = 0.70$ are consistent with those obtained from *ROSAT* PSPC.

The dispersion of best fit values due to the different background subtraction methods (using superposed blank sky and source free region in the field of view, see section 5) is very small and within the statistical error.

6.1.4 Discussion

Averaged gas temperature

The best fits temperature of $8.0^{+1.0}_{-0.8}$ keV in the present observation is well above the lower limit of 6 keV obtained from previous observations with *Einstein*. In general, plasma temperature of clusters is highly correlated with X-ray luminosity; $L_x \propto kT^a$. If we use the 2–10keV luminosity of 3.5×10^{45} ergs s⁻¹ ($H_0 = 50$ km/sec/Mpc, $q_0 = 0$), the plasma temperature of CL0016+16 is predicted to be about 10keV, according to the correlation established for low redshift ($z < 0.1$) clusters by *EXOSAT* ME observations ([Edge & Stewart 1991], $a = 3.57$) and by *Einstein* MPC, *EXOSAT* ME, *GINGA* and *HEAO-1* observations ([David *et al.* 1993], $a = 3.45$). Recently, a similar correla-

tion between temperature and luminosity of cluster ($z < 0.2$) has been obtained with *ASCA* data ([Tsuru et al. 1995], [Kumada et al. 1996], $a \sim 3.5$). Its extrapolation also suggests about 10keV for CL0016+16. Preliminary *ASCA* results for distant clusters are not sufficient in the number of samples at present to determine if the L_x vs. kT relationship is the same at high redshift([Kumada et al. 1996], [Mushotzky 1996]).

Spatial distribution

The core radius is strongly coupled with β for *ASCA* data due to the moderate spatial resolution of *ASCA* XRT and the low S/N ratio at the large radii (~ 1 at $r > 6'$). The *ROSAT* best fit value are very consistent with the *ASCA* value, while the value from *Einstein* HRI is not, probably because the HRI image is rather poor (see Fig 1a of the paper by [White et al. 1981]). The *ROSAT* data are much more consistent as well. We will use the θ_c and β contours by *ASCA* or *ROSAT* for the density distribution to derive the Hubble constant. For the X-ray flux *ASCA* results will be used, since it dose not depend strongly on the θ_c and β in different to the central surface brightness. The error of the X-ray flux due to the uncertainty of the intrinsic surface brightness distribution is definitely smaller than the flux callibration error because of its small extended, point-like image in the case of CL0016+16.

The detailed analysis of *ROSAT* PSPC and HRI image shows that there is the surface brightness excess region at 1.5' west from the cluster center ([Neumann & Bohringer 1996]). The authors concluded that there is an extended source in the line of sight and this might be a subgroup falling into the cluster main body. If this cluster is a strong merger one might expect the system to show a non-isothermal temperature structure([Markevitch 1996]). Unfortunately, the image could not be divided into several energy bands due to the limitation of photon statistics. Thus the temperature gradient mentioned in the section 6.1.3 has not been confirmed. The present data are not of sufficient quality or of spatial resolution to show such effects. There is no evidence of a temperature gradient in the *ROSAT* PSPC data([Neumann & Bohringer 1996]).

Table 6.1: ICM temperature and X-ray flux of CL0016+16

Integration radius (arcmin.)	kT (keV)
< 3	$10.0^{+2.3}_{-1.7}$
< 6	$8.0^{+1.0}_{-0.8}$
< 8	$7.4^{+1.2}_{-1.0}$
2-10 keV flux : $(1.64 \pm 0.16) \times 10^{-12}$ ergs s $^{-1}$ cm $^{-2}$	

Figure 6.1: CL0016+16 spectrum. Top: GIS, Bottom: SIS

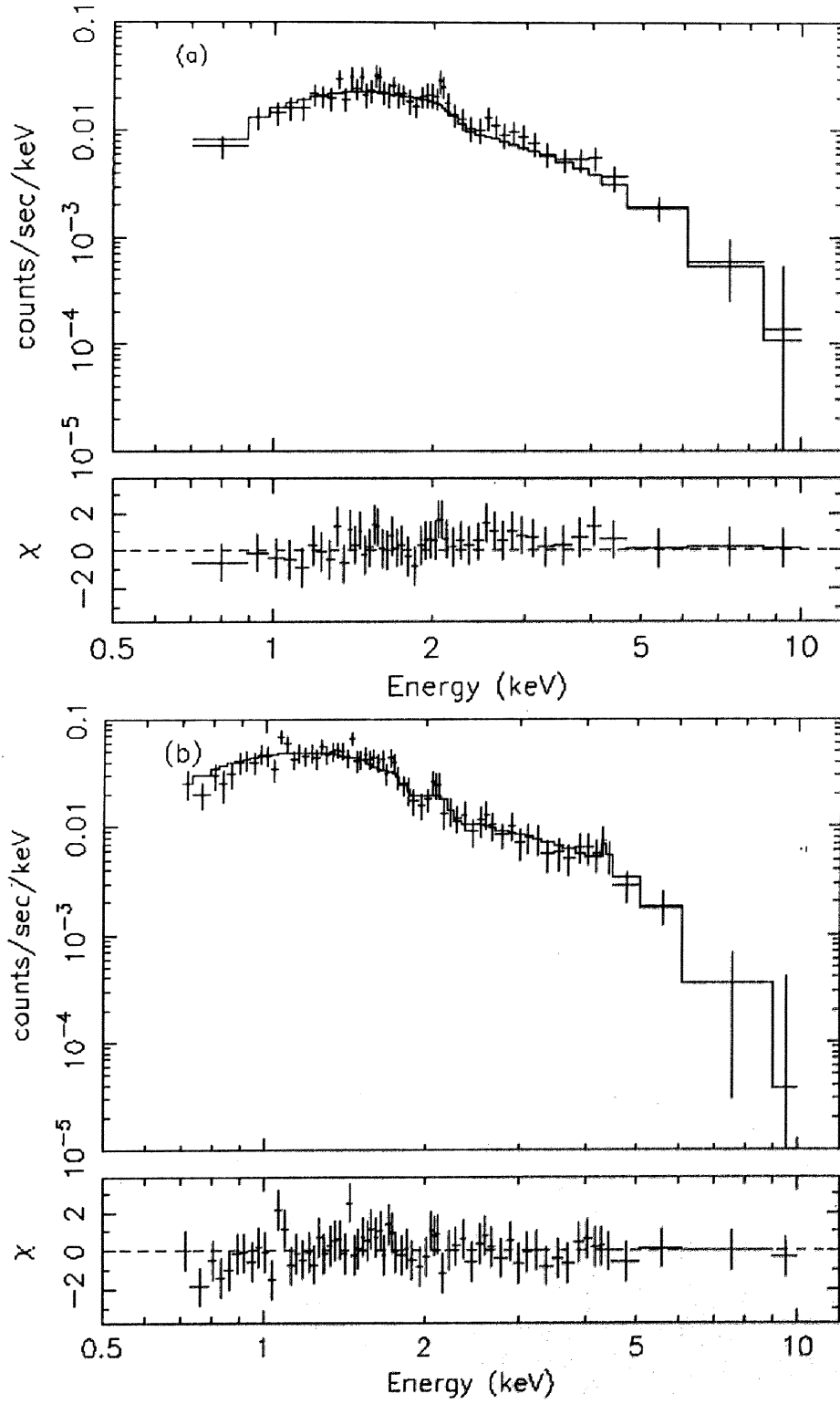


Figure 6.2: CL0016+16 X-ray brightness contour map placed on the optical image. Left: GIS, Right: SIS, Top: 0.5-2.5 keV, Bottom: 2.5-10.0keV

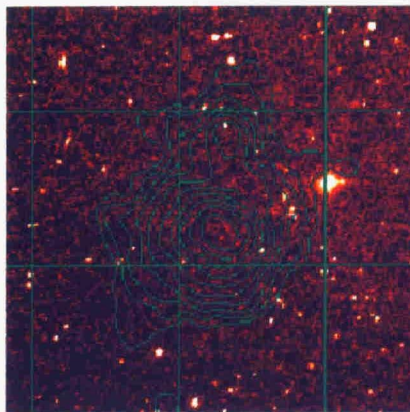
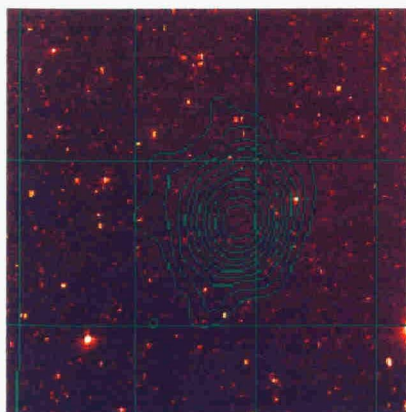
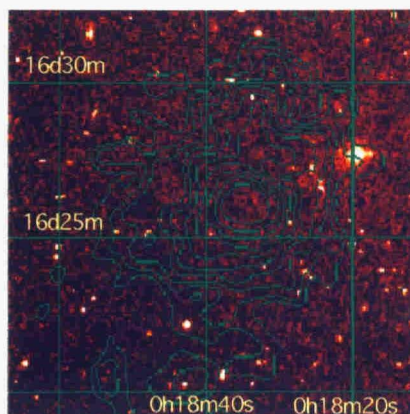
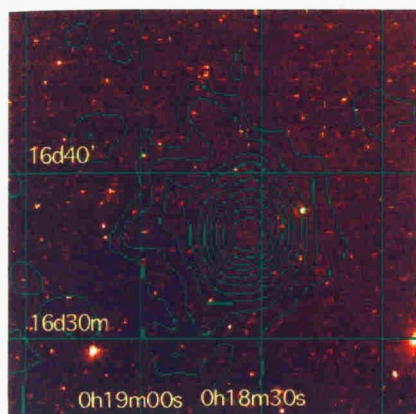


Figure 6.3: Radial profile of the observed surface brightness for CL0016+16 by SIS0. Solid line is the simulated profile with the bestfit parameters of β model. The Dashed line shows the expected radial profile for a point source.

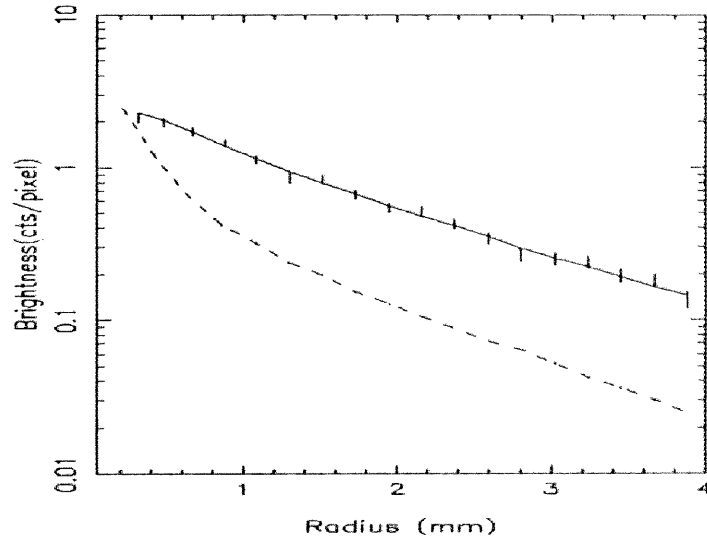
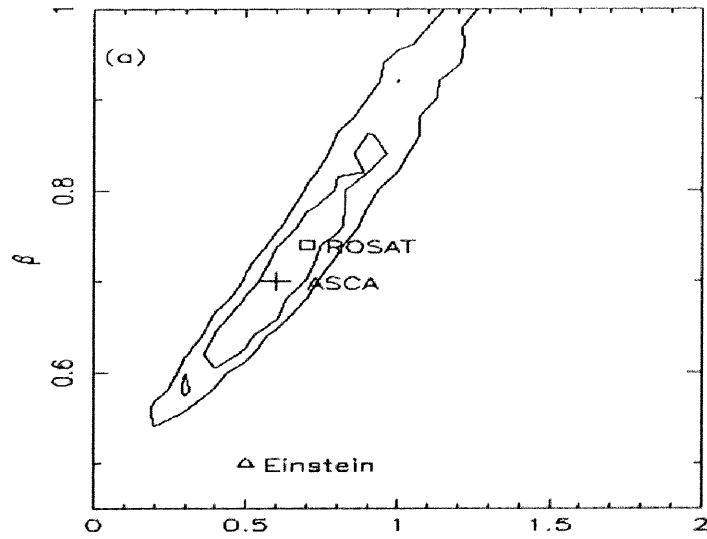


Figure 6.4: Confidence level contours for (θ_c, β) obtained by the β model fitting to the SIS0 radial profile. 90% and 99% confidence level contours and the bestfit values obtained by *ASCA*(cross), *ROSAT*(box) and *Einstein*(triangle) are plotted.



6.2 A773

6.2.1 Introduction

The Distant cluster A773 is at a redshift of 0.217 ([Crawford et al. 1993]) and classified as richness class 2, Bautz-Morgan type II-II ([Abell, Corwin & Olowin 1989]) and Rood-Sastry type 'B' ([Struble & Rood 1991]). This cluster has compact galaxy distribution and no central dominant galaxy.

This cluster has not been studied in all wavelengths. In the X-ray, it was not observed by *Einstein* and *ROSAT* in the pointing observations but observed during the *Einstein* slew survey and *ROSAT* all sky survey. From *Einstein* slew survey data, the luminosity in 2-10 keV band is 6×10^{44} ergs s⁻¹.

6.2.2 Observation

ASCA observed A773 from November 22 to 23 in 1994. It was observed at 1 CCD nominal position. The instruments were working in the PH normal mode for GIS and 1 CCD Faint mode for SIS. The off-axis angle is 8.2', 10.1', 9.6' and 6.48' for SIS0, SIS1, GIS2 and GIS3. The effective exposure time after data reduction was 43000 sec for GIS and 39000 sec for SIS.

6.2.3 Results

X-ray Spectra

The integrated spectra for each circular region were fitted to the Raymond-Smith model with photo absorption. While the fitting results from the individual instruments are slightly different, the results show no systematic difference and are distributed randomly. Then the simultaneous fitting for GISs and SISs spectra has been done (figure 6.5) and results are summarized in table 6.2. The source spectra subtracted the several different background spectra (integrated in the superposed blank sky and three source free regions in the field of view, independently) shows the consistent results. Then it is confirmed that obtained values do not depend on the background subtraction methods we adopted.

The fitted hydrogen column density, 4.1×10^{20} cm⁻² is higher than the galactic value obtained by Stark et al. (1992); 1.8×10^{20} cm⁻². When the column density is fixed at the galactic value, the fitted temperature becomes ~ 1 keV high. Other parameters are not changed (Table 6.2). The parameters has no strong dependence on the integration radius. However, the value of temperature becomes large with increasing the integration radius (from 8.6 keV to 9.5 keV). The change of the abundance seems to be connected with the increase of the fitted temperature, because the Fe K α line emissivity (including the

He-like and H-like $K\alpha$ lines) decrease with increasing the temperature at this temperature range (the emissivity becomes maximum around 6.5keV).

X-ray image

Figure 6.6 show the X-ray image obtained with GIS2 and SIS0 from which the background is not subtracted. For the β model fitting, the background has to be subtracted. Figure 6.7 show the 0.5-2.5 keV and 2.5-10 keV band radial profiles after background subtraction.

Since this cluster observed 1 CCD mode, it is not possible to estimate the background brightness from the source free region in the field of view because of extending cluster emission by PSF. Then we estimated the averaged background brightness from the source free regions in the various observations of distant clusters; ~ 0.05 cts/pixel. The background subtracted radial profile within the radius of 5' was fitted to the β model and fitted χ^2 distribution as a function of (θ_c, β) were obtained as shown in figure 6.8. Though the averaged background brightness has large ambiguity, it is not influent to the fitted result because of limitation of range of radius for fitting (At $r = 5'$, the signal to noise ratio is about 4). Figure 6.9 show the fitted results using the different background levels, which are the minimum and maximum levels obtained from the source free regions in the various observations of distant clusters. For 2.5-10 keV band, Figure 6.8 (bottom) were obtained. The best fit β in 2.5-10keV band is less than that in 0.5-2.5keV band.

6.2.4 Discussion

In section 6.2.3, the integration radius dependence of the spectral parameters have been shown. Furthermore, β model fitted results show that hard(higher energetic) photons has broader distribution than the soft photons and the temperature in the outer region may be higher than that in the inner region. As noted above, in the cluster which contains strong merging component (merger), there might be the non-isothermal and asymmetrical temperature structure. However, at the outer region ($>$ radius of 6'), it is difficult to determine the temperature with accuracy 20%, which is necessary to reveal the temperature difference. Further background study for low source brightness region is needed. The radial dependence of hardness ratio (figure 6.10), suggests the temperature distribution can be well described by iso-thermal model within the radius of 6 arcmin' in the scale of the spatial resolution of the *ASCA* XRT.

Table 6.2: Results of Spectral fitting for A773 (N_H fixed at the galactic value of $1.8 \times 10^{20} \text{ cm}^{-2}$)

Integration region(arcmin.)	kT (keV)	Abundance
$0.0 < r < 3.0$	$8.6^{+0.6}_{-0.6}$	$0.17^{+0.08}_{-0.07}$
$0.0 < r < 6.0$	$9.4^{+0.6}_{-0.6}$	$0.18^{+0.07}_{-0.07}$
$0.0 < r < 9.0$	$9.5^{+0.7}_{-0.5}$	$0.21^{+0.08}_{-0.07}$
$0.0 < r < 12.0$	$9.5^{+0.8}_{-0.5}$	$0.20^{+0.08}_{-0.08}$
2-10keV flux : $(6.77 \pm 1.02) \times 10^{-12} \text{ ergs s}^{-1} \text{ cm}^{-2}$		
redshift : 0.23 ± 0.02		

Table 6.3: Results of Spectral fitting for A773 (N_H free)

Integration region (arcmin.)	$N_H(10^{20} \text{ cm}^{-2})$	kT (keV)	Abundance
$0.0 < r < 3.0$	$4.5^{+1.5}_{-1.7}$	$7.7^{+0.8}_{-0.6}$	$0.17^{+0.08}_{-0.07}$
$0.0 < r < 6.0$	$4.4^{+1.2}_{-1.5}$	$8.4^{+0.6}_{-0.5}$	$0.18^{+0.07}_{-0.07}$
$0.0 < r < 9.0$	$4.1^{+1.4}_{-1.3}$	$8.7^{+0.7}_{-0.6}$	$0.21^{+0.08}_{-0.07}$
$0.0 < r < 12.0$	$4.3^{+1.4}_{-1.3}$	$8.7^{+0.8}_{-0.7}$	$0.20^{+0.08}_{-0.08}$
2-10keV flux : $(6.66 \pm 1.00) \times 10^{-12} \text{ ergs s}^{-1} \text{ cm}^{-2}$			
redshift : 0.23 ± 0.02			

Figure 6.5: A773 spectra. Top: GIS, Bottom: SIS

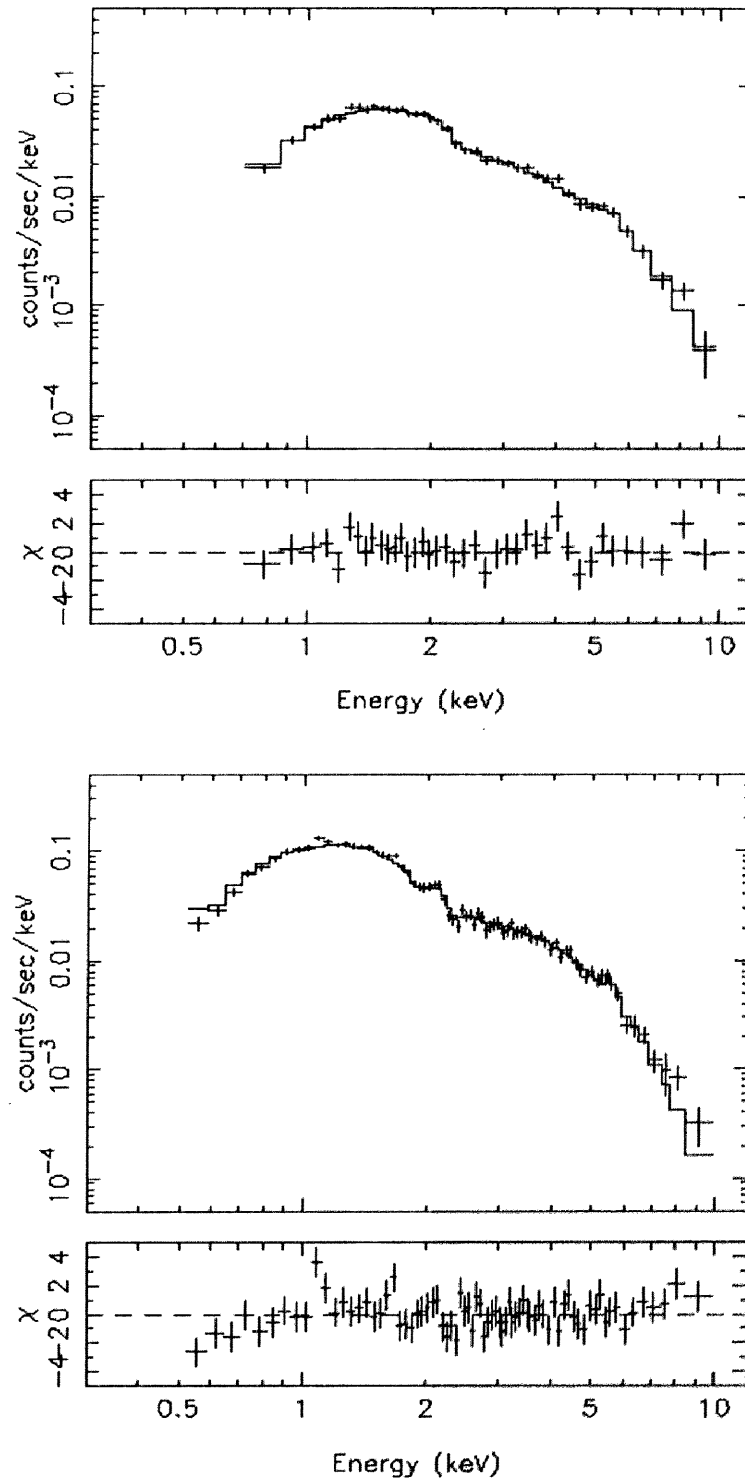


Figure 6.6: A773 X-ray brightness contour map overlaid on the optical image. The background is not subtracted. Left: GIS, Right: SIS, Top: 0.5-2.5 keV, Bottom: 2.5-10.0 keV

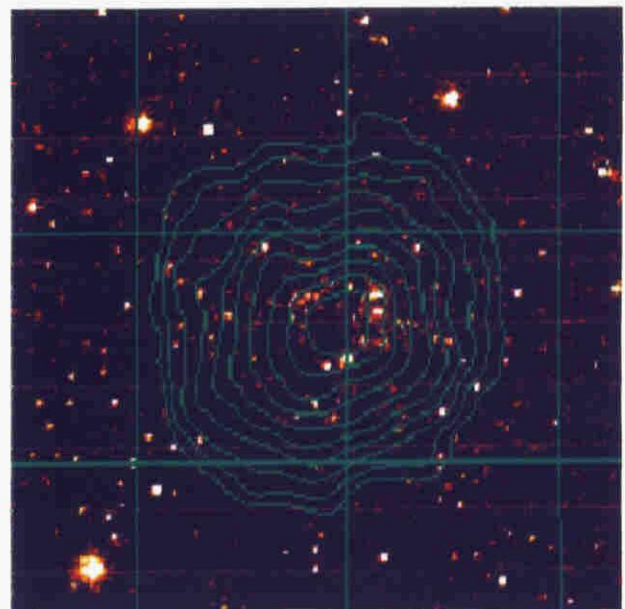
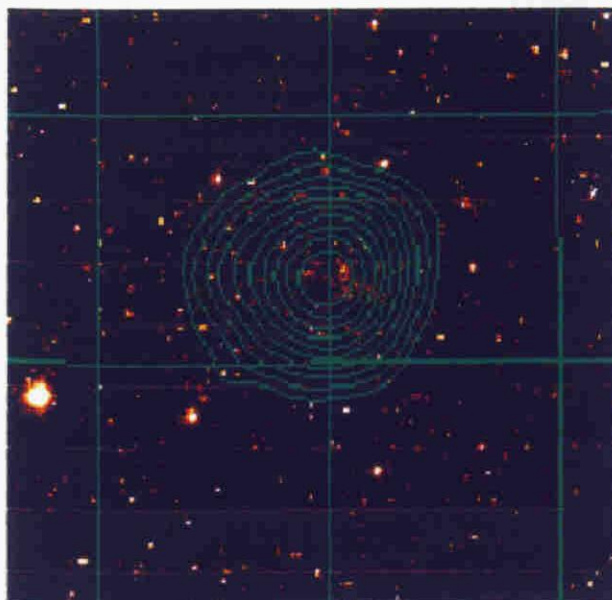
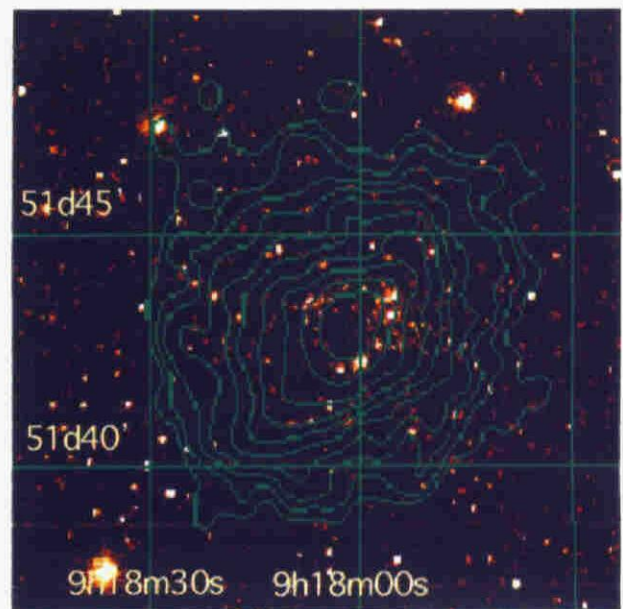
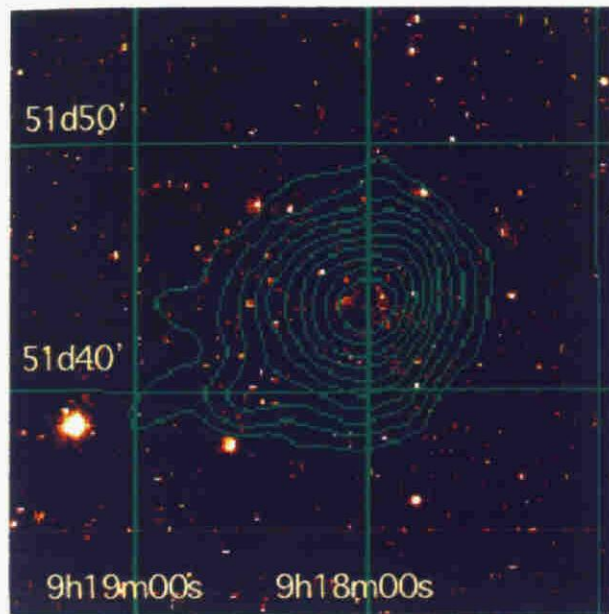


Figure 6.7: A773 Radial profile of surface brightness obtained with SIS0. The best fitting β model profile also shown with solid line. Top:0.5-2.5keV, Bottom:2.5-10keV

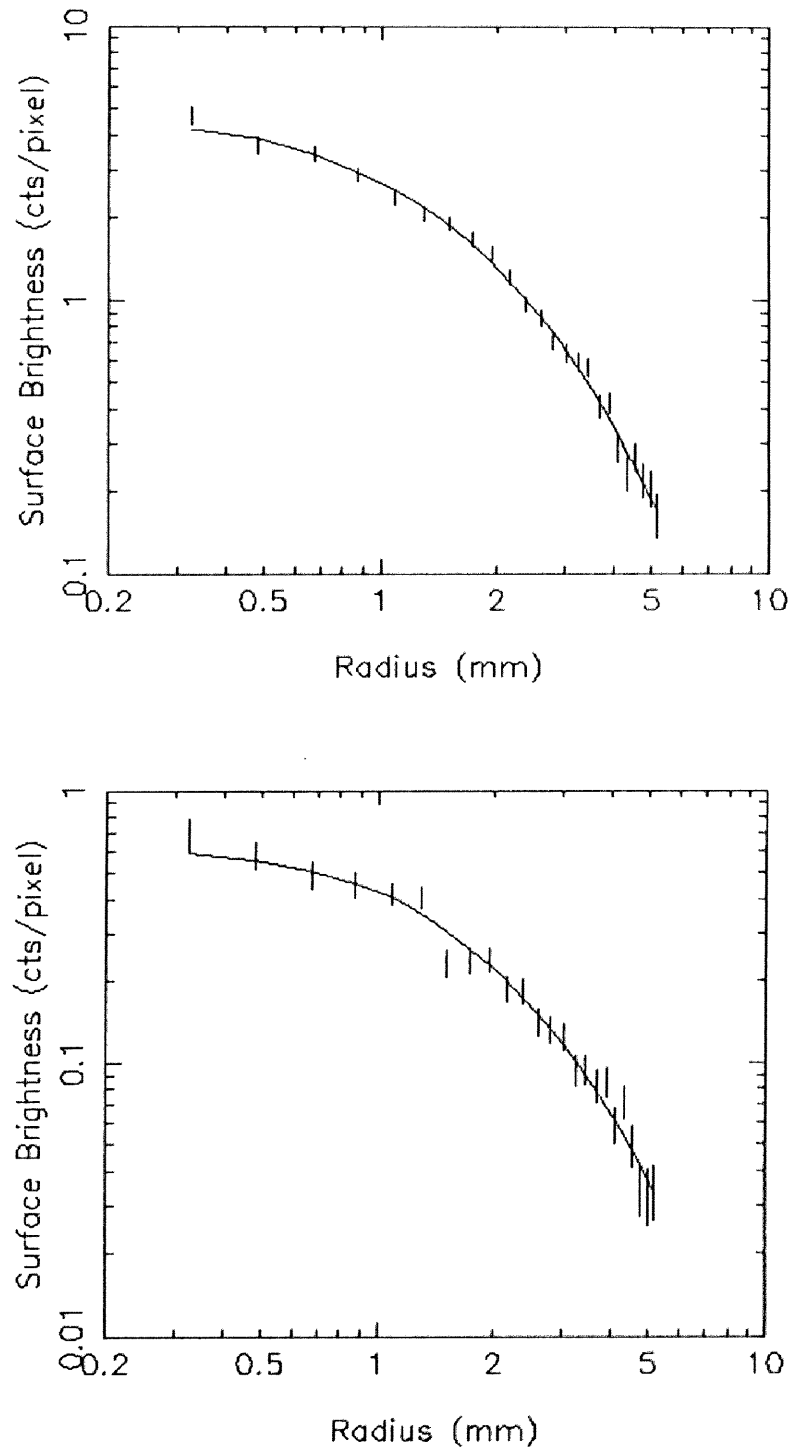


Figure 6.8: Confidence level contours for (θ_c, β) obtained by the β model fitting to the SIS0 radial profile. The background level is 0.05 cts/pixel which is averaged from various observations of distant clusters. 90% and 99% confidence level contours and the bestfit values obtained by *ASCA*(cross). Top:0.5-2.5keV, Bottom:2.5-10keV

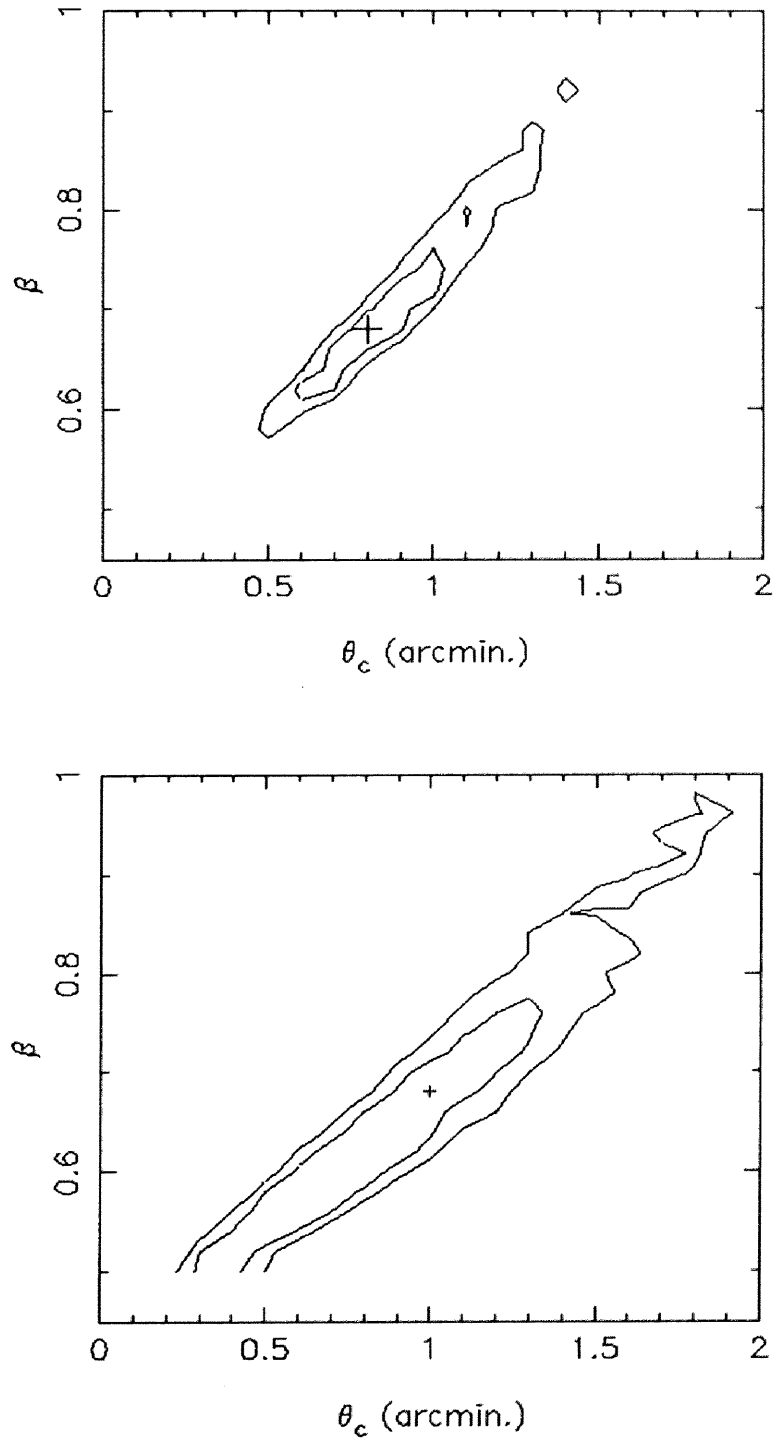


Figure 6.9: Confidence level contours for (θ_c, β) obtained by the β model fitting to the SIS0 0.5-2.5 keV radial profile with different background level. The bestfit values obtained by *ASCA*(cross). Top: background level = 0.03 cts/pixel, Bottom: background level = 0.07 cts/pixel

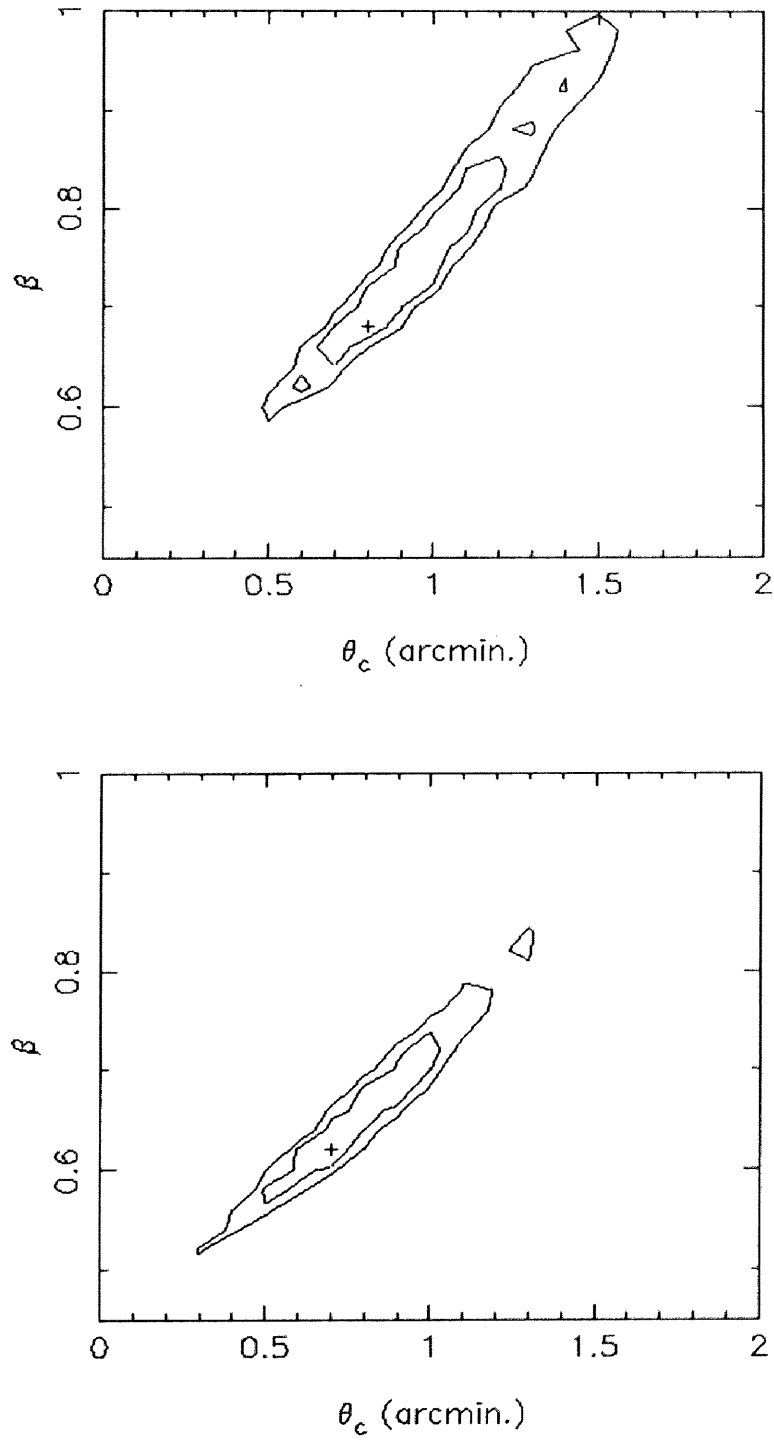
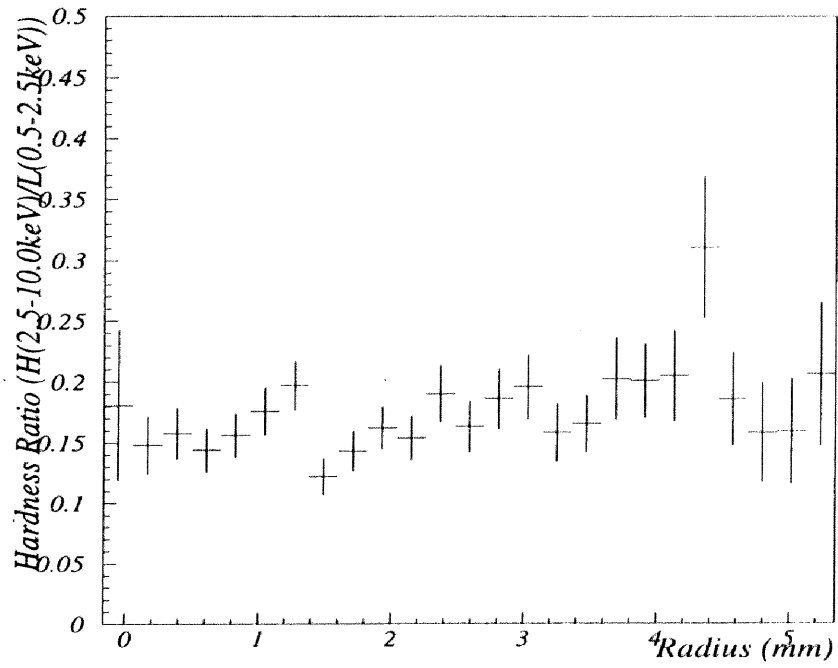


Figure 6.10: Radial dependence of the hardness ratio (2.5-10 keV)/(0.5-2.5 keV).



6.3 A665

6.3.1 Introduction

A665 is a distant at redshift 0.182 and richest among clusters in the Abell's catalogue. This cluster has been classified as richness class 5 and Bautz-Morgan type III ([Abell, Corwin & Olowin 1989]). In the Rood-Sastry morphological classification system, its classified as 'C (core)' ([Struble & Rood 1991]) and the galaxy concentration is relatively high in comparison to other BM type III clusters.

GINGA observed this cluster and obtained averaged temperature and abundance; $kT = 8.2$ keV, abundance 0.42 ($[\text{Fe}]/[\text{H}] = 4.68 \times 10^{-5}$) ([Hughes & Tanaka 1992]). The X-ray luminosity of this cluster is 1.5×10^{45} ergs s^{-1} ([Hughes & Tanaka 1992]). While the obtained temperature is consistent with the temperature predicted from the relation between the luminosity and temperature, abundance is much larger than other hot clusters. From *Einstein* IPC observation, there are three X-ray sources near the Abell 665, $\sim 15'$ apart from the cluster center. These were included in the field of view of *GINGA* LAC and it was impossible to avoid these sources. Since the one of these has very soft spectrum found by IPC spectrum, this is not affective to the temperature determination. Other two sources were identified with active galactic nuclei (AGN). Because the normalization of power-law component turned out to be zero using the sum of the Raymond-Smith model and power-law model as the model spectrum, the authors claimed that the sources did not contribute to the *GINGA* spectrum.

The observation of X-ray brightness distribution of A665 has been done by *Einstein* and *ROSAT*. These instruments can not decide the temperature precisely. The parameters of β model were obtained; $\theta_c = 1.5'$ and $\beta = 0.66$ ([Birkinshaw, Hughes & Arnand 1991]).

6.3.2 ASCA Observation

This cluster has been observed from September 18 to 19 in 1993. The observation mode of instruments were PH normal mode for GIS and 4CCD Bright mode for SIS. The source were placed at the 2CCD nominal position. The angular distance of this source from XRT optical axis is $4.7'$, $9.3'$, $7.1'$ and $7.3'$ for SIS0, SIS1, GIS2 and GIS3, respectively. We have to note that for SIS the peak of brightness distribution might be in the gap of CCD.

After data reduction, the resultant exposure time was about 42000 sec for GIS and 40000 sec for SIS. Details are listed in Table 6.10.

6.3.3 Results

X-ray Spectra

For this cluster, Raymond& Smith model incorporated with the neutral hydrogen absorption on the line of sight has been used for the spectral fitting. The spectra obtained with both SISs and GISs have been fitted to that model simultaneously (figure 6.11). The resulting parameters are $N_H = (5.0 \pm 2.0)^{20} \text{ cm}^{-2}$, $kT = 8.6 \pm 0.4 \text{ keV}$ and the abundance $= 0.2 \pm 0.06$ ($[\text{Fe}]/[\text{H}] = 4.68 \times 10^{-5}$) within the radius of $9'$. Obtained hydrogen column density is well consistent with the galactic value of $4.0 \times 10^{20} \text{ cm}^{-2}$ ([Stark et al. 1992]). Then the hydrogen column density was fixed at the galactic value in the following fitting. The integration radius dependence of these parameters are listed in Table 6.4. The quoted errors in the Table 6.4 are included the statistical error only. It must be noted that these results, with the exception for the abundance and 2-10 keV flux, have relatively large dependence on the background subtraction method in comparison to the results from other clusters we analyzed. The parameters obtained independently from each detector, especially from SIS, are also dispersed in the range of 7.5 - 9.5 keV for the temperature even if the background spectra integrated over the source free region in the field of view during the A665 observation. This seems caused by the flux difference in the energy range of 0.5-0.7 or 7.0-10.0 keV of the background spectra. Then they are the values which we use below to represent the uncertainties for each parameter. If this error has been considered, the dependence on the integration region could not be discussed.

For this cluster, iron K_α lines are clearly seen and K_β lines are also detected as same as A1413. We analyzed the line intensities in detail as shown in the section 6.7 The uncertainty of the background discussed above is not affective for iron line analysis shown in section 6.7.

X-ray Image

Figure 6.12 show the X-ray image obtained with GIS2 and SIS0. Since for SIS, the peak of the surface brightness is very close to the boundary of 2 CCD chips in comparison to other cluster, the peak position for SIS was decided from the peak of GIS images. Figure 6.13 were the azimuthal averaged surface brightness distribution of SIS0 image in the 0.5-2.5 keV and 2.5-10.0 keV band after background subtraction, based on the background map from the superposed blank field accumulated in much longer exposures for the X-ray background observations. Those radial profiles of SIS were fitted to the β model and Figure 6.14 were obtained and best fit values are $\theta_c = 1.1'$ and $\beta = 0.66$. The dispersion of the best fit values due to the different background subtraction methods is within the

90% confidence range.

The fitted results slightly depend on the the peak position for SIS image. When the center to derive the radial profile are shifted about $0.5'$, the best fit position on the $\theta_c - \beta$ plane are shifted along the direction of the elongation of confidence contour within the 99 % confidence range. If the distance between the center we derived and the true center is larger than $0.7'$, the best fit value go out from current 99% range. However, it is hard to consider, because the accuracy of peak position for GIS is less than 1 pixel ($= 0.25mm$).

6.3.4 Discussion

From combined analysis of *ASCA* and *ROSAT* data, Markevitch et al. (1996b) has claimed that there is the strong temperature drop at the $6'-12'$ annulus; 8.3 keV at $r < 6'$, < 4.4 keV at $6' < r < 12'$). For our results, we couldn't discuss the temperature gradient based on the spectral fitted results because of large systematic error, even though the same *ASCA* data were used. From the profile fitted results, which have better statistical quality than the spectrum and is less dependent on the uncertainty of the background flux in the energy range of $0.5-0.7$ and $7.0-10.0$ keV, the large difference between the soft and hard energy bands couldn't be seen. Since this method is less sensitive to the temperature change than the spectral approach and the radial profile within the radius of $7'$ were used for fitting, these is the difficulty to investigate the temperature drop claimed by Markevitch (1996b). However, our fitted result of profile is not consistent with that obtained with *Einstein*. Birkinshaw, Hughes and Arnaud (1991) obtained the best-fit θ_c and β by fitting *Einstein* image to the β model ($\theta_c = 1.5'$ and $\beta = 0.66$). According to this result, the radial profile obtained with *Einstein* is broader than that we obtained. Since the efficiency weighted mean energy of *Einstein* observation is much lower than that of *ASCA* the difference of the profiles between *ASCA* and *Einstein* may suggest the existence of the temperature drop in the outer skirt of brightness.

Table 6.4: Spectral fitting result for A665(Integration radius dependence)

Integration region(arcmin.)	kT (keV)	Abundance
$0.0 < r < 1.5$	$8.8^{+0.8}_{-0.7}$	$0.17^{+0.11}_{-0.10}$
$0.0 < r < 3.0$	$8.8^{+0.5}_{-0.4}$	$0.26^{+0.07}_{-0.07}$
$0.0 < r < 6.0$	$8.7^{+0.3}_{-0.3}$	$0.20^{+0.07}_{-0.06}$
$0.0 < r < 9.0$	$8.6^{+0.4}_{-0.4}$	$0.20^{+0.07}_{-0.05}$
$0.0 < r < 12.0$	$8.6^{+0.4}_{-0.3}$	$0.20^{+0.07}_{-0.05}$
<hr/>		
2-10keV flux : $(1.24 \pm 0.19) \times 10^{-11}$ ergs s $^{-1}$ cm $^{-2}$		
redshift : 0.19 ± 0.01		
<hr/>		

Figure 6.11: A665 spectra. Top:GIS, Bottom:SIS

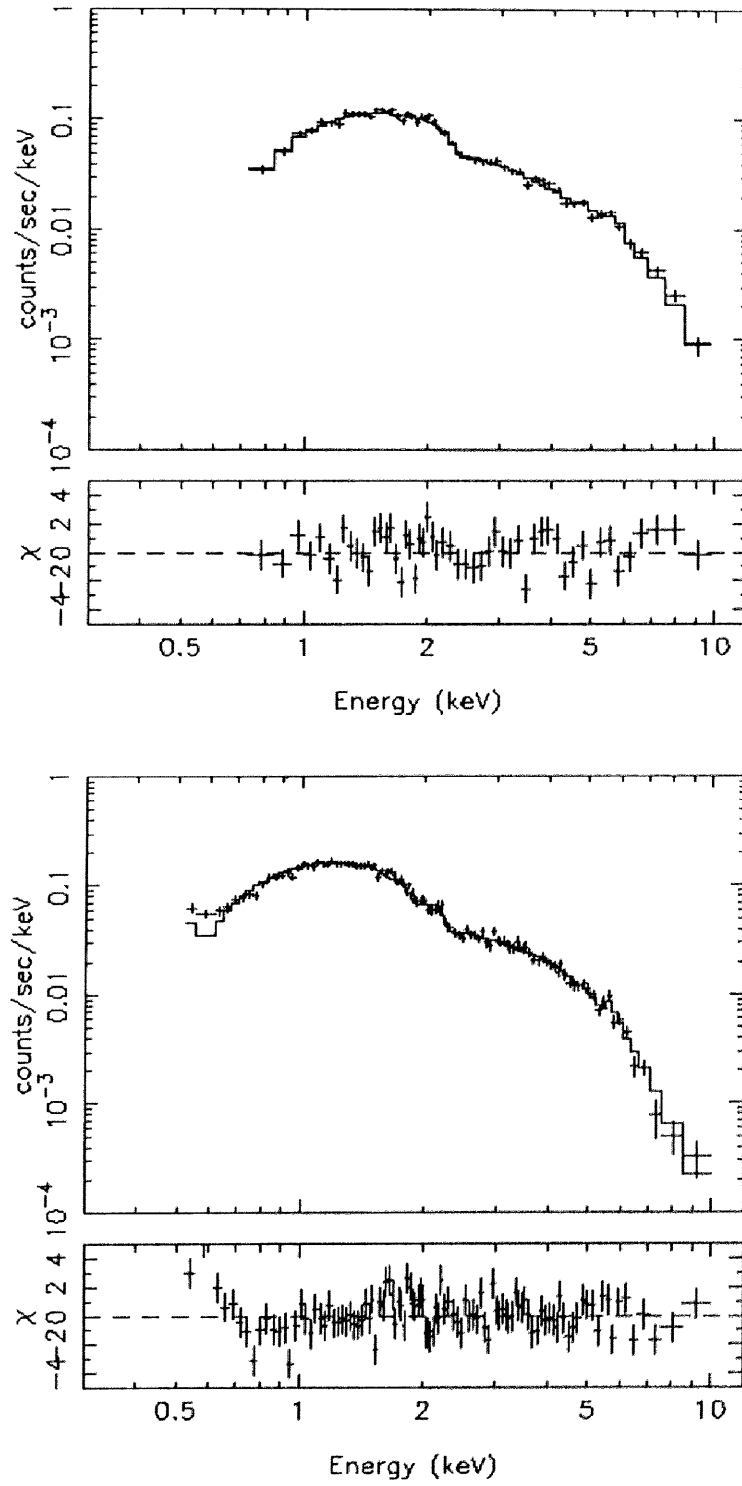


Figure 6.12: A665 X-ray brightness contour superposed by the optical image. The background is not subtracted. Left: GIS, Right: SIS, Top: 0.5-2.5 keV, Bottom: 2.5-10.0 keV

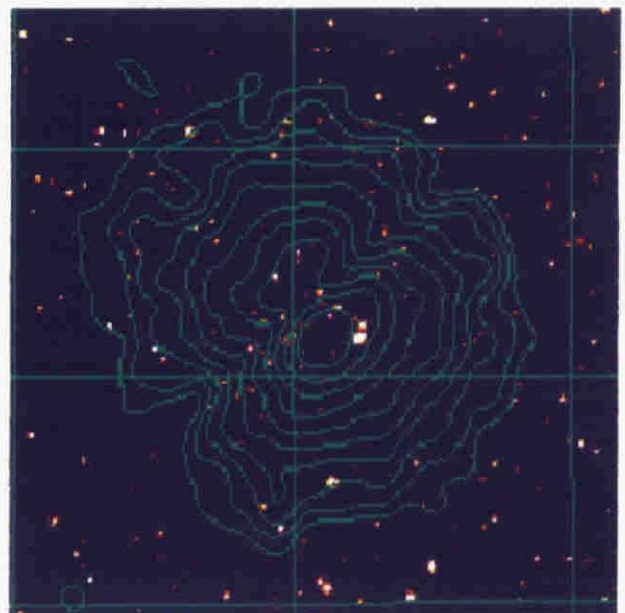
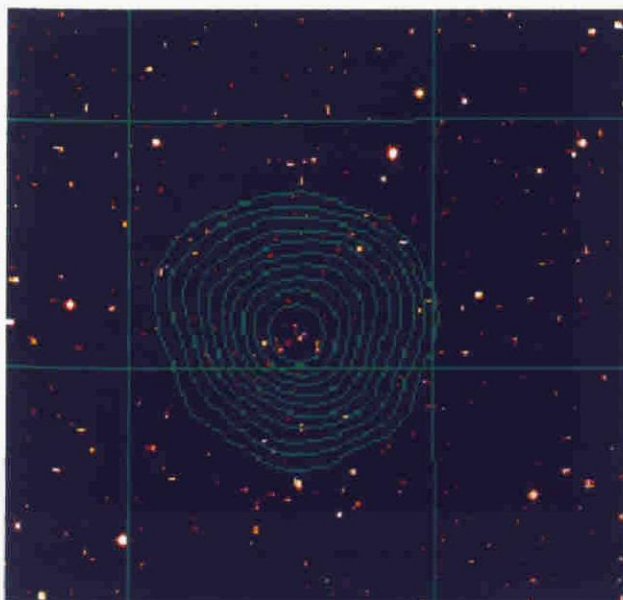
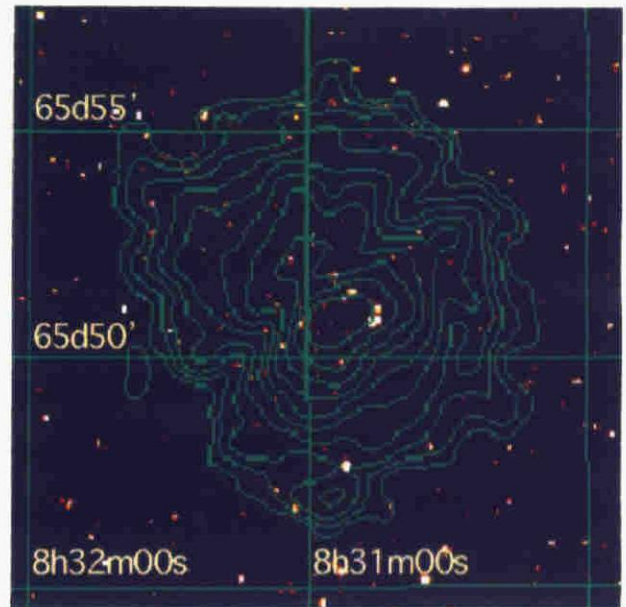
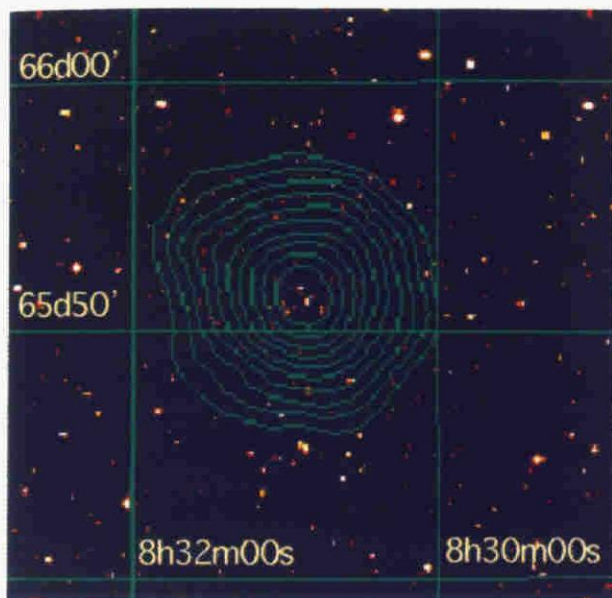


Figure 6.13: A665 Radial profile of surface brightness obtained with SIS0. The best fitting β model profile also shown with solid line. Top:0.5-2.5keV, Bottom:2.5-10keV

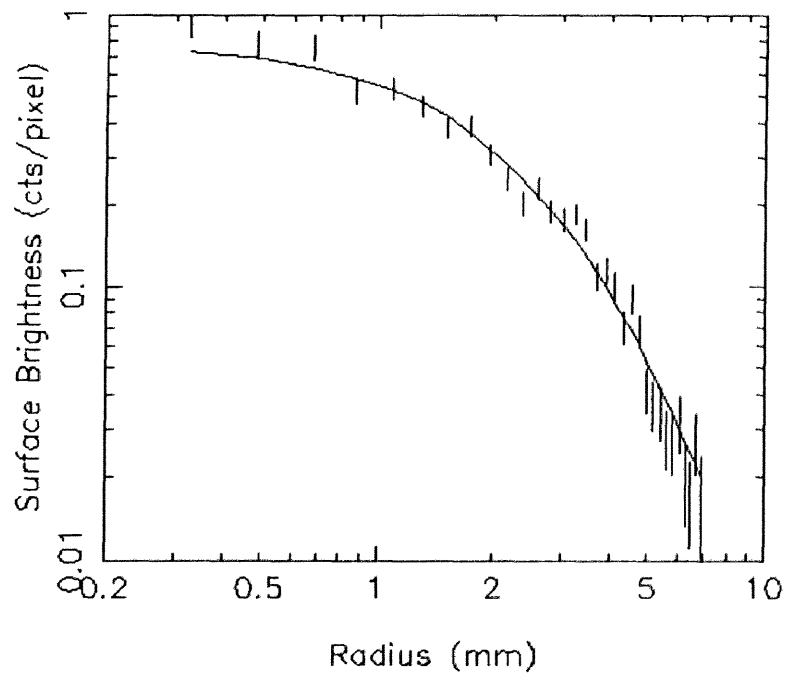
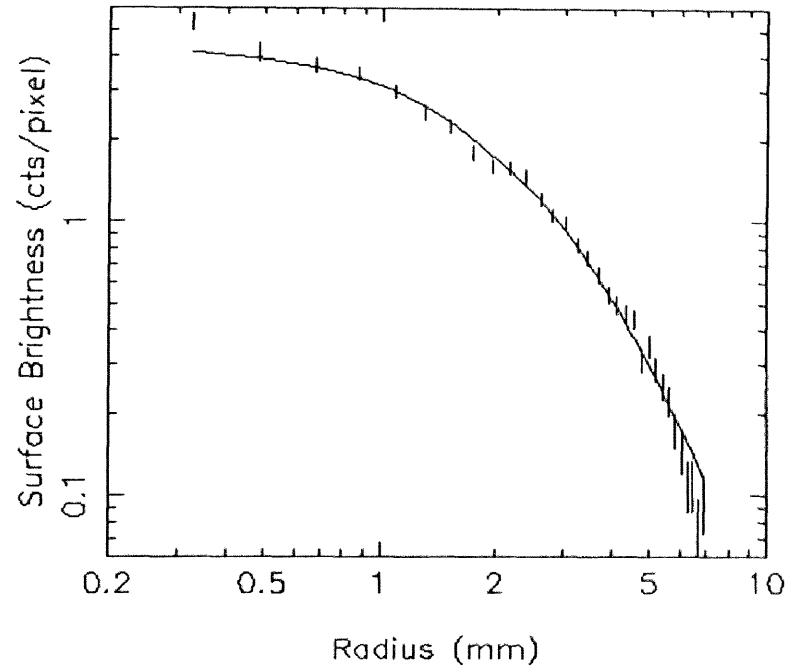
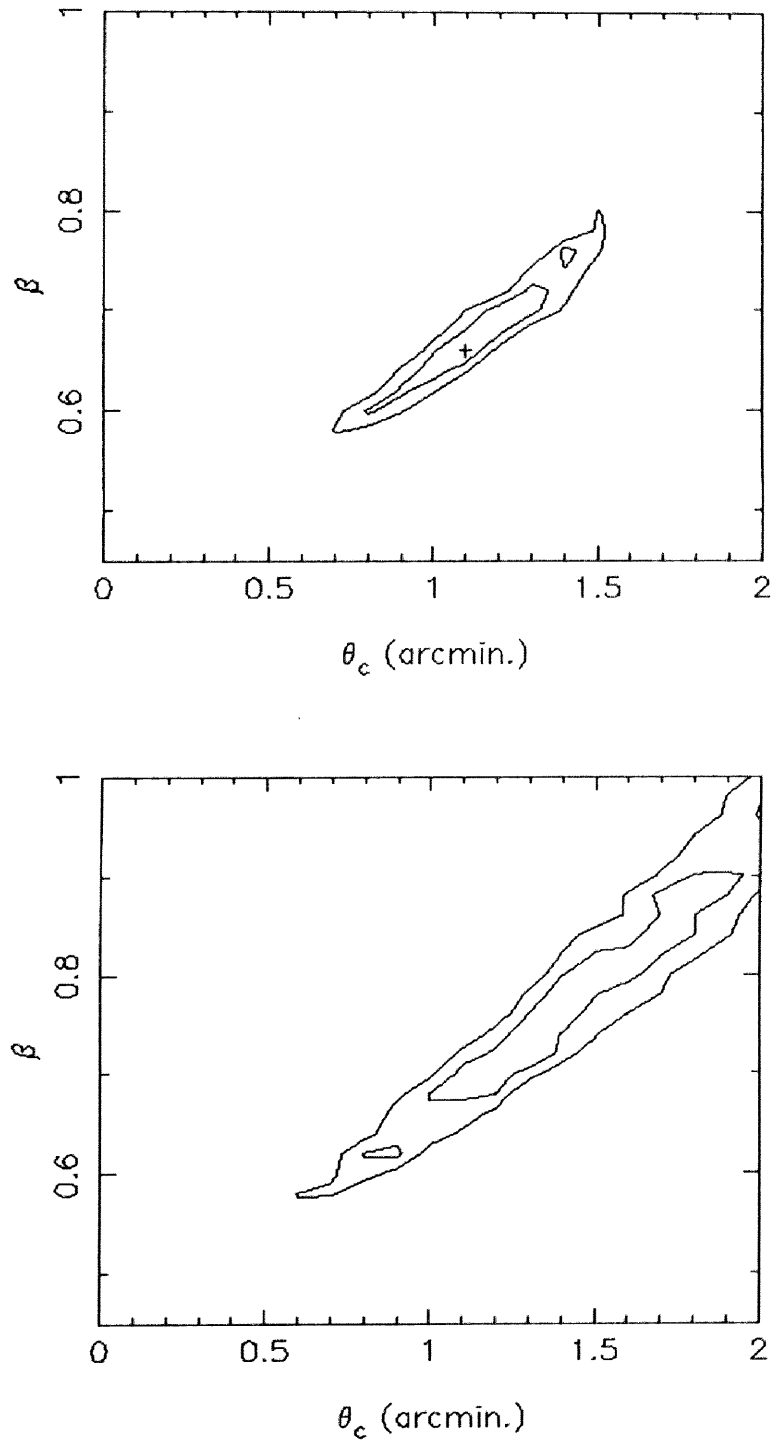


Figure 6.14: Confidence level contours for (θ_c, β) obtained by the β model fitting to the SIS0 radial profile. 90% and 99% confidence level contours and the bestfit values obtained by *ASCA*(cross). Top:0.5-2.5keV, Bottom:2.5-10keV



6.4 A2218

6.4.1 Introduction

A2218 lies at a redshift of 0.171. In the Abell catalogue, this cluster has compact galaxy distribution and classified as Bautz-Morgan type II ([Abell, Corwin & Olowin 1989]) and Rood-Sastry type 'C' ([Struble & Rood 1991]). It has been well studied in the X-ray, optical and radio. A detailed photometric and spectroscopic study of cluster center suggests that there are two galaxy concentrations. There is the cD galaxy at the center of larger concentration, while the smaller one is about 1' apart from the center. From the optical deep observation, it was found that this cluster includes the arcs and arclets, which are considered as image of background ground galaxy distorted by gravitational lensing effect ([Squires et al. 1996]). The location and morphology of the arcs indicate that the bulk gravitational potential is associated with the larger group centered at cD galaxy.

In the radio band, this cluster also shows the strong Sunyaev-Zel'dovich effect observed by various instruments ([Birkinshaw & Gull 1984b], [Birkinshaw, Gull & Hardeback 1984a], [Partridge et al. 1987], [Jones et al. 1993], [Birkinshaw & Hughes 1994]). In the X-ray, *Einstein* and *ROSAT* obtained the smooth and symmetric surface brightness distribution which is centered at the cD galaxy. The obtained parameters are $\theta_c = 1.0$ arcmin. and $\beta = 0.65$. *GINGA* also obtained the temperature of ICM; 6.7 keV ([McHardy et al. 1990]).

6.4.2 Observation

ASCA observed A2218 from April 30 to May 1 in 1993 at the 2CCD nominal position. The angular displacements from the optical axis are 2.43, 6.60, 4.72 and 4.57 for SIS0, SIS1, GIS2 and GIS3, respectively. The observation modes are PH normal mode for GIS and 4CCD Faint/Bright mode for SIS. The effective exposure time was 42000 sec for GIS and 24000 sec for SIS. Details are listed in Table 6.10.

6.4.3 Results

X-ray Spectra

The integrated spectra were fitted to the Raymond-Smith model with photo absorption. At first, the spectrum obtained with each detector was fitted to the model individually. The dispersion of the results obtained above are small and within the statistical error. Then, as the next step, the four spectra obtained with 2 GISs and 2 SISs were fitted to the same model simultaneously. The fitted parameters are $N_H = (4.0 \pm 1.5) \times 10^{20} \text{ cm}^{-2}$, $kT = 6.7 \pm 0.3 \text{ keV}$, Abundance = 0.22 ± 0.05 and 2-10 keV flux = $(8.0 \pm 1.2) \times 10^{-12} \text{ ergs s}^{-1}$

cm^{-2} . The following results were obtained with fixed N_H at the galactic value, since the hydrogen column density is in good agreement with the galactic value of $3.3 \times 10^{20} \text{ cm}^{-2}$ ([Stark et al. 1992]). These results and integration radius dependence of those parameters are listed in Table 6.5. *GINGA* observation also provided the spectral parameters; $kT = 6.7 \pm 0.5 \text{ keV}$, abundance = 0.2 ± 0.2 and 2-10 keV flux = $(6.8 \pm 0.5) \times 10^{-12} \text{ ergs s}^{-1} \text{ cm}^{-2}$. Our results are well consistent with *GINGA* results.

As shown in Table 6.5, the temperature shows the decrease with large integration radius (7.3keV within the radius of 3' and 6.8 keV within the radius of 12'). On the contrary, the iron abundance is almost constant for the all integration radii, though the temperature declines.

X-ray Image

Figure 6.16 show the 0.5-2.5 keV and 2.5-10.0keV band X-ray image of A2218. The brightness distribution is smooth and symmetric. The peak of brightness was determined by searching the position at which the encircled photon counts (the radius of that circle is $0.5\text{mm} \sim 0.5'$) become maximum. The peak positions thus determined for each detector are well consistent. After the background subtraction, we derived the azimuthal averaged surface brightness distribution as shown in figure 6.17. Next, the radial profiles were fitted to the β model within the radius of 8'. Results are shown in figure 6.18. The best fit value in the 0.5-2.5 keV band is $\theta_c = 0.9'$ and $\beta = 0.64$, in the 2.5-10 keV band $\theta_c = 1.1$ and $\beta = 0.70$. Though the profile in the 0.5-2.5 keV band is slightly broader than that in the 2.5-10 keV band, the difference is small in comparison to the statistical error and they are consistent. We applied the two different background subtraction to the profiles to estimate the error of parameters, but there is no dependence on the background subtraction methods.

6.4.4 Discussion

The optical study of galaxy distribution and kinematics suggests that the small group is falling to the main body of this cluster ([Pello et al. 1992]). In this condition, the azimuthal temperature structure seems to be expected ([Schindler & Muller 1993]). Moreover, Markevitch et al. (1996a) and Markevitch (1996b) has reported the existence of radial temperature distribution.

Though the existence of azimuthal temperature structure could not be excluded, the fitted results of radial profile show that it is approximately iso-thermal within the radius of 6' at least, radially. The dependence of the averaged temperature on the integration radius might indicate the existence of the radial temperature drop in the outer skirt of the cluster.

Figure 6.15: A2218 spectra. Top:GIS, Bottom:SIS

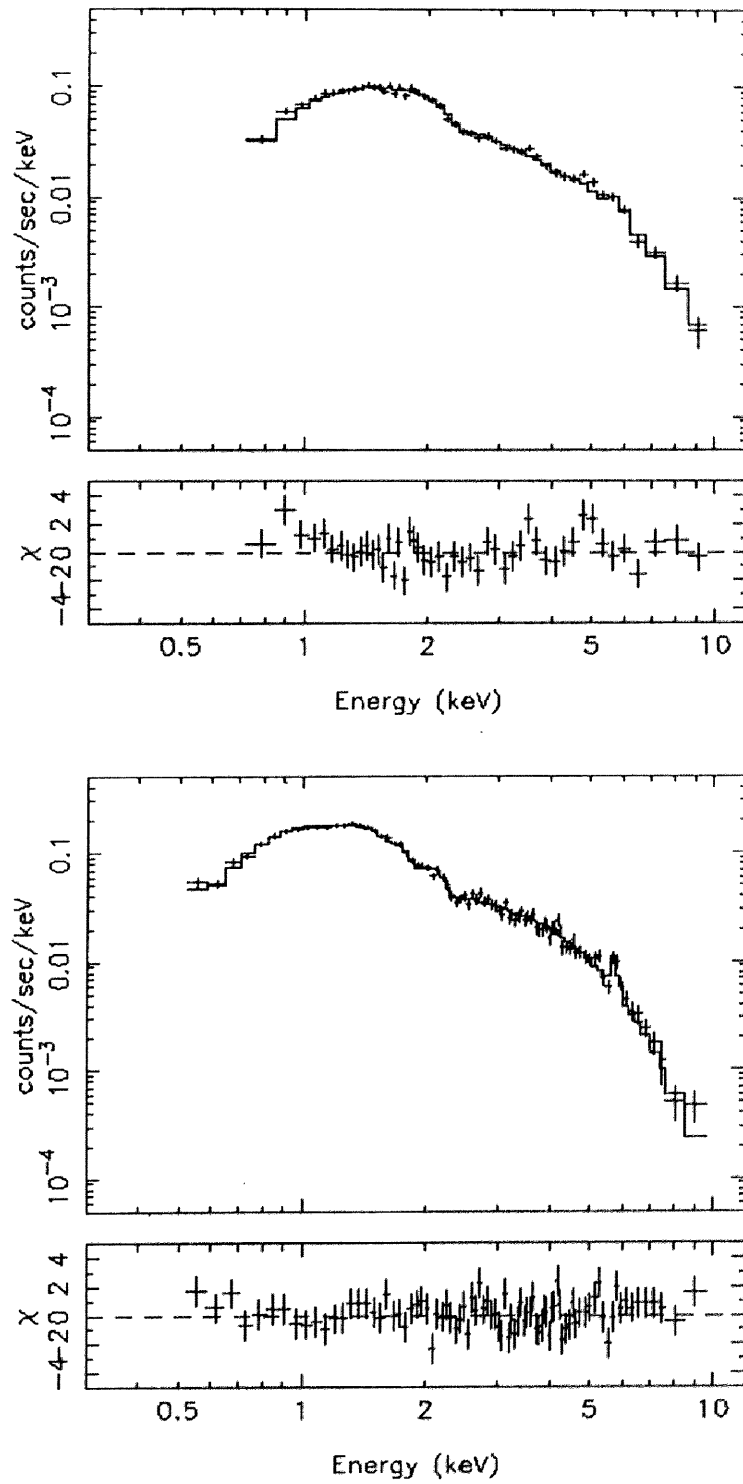


Figure 6.16: A2218 X-ray brightness contour map placed on the optical image. The background is not subtracted. Left: GIS, Right: SIS, Top: 0.5-2.5 keV, Bottom: 2.5-10.0 keV

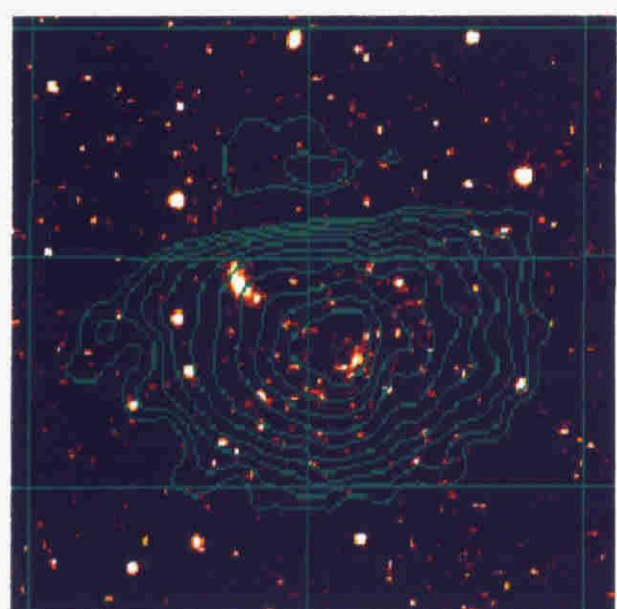
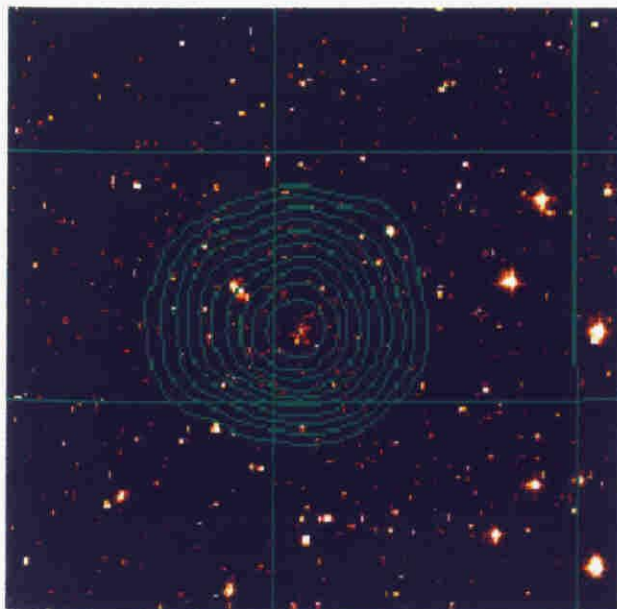
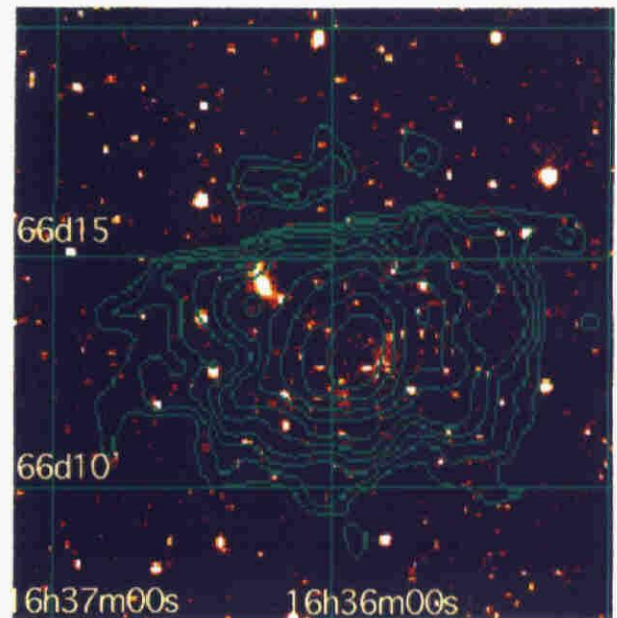
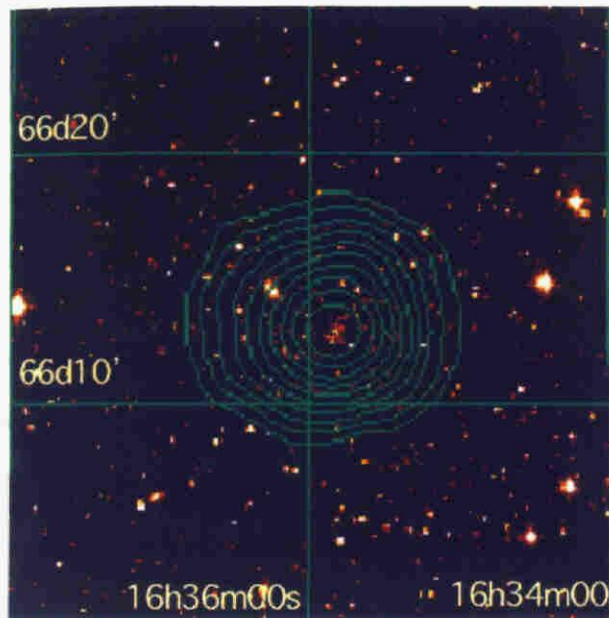


Figure 6.17: A2218 Radial profile of surface brightness obtained with SIS0. The best fitting β model profile also shown with solid line. Top:0.5-2.5keV, Bottom:2.5-10keV

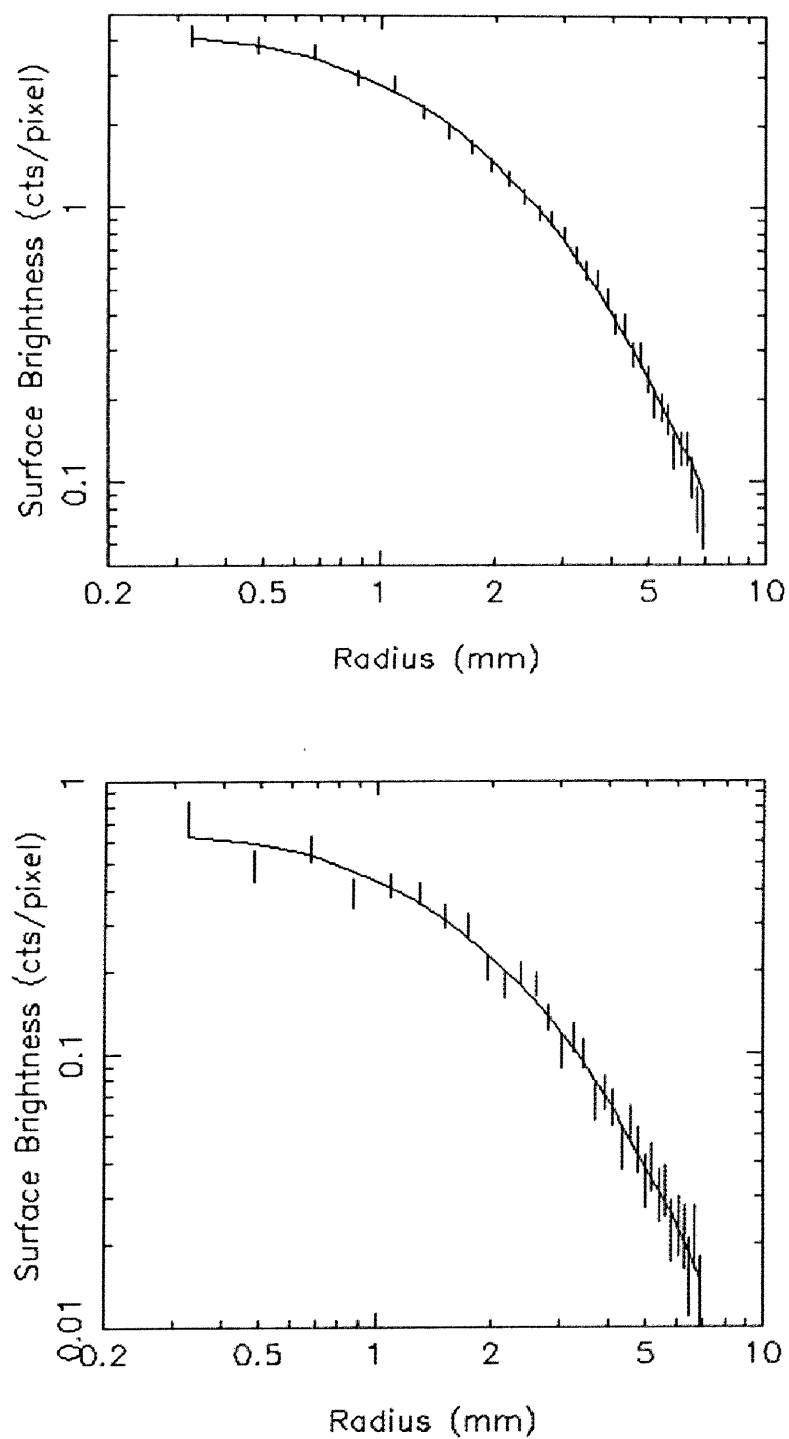
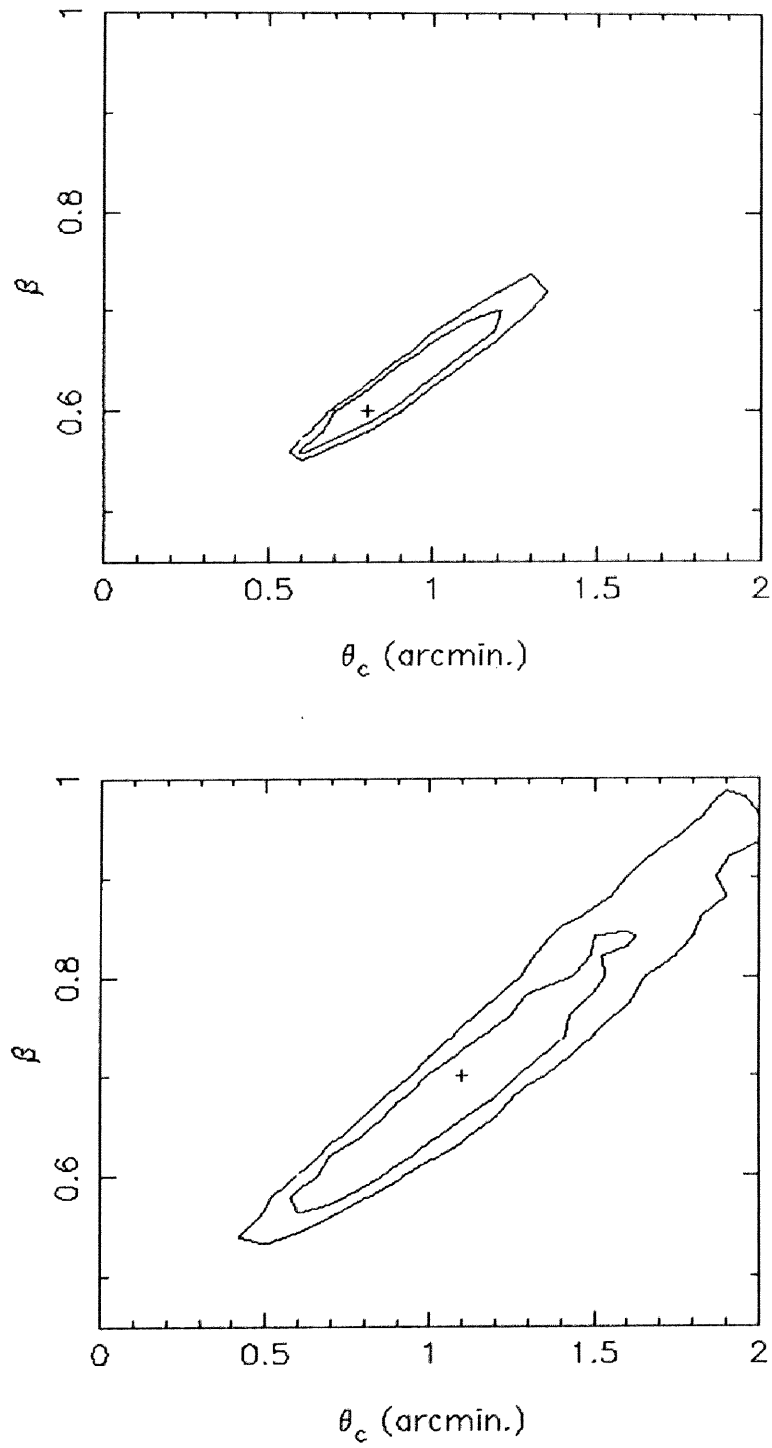


Table 6.5: A2218 spectral fitting result (Integration radius dependence)

Integration region(arcmin.)	kT (keV)	Abundance
$0 < r < 1.5$	$7.3^{+0.6}_{-0.5}$	$0.28^{+0.11}_{-0.10}$
$0 < r < 3.0$	$7.3^{+0.4}_{-0.4}$	$0.20^{+0.06}_{-0.07}$
$0 < r < 6.0$	$6.8^{+0.3}_{-0.3}$	$0.21^{+0.05}_{-0.05}$
$0 < r < 9.0$	$6.7^{+0.3}_{-0.3}$	$0.22^{+0.06}_{-0.05}$
$0 < r < 12.0$	$6.8^{+0.3}_{-0.3}$	$0.22^{+0.05}_{-0.05}$
<hr/>		
2-10keV flux : $(8.11 \pm 1.22) \times 10^{-12}$ ergs s ⁻¹ cm ⁻²		
redshift : 0.18 ± 0.02		
<hr/>		

Figure 6.18: Confidence level contours for (θ_c, β) obtained by the β model fitting to the SIS0 radial profile. 90% and 99% confidence level contours and the bestfit values obtained by *ASCA*(cross). Top:0.5-2.5keV, Bottom:2.5-10keV



6.5 A1204

6.5.1 Introduction

A1204 is the distant Abell cluster classified as richness class I and Bautz-Morgan type II-III. This cluster had not been studied before detection in the *ROSAT* All Sky Survey (RASS). In this cluster, a dominant central galaxy has been found at the X-ray bright core by an optical follow-up study of RASS clusters with Faint Object Spectrograph on the Isaac Newton Telescope ([Allen et al. 1992]) and the redshift was obtained by this followup observation. For this cluster, the optical line emission (H_{α} + [NII] complex) has been detected. Most of clusters containing a central dominant galaxy in the center of X-ray image shows this phenomenon.

6.5.2 Observation

ASCA observed A1204 from May 21 to 22, 1994. The source center was settled at the 1CCD nominal position and observed by GIS PH normal mode and SIS 1CCD Faint mode. According to the standard method previously noted, the data were selected. The resultant exposure is about 35000 sec for GIS and 36000 sec for SIS. The counting rate were 0.13 cts s⁻¹ for GIS, 0.21 cts s⁻¹ for SIS. The details are listed in Table 6.10.

6.5.3 Results

This cluster has extremely compact brightness distribution in comparison to other cluster. Then the only spectrum integrated within the radius of 6' was extracted. The X-ray image of this cluster shows the structure likes 4 leaves. This is very similar to a point source image (see figure 6.20 and point source image 4.14). This implies that the target shows strong peak and the image extension is very small or weak. From the X-ray spectra, iron *K α* emission lines have been detected and line center energy is in good agreement with the center energy deduced from thermal plasma emission in collisional equilibrium (assuming the redshift is 0.170). Furthermore, the X-ray spectra is well described by the Raymond-Smith model with single temperature (Table 6.6, the obtained temperature is exceptionally lower than other distant clusters). Then though the image is less extended, the detected emission are the thermal emission from the cluster. However, since the image is extremely compact, the θ_c and β could not be obtained by *beta* model fitting (the best fit values were obtained, but the lower limit of θ_c has been not obtained. figure 6.21). In order to investigate the extension of the image, the image was divided into 2 energy band; 0.5-2.5keV and 2.5-10keV and the radial dependence of hardness ratio was plotted (figure 6.22).

6.5.4 Discussion

The figure 6.22 may indicate the existence of excess of soft X-ray within the radius of 1 arcmin. At a redshift of 0.17, 1 arcmin. corresponds to ~ 240 kpc. Since the *ASCA* XRT has moderate spatial resolution, the spatial structure has been distorted. However, the sharp structure has remained. Then the size of 240 kpc is upper limit of the size of this structure. As mentioned before, from this cluster, the optical line emission has been detected. The optical line emission like this are commonly detected in the cluster with (X-ray) cool component and central dominant galaxy in the central region ([Fabian 1994]). Allen et al. (1992) suggested the existence of the cooling flow in the central region. Using the luminosity and the best fit values of θ_c and β , the derived cooling time scale is only a few times of 10^9 yr, which is much shorter than the Hubble time. Against the cooling flow, Ikebe (1996) found the coexistence of hot and cool gas in the central region from *ASCA* observation of Fornax and Centaurs clusters, and suggests that the origin of the cool component is central dominant galaxy and the central excess of emission come from the central dominant galaxy. In the case of A1204, it is hard to consider that the origin of this central excess emission is the central dominant galaxy, because for such distant cluster, the emission from ICM are dominant rather than the galaxy component.

Table 6.6: Spectral fit results

Parameter	
$N_H(10^{20} \text{ cm}^{-2})$	7.4 ± 1.0
kT (keV)	3.6 ± 0.1
Abundance	0.35 ± 0.06
<hr/>	
2-10 keV flux : $(3.85 \pm 0.58) \times 10^{-12} \text{ ergs s}^{-1} \text{ cm}^{-2}$	
redshift : 0.17 ± 0.010	
<hr/>	

Figure 6.19: A1204 Spectrum Top: GIS, Bottom: SIS

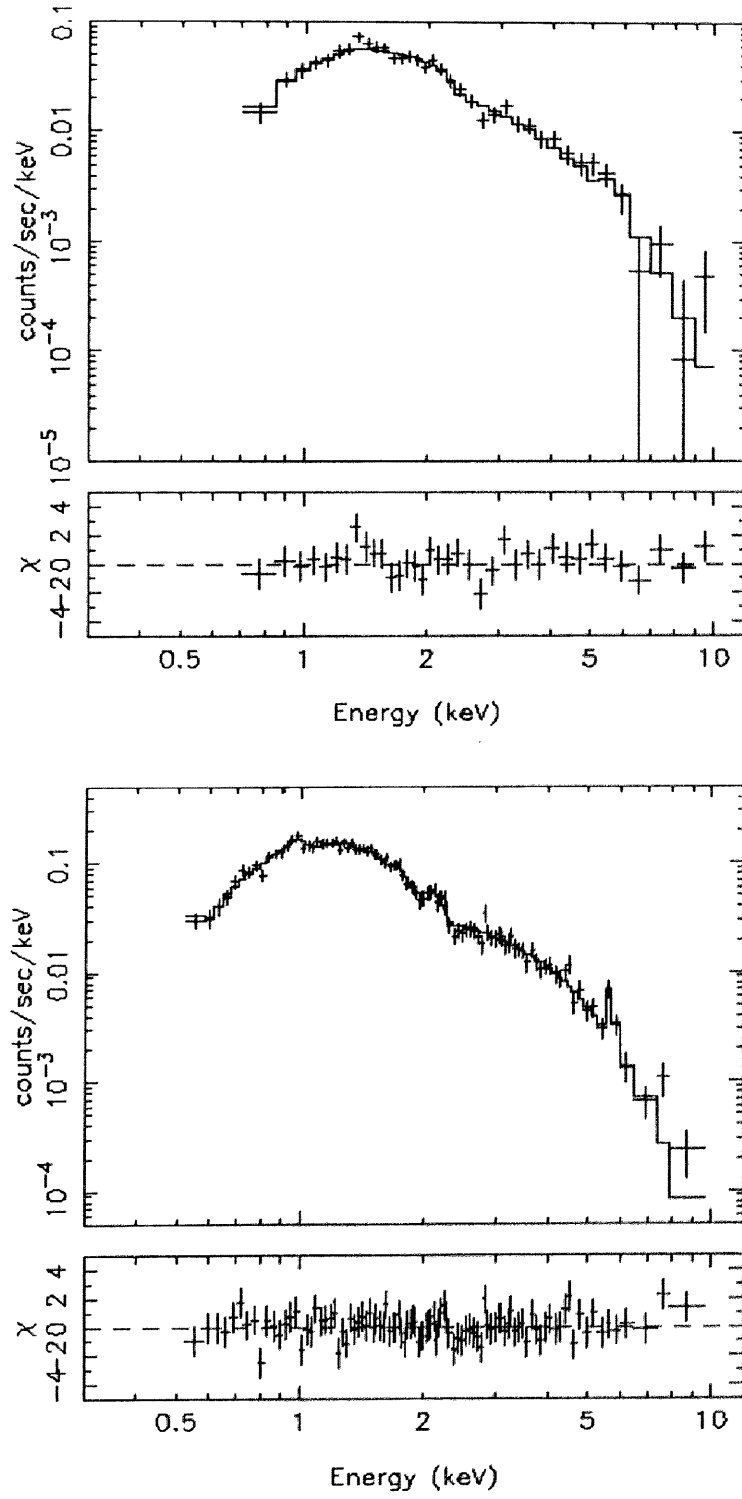


Figure 6.20: A1204 X-ray brightness contour superposed by the optical image. The background is not subtracted. Left: GIS, Right: SIS, Top:0.5-2.5 keV, Bottom:2.5-10.0 keV

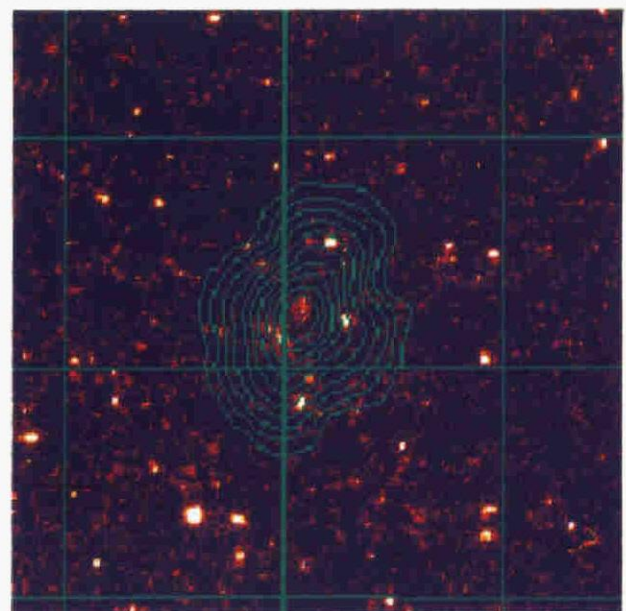
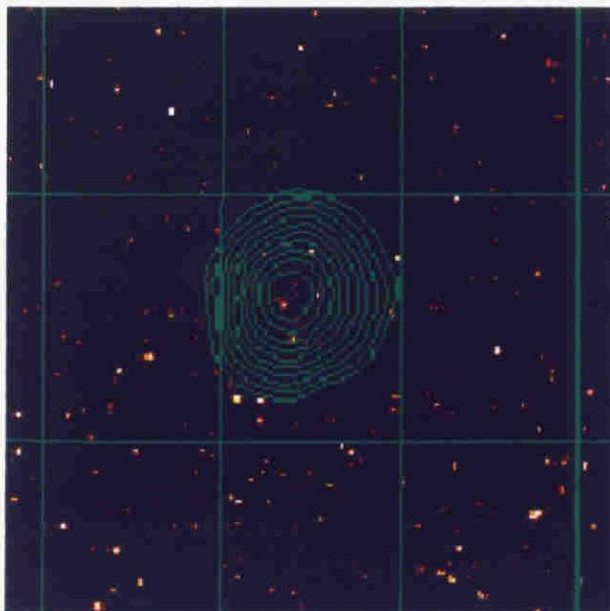
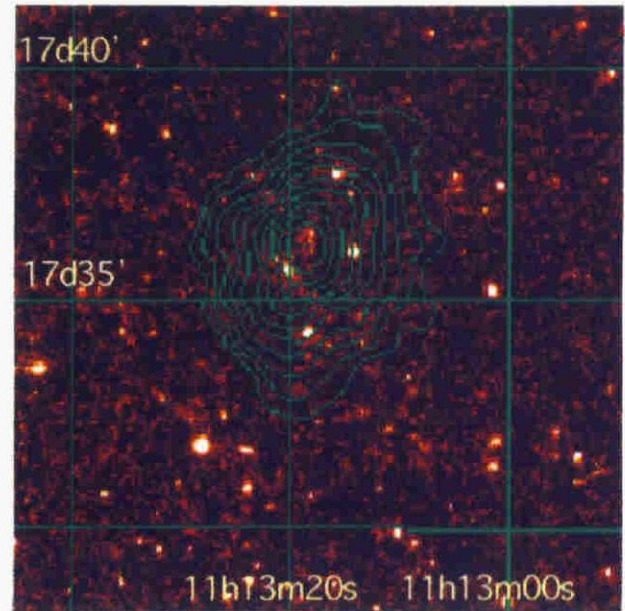
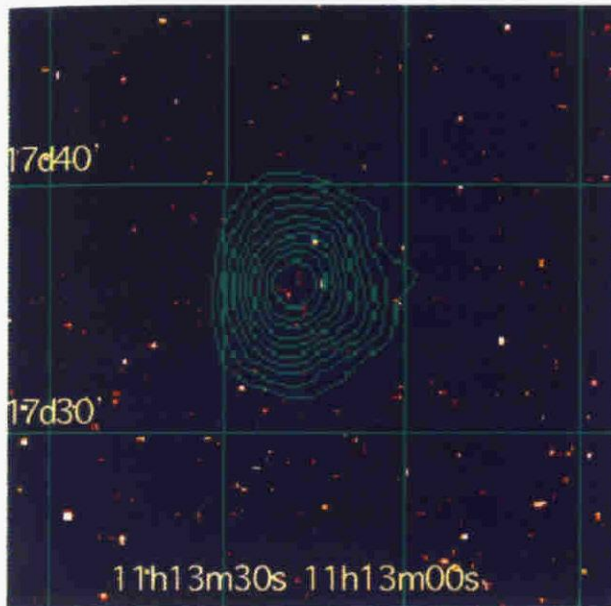


Figure 6.21: Confidence level contours for (θ_c, β) obtained by the β model fitting

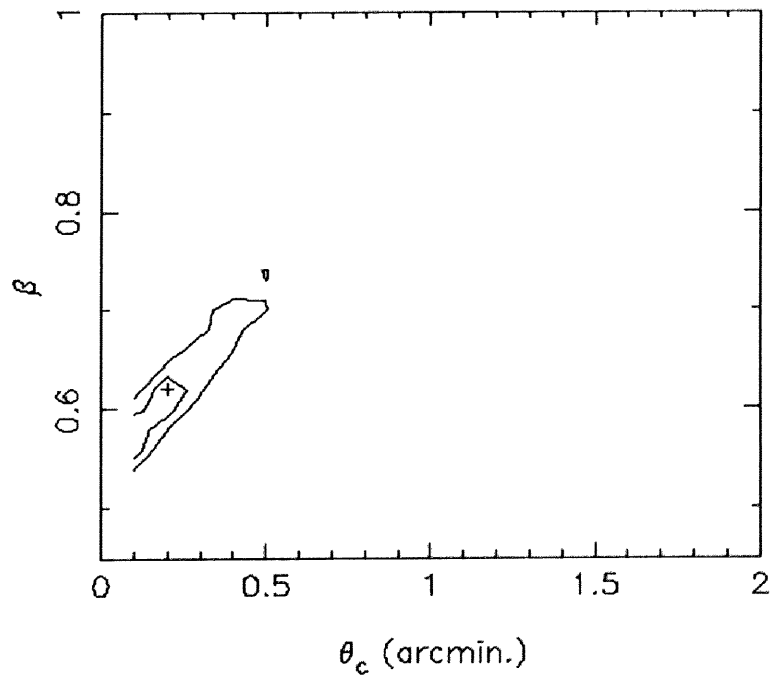
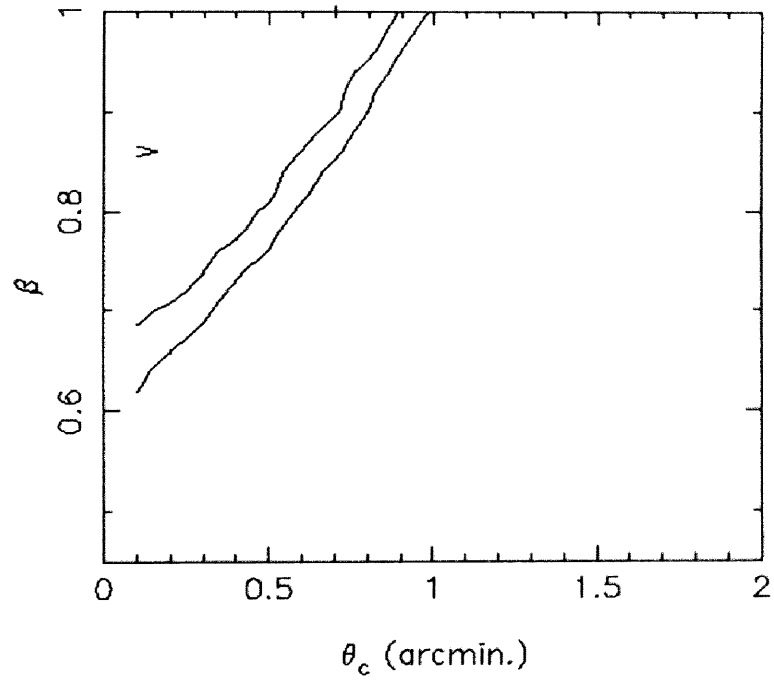
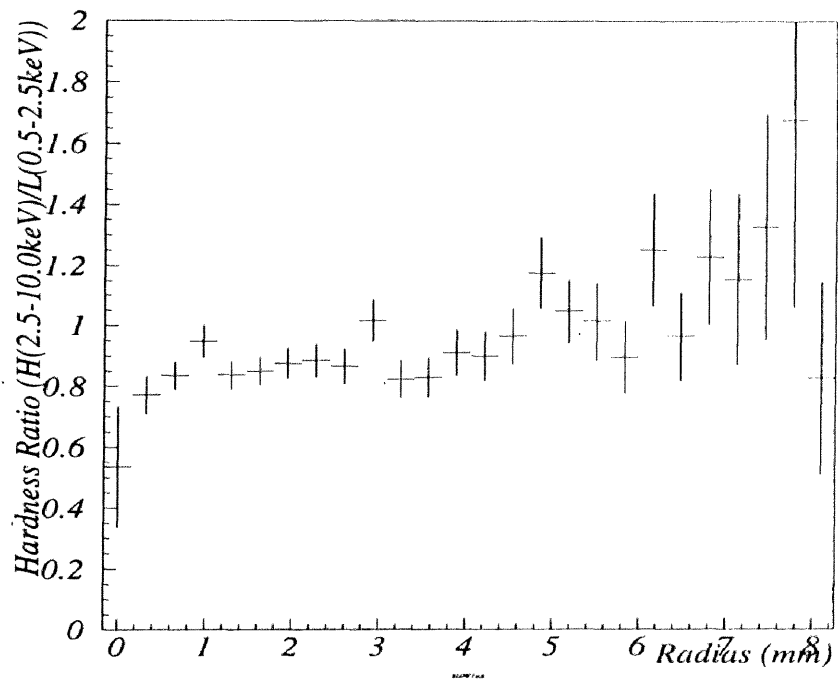


Figure 6.22: Radial dependence of hardness ratio



6.6 A1413

6.6.1 Introduction

A1413 is at the redshift of 0.1427 and classified as Abell richness class 3, Bautz-Morgan type I and Rood-Stastry type cD. This cluster is neither well known in X-rays nor at optical wavelengths.

GINGA observed this cluster and obtained the temperature of 8.85 ± 0.50 keV and the 2-10 keV flux of 2.1×10^{-11} ergs s $^{-1}$ cm $^{-2}$ (it corresponds to the 2-10 keV luminosity of 2.1×10^{45} ergs s $^{-1}$) ([David *et al.* 1993]). *ROSAT* also observed this cluster. The X-ray brightness distribution shows the elongation significantly as seen in galaxy distribution ([Allen *et al.* 1995]). However, since it has fairly smooth looking and there is no strong substructure as seen in elongated clusters frequently ([Slezak, Durret & Gerbal 1994]) at the scale larger than 30 arcsec.

Allen *et al.* (1995) obtained the radial distribution of the density and temperature by the deprojection technique from *ROSAT* PSPC image. The central temperature they obtained is ~ 6.5 keV and increasing to the 8.8 keV with the radius. They estimated the cooling time, which is much less than the Hubble time (2×10^{10} yr) within the radius of 0.2 Mpc. Then they suggested the existence of the cooling flow in the central region within the radius of 0.2 Mpc (corresponds to $1'$). The integrated mass deposition rate (\dot{M}) was derived to be $200 M_{\odot}$ yr $^{-1}$.

6.6.2 Observation

ASCA was pointing to the A1413 from December 11 to 12 in 1993. The cluster center was placed at 2CCD nominal position. The instruments were in the PH normal mode for GIS and 4CCD Faint mode for SIS. The distance between the cluster center and optical axis is $1.97'$, $5.44'$, $3.54'$ and $3.64'$ for SIS0, SIS1, GIS2 and GIS3, respectively. The effective exposure time after the data selection are 39000 sec for GIS and 35000 sec for SIS. The counting rates are 0.42 cts/sec within the radius of $9'$ for GIS and 0.52 cts/sec within the radius of $6'$ for SIS, and this cluster is the brightest cluster among the clusters used in this thesis¹.

6.6.3 Results

X-ray Spectra

As the model spectrum, the Raymond-Smith model with photo absorption has been used. The parameters obtained with each detector show dispersion in the temperature range of

¹In section 6.7, the results of A1689 has been shown briefly. It is brighter than A1413 actually.

7.0-8.5 keV and the temperature obtained with SISs is about 0.5 keV smaller than that obtained with GISs. As the next step, the simultaneous spectral fitting for the spectra obtained each detector has been done. The results are $N_H = (3.8 \pm 0.8) \times 10^{20} \text{ cm}^{-2}$, $kT = 8.0 \pm 0.3 \text{ keV}$, abundance = 0.23 ± 0.04 and 2-10 keV X-ray flux = $(1.8 \pm 0.3) \times 10^{-11} \text{ ergs s}^{-1} \text{ cm}^{-2}$. The galactic value of N_H is $2.2 \times 10^{20} \text{ cm}^{-2}$ and it is smaller than our result. When a column density is fixed at the galactic value, only the temperature is changed to 7.6 keV and other parameters are not changed. The results and dependence of parameters on the integration radius are listed in Table 6.7, in which parameters was obtained with fixed N_H at the galactic value and the quoted errors are statistical error with 90% confidence. The parameters are almost constant for all integration radius.

For this cluster, iron K_α lines are clearly seen and K_β lines are also detected. We analyzed the line intensities in detail as shown in the section 6.7.

X-ray Image

Figure 6.24 show the 0.5-2.5 keV and 2.5-10.0keV band X-ray image of A1413. The brightness distribution looks smooth. While the *ROSAT* image shows the north-south elongation, the elongation is not seen strongly in *ASCA* image. It seems to be due to the PSF broadening and vignetting.

Figure 6.25 were the azimuthal averaged surface brightness distribution of SIS0 image in the 0.5-2.5 keV and 2.5-10.0 keV band after background subtraction, based on the background map from the superposed blank field accumulated in much longer exposures for the X-ray background observations. The cluster center was found by searching the position at which the flux within the circle of 0.5mm is maximum. These radial profiles were fitted to the β model within the 10 arcmin and the core radius and β were obtained; $\theta_c = 0.6'$, $\beta = 0.58$ in the 0.5-2.5 keV, $\theta_c = 0.7'$, $\beta = 0.64$ in the 2.5-10.0 keV (figure 6.26)

The dependence of parameters on the background brightness were estimated by subtracting the various background brightness; the superposed blank sky and several source free regions in the field of view. The dispersion of best fit values are within the statistical error shown in figure 6.26.

6.6.4 Discussion

While the existence of strong cooling flow in this cluster has been suggested by Allen et al. (1995) from *ROSAT* PSPC image, the X-ray spectrum obtained by *ASCA* is well fitted to the single temperature Raymond-Smith model in all integration radius. Then the X-ray spectrum were made from the simulation assuming the temperature and density distribution derived by Allen et al. with *ASCA* XRT PSF, and fitted to the single temperature

Raymond-Smith model. The resulting temperature is 7.2 keV within the radius of 1.5'. Our result is slightly high. However, the temperature obtained with SISs only is smaller than that obtained by simultaneous fitting and that obtained with GISs only. Then at the present, the existence of the cool component in the central region couldn't be excluded.

Though A1413 is the nearest one among the clusters presented in this thesis, this cluster has the smallest core radius among them. If the brightness distribution consists of the strong cusp-like peak at the center of broad (and low brightness) outer skirt which is represented by β model, the radial profile blurred by XRT PSF has much smaller core radius than the intrinsic one. Then it seems to be consistent with *ROSAT* image.

Table 6.7: Fitting result (Integration radius dependence)

Integration radius(arcmin.)	kT (keV)	Abundance
1.5	$8.1^{+0.5}_{-0.5}$	$0.32^{+0.08}_{-0.07}$
3.0	$8.2^{+0.4}_{-0.3}$	$0.27^{+0.05}_{-0.05}$
6.0	$8.0^{+0.3}_{-0.3}$	$0.24^{+0.04}_{-0.04}$
9.0	$8.0^{+0.3}_{-0.3}$	$0.23^{+0.04}_{-0.04}$
12.0	$8.0^{+0.3}_{-0.3}$	$0.28^{+0.06}_{-0.06}$
<hr/>		
2-10keV flux : $(1.77 \pm 0.27) \times 10^{-11}$ ergs s ⁻¹ cm ⁻²		
redshift : 0.15 ± 0.010		
<hr/>		

Figure 6.23: A1413 spectra. Top:GIS, Bottom:SIS

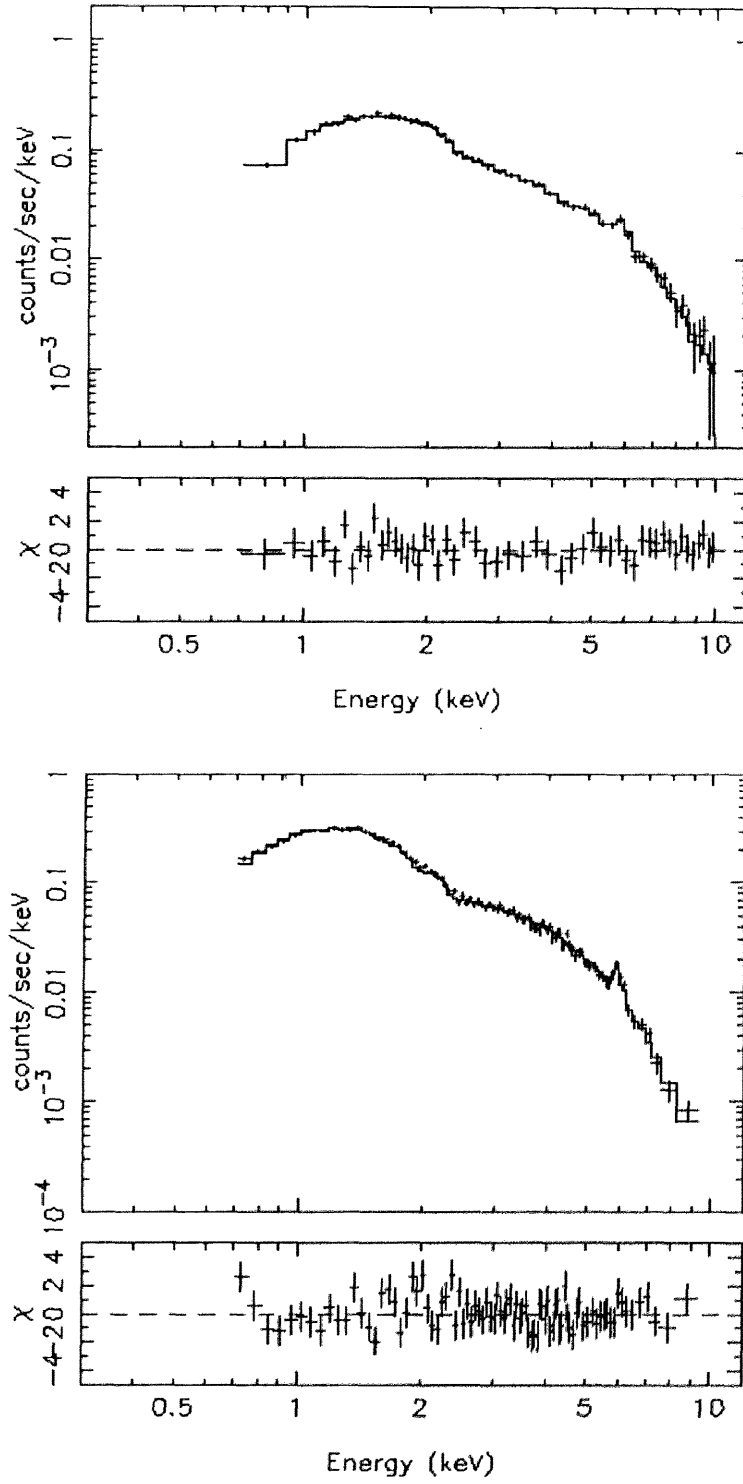


Figure 6.24: A1413 X-ray image. The background is not subtracted. Top:GIS, Bottom:SIS

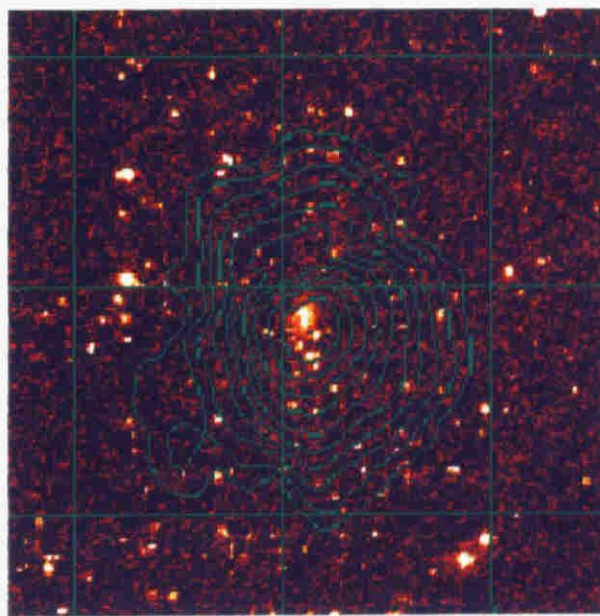
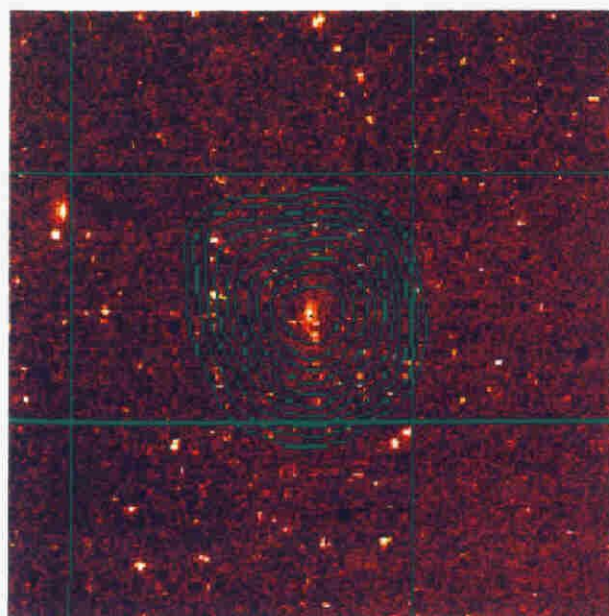
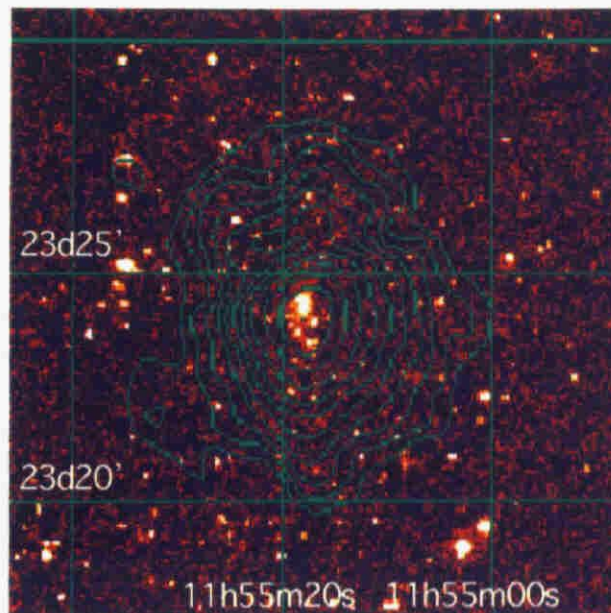
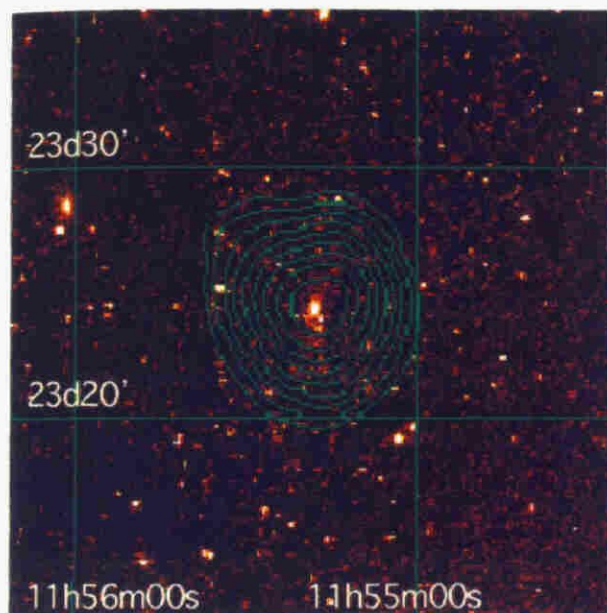


Figure 6.25: A1413 Radial profile of surface brightness obtained with SIS0. The best fitting β model profile also shown with solid line. Top:0.5-2.5keV, Bottom:2.5-10keV

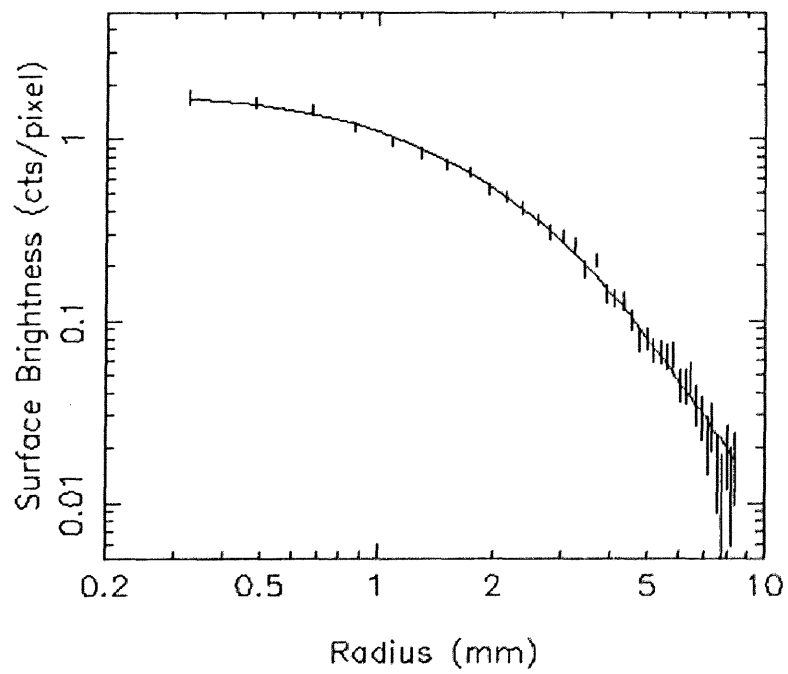
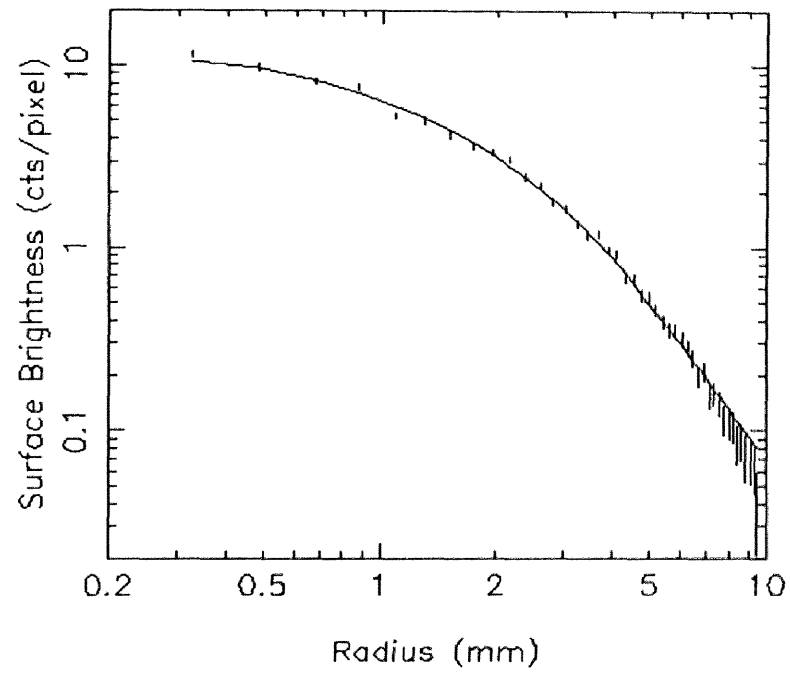
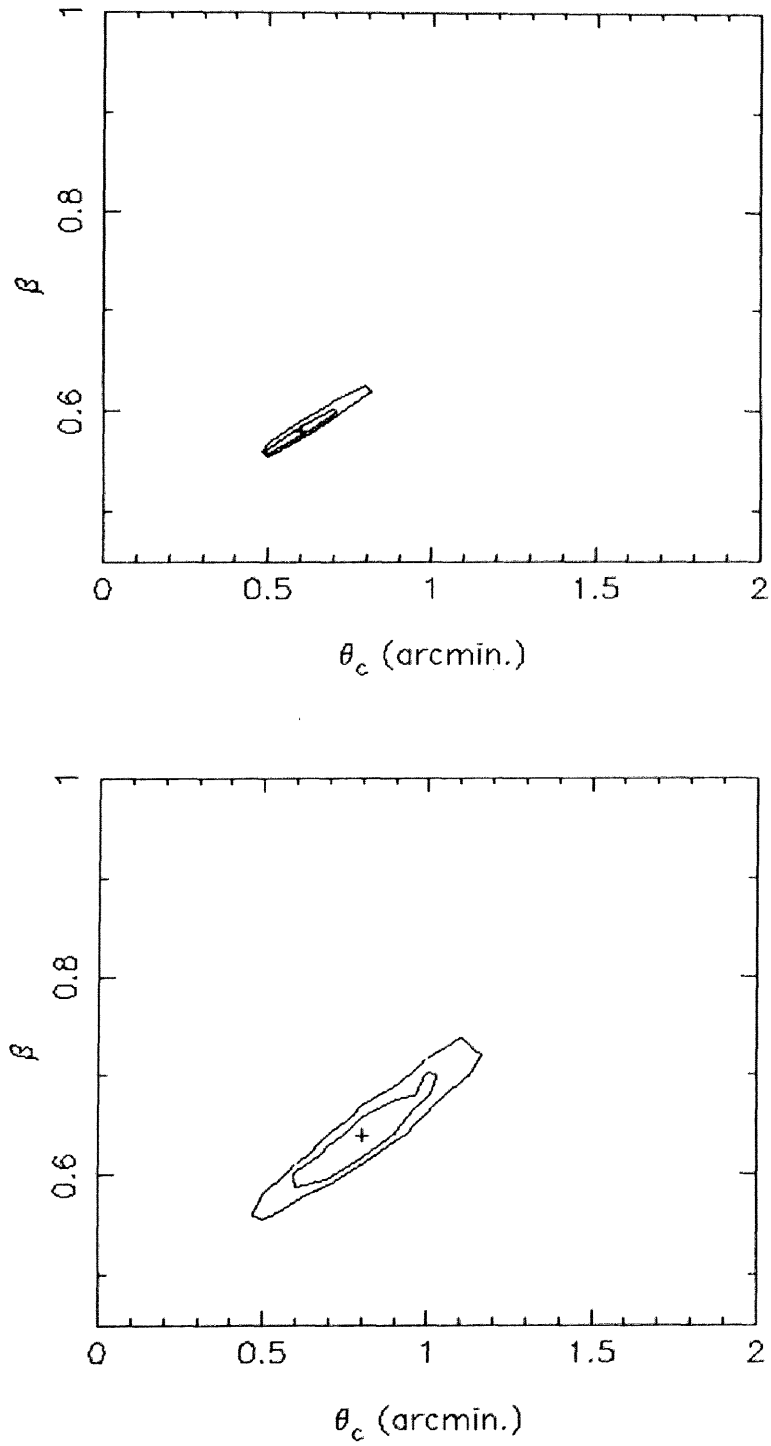


Figure 6.26: Confidence level contours for (θ_c, β) obtained by the β model fitting to the SIS0 radial profile. 90% and 99% confidence level contours and the bestfit values obtained by *ASCA*(cross). Top:0.5-2.5keV, Bottom:2.5-10keV



6.7 Fe-K line analysis – $K\alpha/K\beta$ ratio anomaly ?

6.7.1 Introduction

In the case of high temperature cluster gas, higher than 5keV, the abundance is mainly determined by the sum of H-like and He-like Fe- $K\alpha$ line intensities. Other lines, such as $K\beta$, are not sensitive for the abundance determination. For nearby clusters of galaxies, Virgo, Perseus clusters, it is reported that the intensity ratio of Fe- $K\alpha$ to Fe- $K\beta$ is smaller than model prediction assuming the collisional ionization equilibrium.

The resonance scattering effect on the Fe- $K\alpha$ lines may explain such a small ratio. Since the optical depth for Fe- $K\alpha$ line with respect to the resonance scattering is larger than that for Fe- $K\beta$ line, Fe- $K\alpha$ is suppressed at the dense core of clusters much more than Fe- $K\beta$. Hence the intensity ratio of Fe- $K\alpha$ to Fe- $K\beta$ become small in the central region. However, considering the conservation of photon number of line emission, this effect should not be seen in the spectrum spatially integrated over the cluster emission. For nearby clusters, Fe- $K\beta$ lines are seen at 8keV. The XRT effective area rapidly decreases in this energy band. Then the uncertainty of $K\beta$ line intensity is considerably large due to the uncertainty of continuum emission and poor statistics.

For distant clusters of galaxies, the photon statistics are poor in comparison to the nearby clusters of galaxies. However there are some advantages as follows.

- The Fe lines are redshifted at the energy band, 5 to 7 keV, where we can get good quantum efficiency and intrinsic background spectrum has no strong structure. The flux fluctuation of background spectra is negligible, because the flux from the source is much larger than that of the background spectra in the energy range of 5 to 7 keV.
- The image size of the distant clusters is smaller than F.O.V.
- It is easy to obtain the averaged values of temperature, abundance and luminosity accurately.

6.7.2 Analysis & Results

Averaged temperature, abundance and luminosity

We have analyzed 16 distant clusters of galaxies in the redshift range from 0.1 to 0.54. Among them, we selected A665 and A1413 because they show clear Fe- $K\beta$ line features. For comparison, we also selected A1689 with no strong Fe $K\beta$ feature. At first, the values of luminosity, temperature and Fe abundance averaged in the whole region of the

clusters were obtained using the Raymond-Smith model. These three clusters have similar temperature (~ 8 keV) and abundance (~ 0.25).

In different to the results shown in section 6.6, the parameters were not obtained by simultaneous fitting the spectra of GISs and SISs, but were obtained by fitting separately.

Line intensities – He-like and H-like $K\alpha$ lines(SIS)

As the next step, to separate the lines from the continuum, we used the models consisted of bremsstrahlung and 2 Gaussians for GIS and SIS. The Gaussians represent the Fe- $K\alpha$ and $K\beta$ for GIS, and He-like and H-like of $K\alpha$ lines for SIS. For SIS, the poor photon statistics prevent us to evaluate the $K\beta$ lines. Then we intend to analyze the He-like and H-like $K\alpha$ lines with SIS. The best fit values for SIS are listed in Table 6.8.

The line center energies agree with the energies expected from the redshift. In the collisional ionization equilibrium, the ratio of He-like to H-like $K\alpha$ line intensity, which implies the ionization temperature, is the function of the plasma temperature. The ionization temperature derived from the intensity ratio using the Masai code is also listed in Table 6.8 (Ionization Temperature). The ionization temperature of these clusters of galaxies is slightly large. The GIS spectra show slightly higher continuum temperatures (This discrepancy may due to the systematic error of detector and/or telescope response.). Then the ionization temperature is agrees with the electron temperature derived from the continuum emission.

Line intensities – $K\alpha$ and $K\beta$ lines(GIS)

GIS has the better efficiency in the high energy range($6 > \text{keV}$), then $K\beta$ intensity could be evaluate with high confidence. The fitting results for GIS are listed in Table 6.9.

Intensity ratio of $K\alpha$ to $K\beta$ is also the function of the plasma temperature kT . The ratio derived from the electron temperature using Msai model is also listed. Within 4 arcmin., the intensity ratio of $K\alpha$ to $K\beta$ is consistent with the model prediction for these all clusters of galaxies. However, the intensity of $K\beta$ becomes strong as the radius is increasing in comparison to the $K\alpha$ intensity for A665 and A1413. For A1689, the intensity of $K\beta$ is not clearly detected even in the spectrum integrated in the large integration region.

Especially, for A665, $K\beta$ line intensity is 2.5 times larger than the predicted value deduced from the intensity of $K\alpha$ line. According to the $K\alpha$ line intensity, the abundance is 0.3 Solar value for the spectra integrated in each radius, not dependent on the radius. But using the intensity of $K\beta$, the abundance is 0.4 Solar within 4arcmin. radius, 0.75 solar within 8arcmin. radius.

6.7.3 Discussion

Assuming the iso-thermal and optically thin plasma with collisional ionisation equilibrium(CIE), it is impossible to describe the obtained intensity ratio.

For A665, Markevitch et al.(1996) has reported the strong temperature drop in the outer region. In our results, the dependence of the best fit temperature on the integration radius indicates the existence of the temperature gradient. This leads the radial dependency of the line intensity. As mentioned above, the resonance scattering effect also changes the brightness profile of Fe-K α line.

In order to estimate the deviation from the iso-thermal and optically thin ICM, we simulated the projected spectra for two conditions. One is the iso-thermal ICM of $kT = 8.3\text{keV}$ with resonance scattering. Another condition is that the ICM temperature in the outer region is lower than the central temperature; $kT = 9\text{keV}$ ($r < 5R_c$), $kT = 4\text{keV}$ ($r \geq 5R_c$)(figure 6.30). In both cases, the intensity ratio increases with the integration radius. We can neglect the resonance scattering effect with larger integration radius($r > 3R_c$), assuming the conservation of the number of photons. The temperature gradient makes discrepancy between the observed electron temperature and the temperature derived from the line ratio. Assuming the collisional ionization equilibrium, in the outer portion, the emissivity of K α line becomes strong relative to that of K β line. Then the existence of temperature gradient makes the ratio of K α to K β large.

Based on the assumption of collisional ionisation equilibrium, this small ratio and radial dependence can not be described. If ICM in the outer region is not in the CTE but recombining plasma, this small ratio may be possible. However, the quantitative simulation and analysis have never been attempted, because the collisional ionisation equilibrium timescale for the ICM is considered to be much shorter than the Hubble time.

On the other hands, Abell1689, which has similar temperature and luminosity(relatively higher than others), dose not exhibit such small line ratio. Though this line ratio anomaly is not common, several of 16 distant clusters show the same tendency.

6.7.4 Summery

- For inner region, within the $5 R_c$, the intensity ratio of K α to K β is well described by CIE.
- The intensity of K α is not depend on the integration radius strongly, then the average value of the abundance derived from K α line seems reliable.
- The intensity of K β line is 2 to 3 times larger than the predicted value in the outer portion of A665 and A1413.
- This couldn't be discribed by temperature gradient and resonance scattering.

- Other process has to be considered to describe this phenomena.

Table 6.8: Intensity ratio of He-like $K\alpha$ to H-like $K\alpha$. Spectrum model consists of bremsstrahlung and two Gaussians (He-like, H-like Fe- $K\alpha$) for SIS. These parameters were obtained from SIS spectrum only.

	R	kT	I(He-like $K\alpha$)	I(H-like $K\alpha$)	$\frac{I(\text{He-like})}{I(\text{H-like})}$	Ionization Temperature
	arcmin.	keV	10^{-5} photons/sec	10^{-5} photons/sec		keV
A665	4	$8.5^{+0.6}_{-0.5}$	$1.4^{+0.5}_{-0.6}$	$0.8^{+0.4}_{-0.6}$	1.75 ± 1.26	$9.2^{+10.0}_{-3.4}$
A1413	4	$6.7^{+1.2}_{-0.6}$	$2.1^{+0.4}_{-0.8}$	$1.3^{+0.7}_{-0.4}$	1.61 ± 0.82	$9.5^{+3.5}_{-1.9}$
A1689	4	$9.8^{+1.3}_{-1.1}$	$2.2^{+1.0}_{-0.5}$	$2.2^{+1.0}_{-0.5}$	1.00 ± 0.48	$11.7^{+8.0}_{-1.9}$

R is the radius of circle in which the spectrum is integrated and kT is the continuum temperature

Table 6.9: Intensity ratio of $K\alpha$ line to $K\beta$ line with GIS. Model spectrum consists of bremsstrahlung and two Gaussians(Fe- $K\alpha$ and Fe- $K\beta$). These parameters were derived from the GIS spectra only.

	R	kT	I($K\alpha$)	I($K\beta$)	$\frac{I(K\alpha)}{I(K\beta)}$	Model Prediction of $I(K\alpha)/I(K\beta)$
	arcmin.	keV	10^{-5} ph./sec	10^{-5} ph./sec		
A665	4	$9.5^{+0.9}_{-0.6}$	$2.2^{+0.7}_{-0.7}$	$0.5^{+0.7}_{-0.5}$	$4.4^{+6.7}_{-4.4}$	5.8
	8	$8.4^{+0.6}_{-0.4}$	$3.2^{+1.1}_{-1.0}$	$1.6^{+1.1}_{-1.0}$	$2.0^{+1.5}_{-1.5}$	6.0
A1413	4	$7.6^{+0.4}_{-0.4}$	$4.4^{+0.9}_{-0.9}$	$0.7^{+0.8}_{-0.7}$	$6.3^{+6.3}_{-6.3}$	6.3
	8	$7.4^{+0.3}_{-0.3}$	$5.5^{+0.8}_{-1.3}$	$1.3^{+1.0}_{-1.0}$	$4.2^{+3.3}_{-3.3}$	6.4
A1689	4	$9.2^{+0.5}_{-0.7}$	$3.5^{+1.2}_{-1.3}$	< 0.7	> 5.0	5.8
	8	$9.7^{+0.4}_{-0.4}$	$5.7^{+1.5}_{-0.9}$	< 0.7	> 8.0	5.8

Figure 6.27: A665 spectrum. Up:GIS, Bottom: SIS

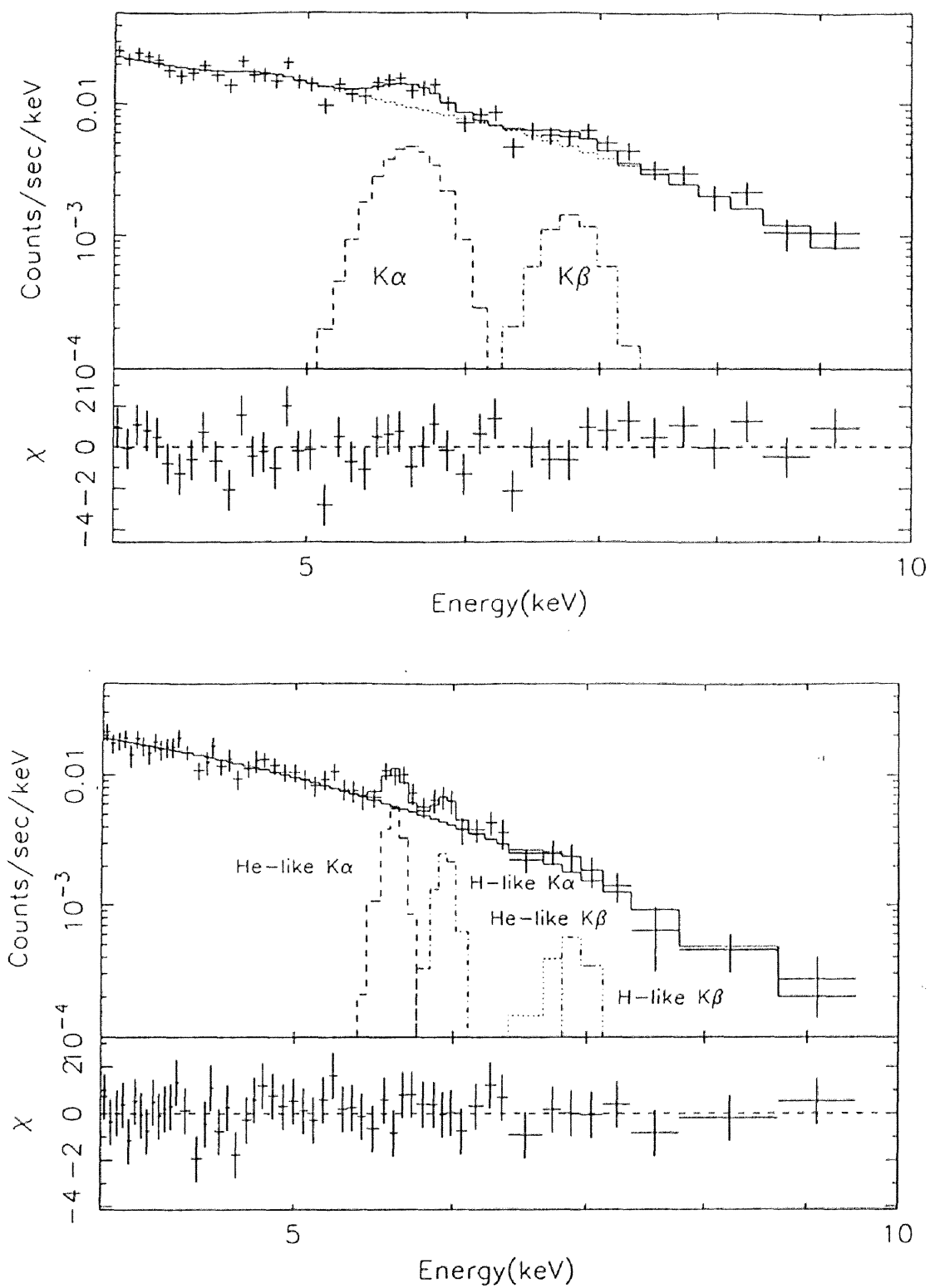


Figure 6.28: A1413 spectrum. Up:GIS, Bottom: SIS

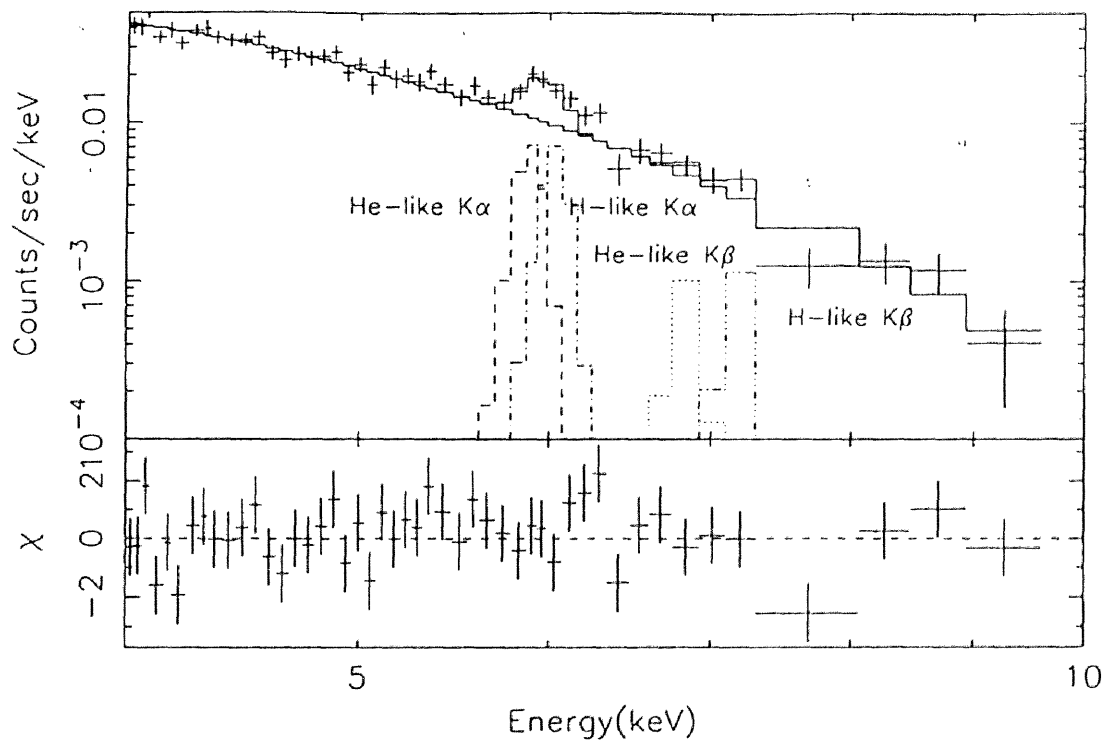
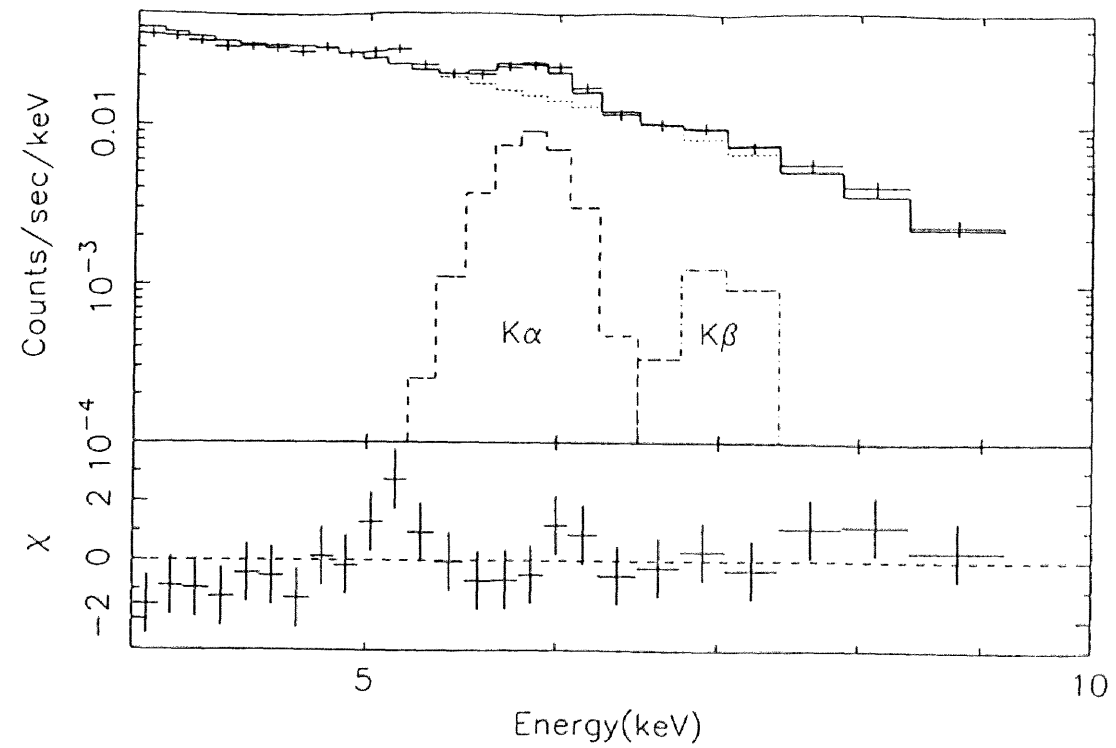


Figure 6.29: A1689 spectrum. Up:GIS, Bottom: SIS

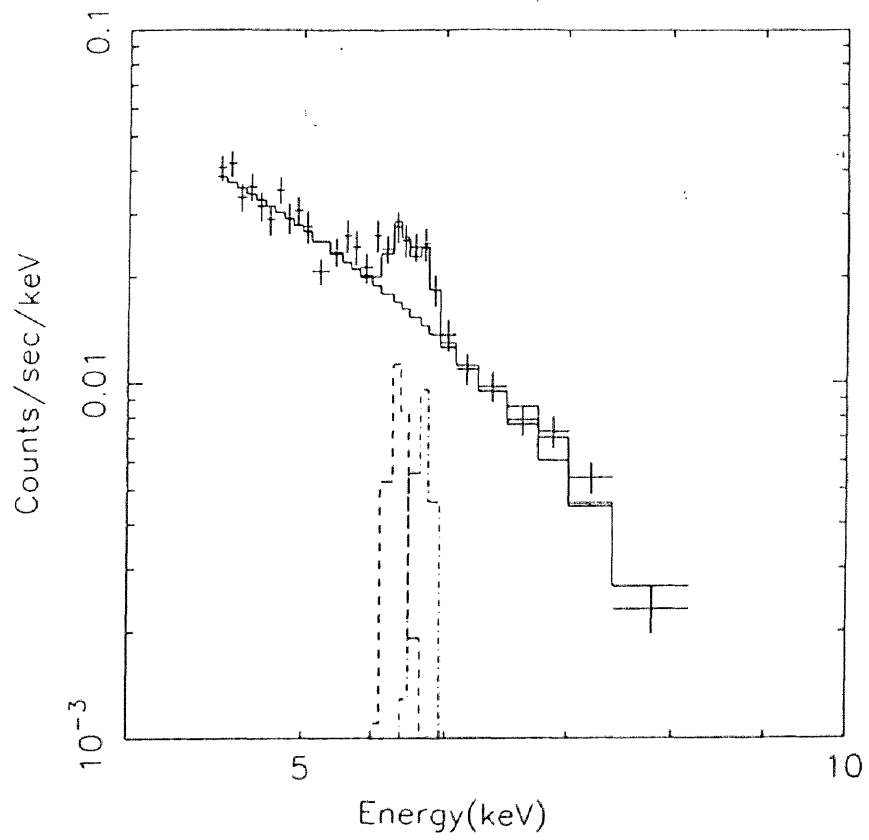
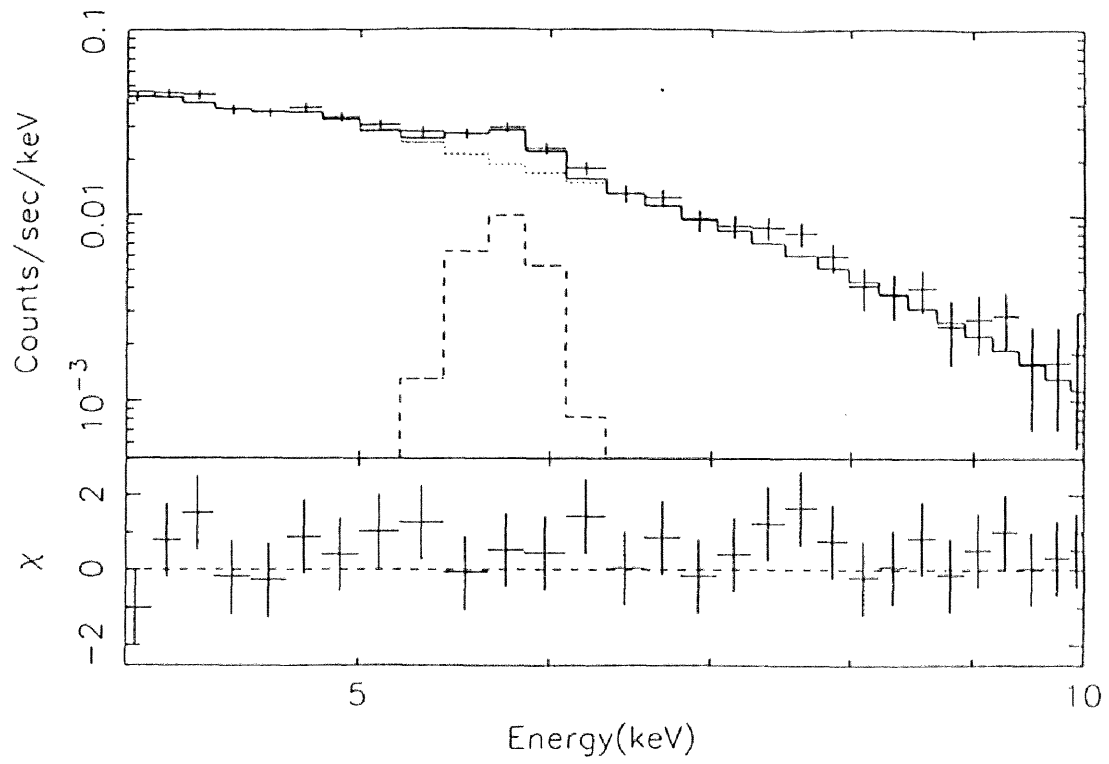


Figure 6.30: Simulated integration radius dependence of the intensity ratio. The simulated conditions are thin iso-thermal ICM(solid line), iso-thermal ICM with resonance scattering(dotted line) and ICM with temperature gradient and resonance scattering(dashed line). The data points with error bar are obtained values from A665.

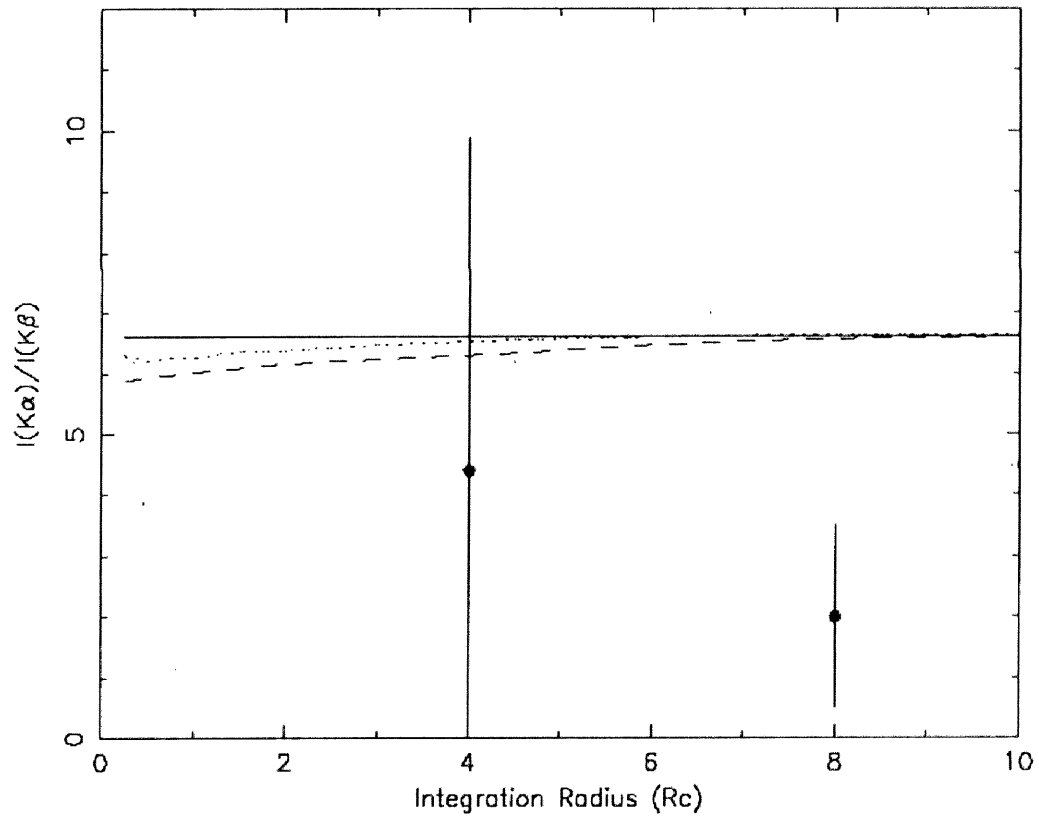


Table 6.10: Effective exposure time and counting rate for each cluster

Target	Sensor	Effective exposure (sec)	Counting rate within r (cts/sec)	r (arcmin.)
Cl0016+16	GIS2	36580	0.052	6
	GIS3	36550	0.053	6
	SIS0	26400	0.061	5
	SIS1	21500	0.067	5
A773	GIS2	43248	0.107	9
	GIS3	43240	0.144	9
	SIS0	39030	0.204	9
	SIS1	38082	0.188	9
A665	GIS2	42256	0.243	9
	GIS3	42240	0.234	9
	SIS0	40127	0.322	9
	SIS1	40192	0.217	9
A2218	GIS2	41955	0.195	9
	GIS3	41953	0.202	9
	SIS0	23651	0.337	9
	SIS1	37268	0.262	9
A1204	GIS2	35170	0.111	10
	GIS3	35170	0.145	10
	SIS0	36292	0.225	5
	SIS1	36298	0.204	5
A1413	GIS2	39466	0.414	9
	GIS3	39484	0.429	9
	SIS0	35186	0.577	9
	SIS1	34922	0.466	9

Chapter 7

Implication for the Hubble constant

7.1 Derivation of H_0

As described in section 3.5, to derive the Hubble constant; H_0 , it is necessary to obtain the spatial distribution of the electron density, the temperature from the X-ray observation and the decrement of the brightness temperature from the radio observation. For the previous H_0 derivations ([Birkinshaw, Hughes & Arnaud 1991], [Birkinshaw & Hughes 1994]), the central density was derived from the central surface brightness obtained by fitting the brightness distribution to the β model with iso-thermal assumption. Then the value of the central brightness has a model dependence; (θ_c, β) (parameter coupling between the central surface brightness and (θ_c, β)).

In this thesis, we define the parameters C_X and Pr for H_0 derivation here. The decrement index; C_X and the profile correction index; Pr are obtained from X-ray observation. Under the basic assumption of spherical symmetry, C_X is independent on the spatial distribution model and indicate the averaged strength of decrement. Pr is derived from the distribution function of the temperature and density, and dose not concerned with the absolute value of the temperature and density. This is the profile correction factor to the averaged strength of decrement.

Using these parameters instead of the central surface brightness and structural parameters (θ_c, β) , it is possible to compare and combine data obtained with various missions without considering the parameter coupling between the central surface brightness and structural parameters¹.

Assuming the spherical symmetric distribution of the temperature and density, the distribution of temperature and density are described as, $n_e(r) = n_{e0}f_{n_e}(r)$, $T_g = T_{g0}f_{T_g}(r)$

¹In some literatures, wrong set of the central surface brightness and structural parameters are used for the Hubble constant derivation ignoring the parameter coupling.

where r is the distance from the center, n_{e0} is the central density, $f_{n_e}(r)$ is a (non-dimensional) distribution function of the density, T_{g0} is the temperature at the center and $f_{T_g}(r)$ is a (non-dimensional) distribution function of the temperature. Using these functions, the central decrement of the brightness temperature and the X-ray flux are expressed as,

$$\frac{\Delta T_r}{T_r} = F(\chi) \frac{2kT_{g0}}{m_e c^2} \sigma_T n_{e0} 2 \int_0^\infty f_{n_e}(r) f_{T_g}(r) dr \quad (7.1)$$

$$F_X(E1, E2) = \frac{n_{e0}^2 \Lambda(T_{g0}; E1', E2')}{4\pi D_L^2} \int_0^\infty f_{n_e}(r)^2 \frac{\Lambda(T_g; E1', E2')}{\Lambda(T_{g0}; E1', E2')} 4\pi r^2 dr$$

where $F(\chi)$ is the term of the frequency dependence of the decrement, D_L is the luminosity distance, $F_X(E1, E2)$ is the observed X-ray flux in the energy range of $E1 - E2$ and $\Lambda(T_g; E1', E2')$ is the thermal bremsstrahlung emissivity in the energy range of $E1' - E2'$ keV ($E1' = (1+z)E1, E2' = (1+z)E2$). $F(\chi)$ have the values of -0.994 for 15 GHz, -0.989 for 20.3 GHz and -0.979 for 28.7 GHz.

Eliminating n_{e0} from above equations, we obtained as following equation,

$$\left(\frac{\Delta T_r}{T_r}\right)^2 = \left(F(\chi) \frac{2kT_{g0}}{m_e c^2} \sigma_T\right)^2 \frac{D_A^2 (1+z)^4 F_X(E1, E2)}{\Lambda(T_{g0}; E1', E2')} \frac{\left(2 \int_0^\infty f_{n_e}(r) f_{T_g}(r) dr\right)^2}{\int_0^\infty f_{n_e}(r)^2 \frac{\Lambda(T_g; E1', E2')}{\Lambda(T_{g0}; E1', E2')} r^2 dr} \quad (7.2)$$

where D_A is the angular diameter distance.

Replacing dr with $D_A d\theta$, the equation of D_A can be derived,

$$D_A = \left(\frac{\Delta T_r}{T_r F(\chi)}\right)^2 C_X^{-2} P_r^{-1} \quad (7.3)$$

$$C_X \equiv \frac{2kT_{g0}}{m_e c^2} \sigma_T \sqrt{\frac{(1+z)^4 F_X(E1, E2)}{\Lambda(T_{g0}; E1', E2')}} \quad (7.4)$$

$$P_r \equiv \frac{\left(2 \int_0^\infty f_{n_e}(\theta) f_{T_g}(\theta) d\theta\right)^2}{\int_0^\infty f_{n_e}(\theta)^2 \frac{\Lambda(T_g; E1', E2')}{\Lambda(T_{g0}; E1', E2')} \theta^2 d\theta} \quad (7.5)$$

Here, if the averaged temperature \bar{T}_g is used instead of T_{g0} , the C_X is observable and a model invariant value.

Since the XRT response depend on the brightness profile, F_X and \bar{T}_g has the dependence on the distribution model. The dependence is much important for the largely

extended nearby clusters. However, it is not influent for the distant clusters. Since the distant cluster shows the small extended image similar to the point source in comparison to nearby clusters, the error due to the uncertainty of the brightness distribution is less than the statistical error.

The angular diameter distance D_A can be expressed as,

$$D_A = \frac{1}{H_0} f_d(z, q_0) \quad (7.6)$$

$$f_d(z, q_0) = \frac{cz}{(1+z)^2} \left[1 + \frac{z(1-q_0)}{1+q_0z+(1+2q_0z)^{1/2}} \right] \quad (7.7)$$

Using the above expressions, the Hubble constant can be derived as,

$$H_0 = \left(\frac{T_r}{\Delta T_r} F(\chi) \right)^2 C_X^2 Pr f_d(z, q_0) \quad (7.8)$$

When the density distribution of the intracluster medium can be expressed with β model (see section 2.4.2) and there is no temperature structure (iso-thermal), Pr has the following formula,

$$Pr = 4\sqrt{\pi} \frac{\Gamma(3\beta)}{\Gamma(3\beta-1.5)} \left(\frac{\Gamma(1.5\beta-0.5)}{\Gamma(1.5\beta)} \right)^2 \quad (7.9)$$

Figure 7.1 shows values of Pr in the (θ_c, β) plane. We assumed the iso-thermal intracluster medium. The effect of the temperature structure will be discussed in section 8.

7.2 X-ray data

We summarized the X-ray data and C_X , Pr in the table 7.1. For A665 and A1413, the result obtained with free N_H fitting is listed.

Figure 7.1 shows the values of Pr in the θ_c, β plane. The error of Pr also listed in table 7.1 were obtained from the figure 7.1 and 90% confidence region in (θ, β) plane of each cluster determined with the 0.5-2.5 keV band radial profile (chapter 6, figure 6.4, 6.8, 6.14, 6.18).

Figure 7.1: (θ_c, β) dependence of Pr

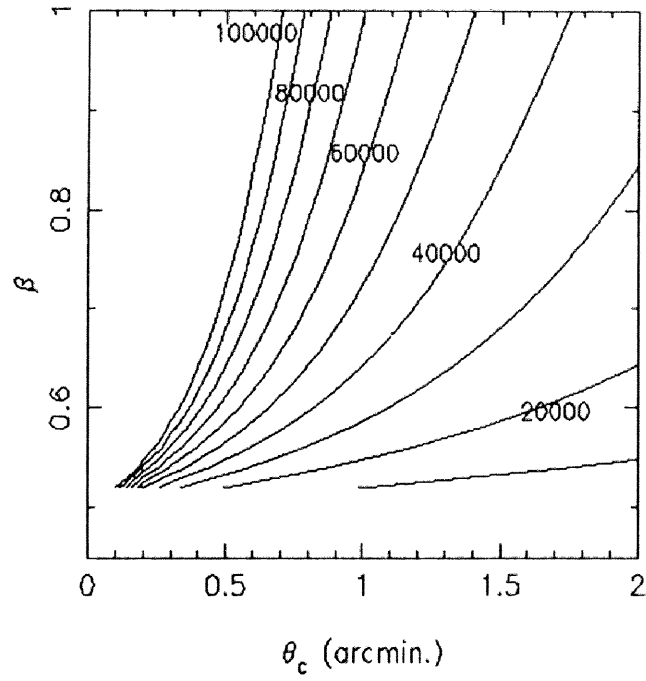


Table 7.1: *ASCA* X-ray data and C_X , Pr for H_0 determination

Target	$\overline{kT_g}$ (keV)	$F_X(2-10\text{keV})$ ($10^{-12}\text{ergs/s/cm}^2$)	C_X^2 (10^{-15}Mpc^{-1})	θ_c (arcmin.)	β	Pr (10^4)
Cl0016+16	8.0 ± 1.0	1.64 ± 0.16	1.65 ± 0.35	0.6	0.70	$7.87^{+2.2}_{-1.5}$
A773	8.7 ± 0.7	6.66 ± 1.00	2.74 ± 0.53	0.8	0.68	5.61 ± 0.9
A665	8.6 ± 0.7	12.4 ± 1.9	4.40 ± 0.85	1.1	0.66	$3.85^{+0.40}_{-0.15}$
A2218	6.7 ± 0.3	8.11 ± 1.22	2.02 ± 0.33	0.9	0.64	$4.39^{+0.50}_{-0.40}$
A1413	7.5 ± 0.4	17.0 ± 2.6	4.38 ± 0.74	0.6	0.58	$4.75^{+0.20}_{-0.20}$
A1204	3.6 ± 0.1	3.85 ± 0.58	0.543 ± 0.106	0.2	0.70	23.60

7.3 Radio data

Decrement data have been obtained by the single dish and interferometer mainly. The table 7.3 shows the published decrement data obtained with the 40m telescope of the Owens Valley Radio Observatory (OVRO40) with 20.3 GHz, the Ryle Telescope (RT) of the Mullard Radio Observatory with 15 GHz and the millimeter array of the Owens Valley Radio Observatory (OVRO10) with 28.7 GHz. The OVRO40 is the single-dish telescope ,and the RT and OVRO10 are the interferometers. The details of these telescopes are listed in table 7.2.

For the single dish observation, ΔT_r is obtained by the efficiency calculation with the telescope response and the radial profile model of the decrement deduced from the X-ray image. Previously, (θ_c, β) obtained from *Einstein* HRI image or assumed parameters were used for the determination of ΔT_r ([Birkinshaw 1991], [Birkinshaw, Hughes & Arnaud 1991], [Birkinshaw & Hughes 1994]).

For the interferometric observations, the decrement image are observable directly and ΔT_r is obtained by fitting the image to the model image produced from the telescopes configuration and decrement model image. For OVRO10 data of Cl0016+16 and A773, (θ_c, β) were derived from the measured decrement image only , however, which have large errors in comparison to the X-ray determination ([Carlstrom *et al.* 1996]).

Since tighter constraints on parameters θ_c, β can be obtained using the X-ray and the measured decrement image rather than using the measured decrement image only, (θ, β) obtained with X-ray images are used in some cases. For RT data of A2218, (θ_c, β) derived from *ROSAT* image were used ([Jones 1993]).

(θ_c, β) for A773 RT data listed in table 7.3 were obtained from *ASCA* image by using Richardson-Lucy method ([Matsuura et al. 1996]). This is the way to restore the convoluted image by a point spread function of a telescope. This method has the difficulty to evaluate the error of model parameters.

ΔT_r listed in table 7.3 are the value at (θ_c, β) and its error contains a random error only. The systematic error due to the model uncertainty is not included.

Table 7.2: Radio Telescopes for S-Z detection

Observatory	telescope	Technique	Frequency	note
OVRO	40 m	Single Dish	20.3 GHz	non-imaging
OVRO	10 m \times 5	Interferometer	28.7 GHz	Baseline 10.4 m - 75 m
MRAO RT	13 m \times 8	Interferometer	15 GHz	Baseline 18 m - 4.8 km

Table 7.3: Derived central decrement of the brightness temperature

Target	Telescope	Used image for (θ_c, β)	ΔT_r	Ref.
cl0016+16	OVRO40	Assumed para., (1.0', 0.8)	0.85 ± 0.11 mK	1
	OVRO10	OVRO10, (0.7', 0.66)	0.717 ± 0.065 mK	2
A773	OVRO10	OVRO10, (0.66', 0.65)	0.590 ± 0.077 mK	2
	RT	ASCA RLmethod, (0.83', 0.62)	0.89 ± 0.10 mK	3
A665	OVRO40	Einstein PSPC, (1.6', 0.66)	0.936 ± 0.083 mK	4
A2218	OVRO40	Einstein PSPC, (1.0', 0.65)	0.62 ± 0.08 mK	5
	RT	ROSAT PSPC, (1.0', 0.64)	$0.90^{+0.06}_{-0.14}$ mK	6
A1204	RT	Negative detection		
A1413	RT	ΔT_0 has not been derived because of the complicated density distribution in ROSAT data.		
Ref.	1: [Birkinshaw 1991], 2: [Carlstrom <i>et al.</i> 1996] 3: [Matsuura et al. 1996], 4: [Birkinshaw, Hughes & Arnaud 1991] 5: [Birkinshaw & Hughes 1994], 6: [Jones 1993]			

7.4 Results

7.4.1 H_0 determination with the published (θ_c, β) and ASCA C_X

For deriving the Hubble constant from the parameters listed in table 7.3, we had to calculate Pr corresponded to the published (θ_c, β) listed in table 7.3 because (θ_c, β) listed in table 7.1 are different from them in 7.3. Otherwise, since C_X has no model dependence, C_X listed in table 7.1 can be used.

The Hubble constant obtained with the published best-fit (θ_c, β) are listed in Table 7.4.

The errors of Pr couldn't be obtained because the 90% confidence region in the (θ_c, β) plane is not available. ΔT_r has the (θ_c, β) dependence but is not considered here.

In the table 7.4, quoted errors were derived by combining errors of C_X and ΔT_r in quadrature.

Obtained Hubble constants are dispersed in the range of 40 to 65 except for the CL0016+16 OVRO40 data and CL0016+16, A773 OVRO10 data.

OVRO10 data for A773, CL0016+16 show a considerably larger value than other results. Carlstrom *et al.* (1996) state that their microwave decrement results are in good

Table 7.4: The Hubble constants obtained with published (θ_c, β)

Target	Pr (10^4)	D_A (Gpc)	$H_0(q_0 = 0)$ (km/s/Mpc)	Data Source
Cl0016+16	5.66	1.1 ± 0.3	82.5 ± 21.2	OVRO40(ΔT_r)+Assumed profile(θ_c, β)
	6.05	0.72 ± 0.20	121 ± 34	OVRO10($\Delta T_r, \theta_c, \beta$)
A773	6.20	0.28 ± 0.09	176 ± 57	OVRO10($\Delta T_r, \theta_c, \beta$)
	4.38	0.86 ± 0.25	56.2 ± 16.6	RT(ΔT_r)+ <i>ASCA</i> (θ_c, β) with Richardson-Lucy method
A665	2.65	1.02 ± 0.27	41.7 ± 10.9	OVRO40(ΔT_r)+ <i>Einstein</i> (θ_c, β)
A2218	4.09	0.63 ± 0.19	64.1 ± 19.4	OVRO40(ΔT_r)+ <i>Einstein</i> (θ_c, β)
	3.95	0.99 ± 0.27	41.4 ± 11.4	RT(ΔT_r)+ <i>ROSAT</i> (θ_c, β)

C_X used for H_0 determination here are our results listed in table 7.1 for all clusters. For Cl0016+16 OVRO40 data, the integration in Pr is not converged. Then the integration procedure was truncated at $10\theta_c$. When we make the integration range large, Pr decrease to 0.

agreement with the X-ray image and temperature quoted by Hughes et al (1995) but do not state the value of H_0 used in the comparison. At present we are not certain as to the origin of the difference between the Carlstrom *et al.* and Birkinshaw *et al.* results, one possibility is that the interferometric data are missing information on large scales.

Other results are consistent with each other. However, the best-fit values of θ_c and β are somewhat different from our results.

7.4.2 H_0 determination with complete data set of our results of Pr , C_X and ΔT_r

For OVRO40 data, it is easy to obtain ΔT_r at the different θ_c and β from published data because of the simple telescope response (Gaussian beam with the half beam width = 107 arcsec). In contrary, for the interferometric data as obtained with OVRO10 and RT, they have complicated telescope response and it is difficult to obtain ΔT_r at different θ_c and β . Then for OVRO40 data, we derive the Hubble constant using the converted central decrement to that at the our best-fit θ_c and β .

Figure 7.2 show the values of ΔT_r in the (θ_c, β) plane for Cl0016+16, A665 and A2218 calculated from the published radio data and the telescope response of OVRO40.

For the X-ray data, the model dependent term and the observable invariant value could be separated by the expressions as equation 7.5. However, the model dependence of ΔT_r is still remained. In order to separate the model dependent term and invariant term in the equation 7.8, the spatial response of the radio telescope is necessary. At present, the telescope response of OVRO40 is only available. Then we calculated the value of Pr' in the (θ_c, β) plane for the OVRO40 observations. Pr' is as follows,

$$Pr' \equiv \left(\frac{T_r}{\Delta T_r} F(\chi) \right)^2 Pr \quad (7.10)$$

Using this expression, the equation 7.8 is separated into the model dependent term and independent term,

$$H_0 = Pr' C_X^2 f_d(z, q_0) \quad (7.11)$$

Figure 7.3 show the value of Pr' in the (θ_c, β) plane for each cluster produced from figure 7.2 and 7.1. We can estimate the 90% confidence range of Pr' in the same manner as estimating the range of Pr (section 7.2).

The Hubble constant obtained by above procedure are listed in table 7.5.

Table 7.5: Hubble constants obtained with our best-fit (θ_c, β)

Target	ΔT_r (mK)	Pr' (10^{11})	D_A (Gpc)	$H_0(q_0 = 0)$ (km/s/Mpc)
Cl0016+16	1.05 ± 0.12	3.52 (2.40 – 4.00)	1.08 (1.46 – 0.58)	80.8 ± 20.8 ($60.0 \pm 15.5 - 102 \pm 26$)
A665	0.965 ± 0.086	3.04 (2.60 – 3.60)	0.748 (0.874 – 0.631)	57.0 ± 15.0 ($48.8 \pm 12.3 - 67.5 \pm 17.6$)
A2218	0.638 ± 0.082	7.92 (5.20 – 8.60)	0.625 (0.952 – 0.576)	65.0 ± 19.7 ($42.7 \pm 12.9 - 70.5 \pm 21.3$)

Quoted errors are random errors combined in quadrature. The range of value noted in the () is the 90% confidence range considering the error of Pr' .

The value of the Hubble constant obtained with our best-fit (θ, β) are well agreement with each other. Using A665 and A2218, the Hubble constant determined with *Einstein's* image, *GINGA's* temperature and OVRO40's radio data has been reported ([Birkinshaw, Hughes & Arnaud 1991], [Birkinshaw & Hughes 1994]) and it is well consistent with our results of *ASCA* and OVRO40 observation.

Figure 7.2: (θ, β) dependence of ΔT_r for OVRO40 data. Top: Cl0016+16, Middle: A665, Bottom: A2218

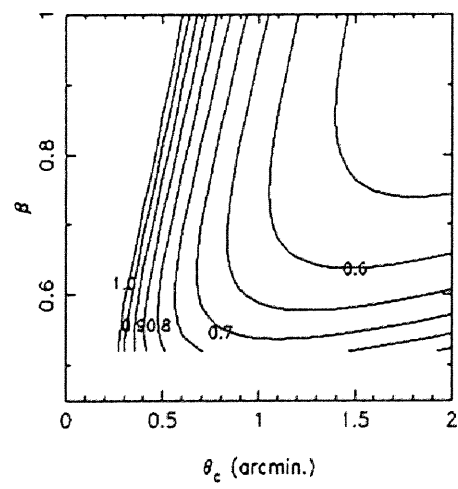
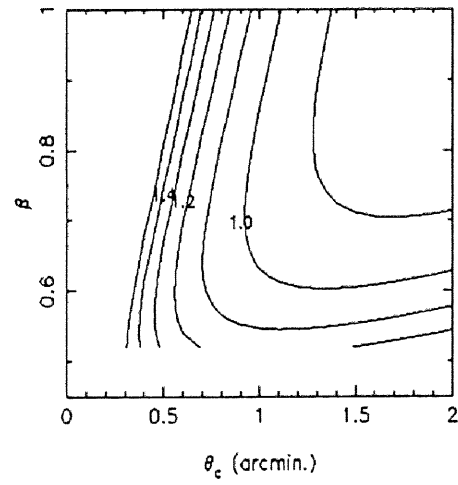
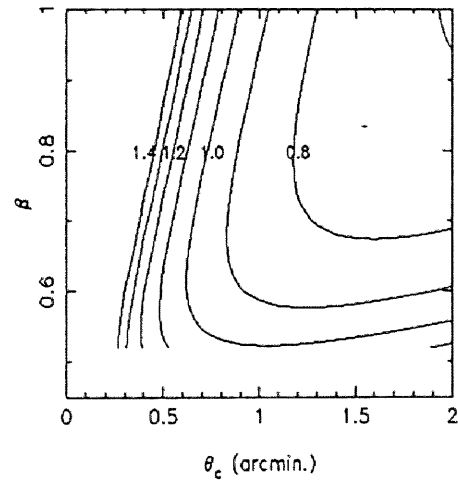
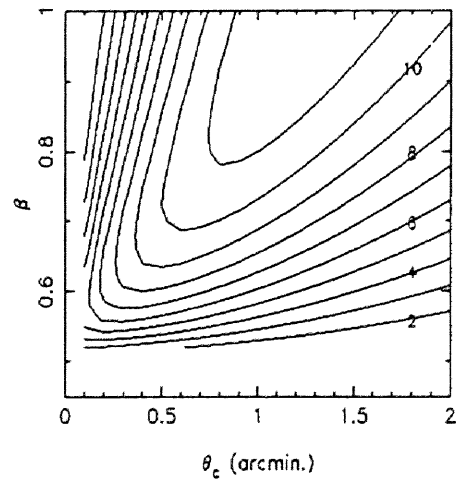
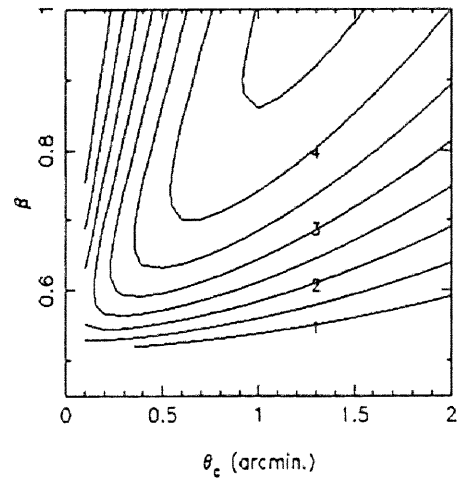
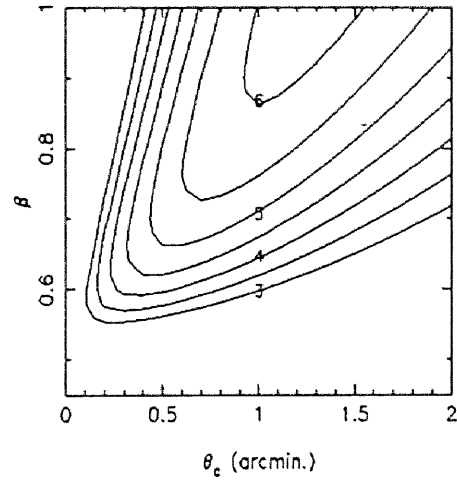


Figure 7.3: (θ, β) dependence of Pr' for OVRO40 data. Top: Cl0016+16, Middle: A665, Bottom: A2218



Chapter 8

Discussion

Our sample of S-Z cluster has great advantage for the determination of the Hubble constant because of using the targets at cosmological distances and in the large distance range; $0.17 < z < 0.54$. The target in that range has a recession velocity of $(5 \sim 12) \times 10^4$ km/s, which seems much larger than the peculiar velocity.

We derived the Hubble constant for each cluster with the published radio data using both (θ_c, β) in the literature and our best-fit (θ_c, β) in the previous chapter. The obtained Hubble constant is in the range of 50 to 80 km sec⁻¹ Mpc⁻¹. It is somewhat lower than the value determined by the optical observation based on Cepheid variables. Before discussing that difference, the uncertainty of our results has to be examined.

The complete results including the (θ_c, β) dependence of ΔT_r are obtained from OVRO40 data for Cl0016+16, A665 and A2218. Other targets and radio data has the (θ_c, β) dependence implicitly and the dependency is unknown. Then we concentrated at the results of OVRO40 data.

8.1 Source of the uncertainty

8.1.1 Off-axis angle uncertainty (Positional uncertainty of the optical axis)

We determined the density distribution from the surface brightness distribution obtained with *ASCA* using the spherical symmetric, iso-thermal β model. The structural parameters have uncertainties due to the positional uncertainty of optical axis of the XRT.

The systematic error due to the optical axis uncertainty can be examined by the fitting with different off-axis angle from that we derived. The model template radial profiles for β model fitting were prepared at the off-axis angle of 0', 5', 10' and 15' (section 5.3). The target is observed at the off-axis angle of ~ 2.5 arcmin. for the SIS0 on a 2CCD mode observation. Then the radial profile obtained with SIS0 was fitted to the β model template

profile at the off-axis angle of $0'$ and $5'$. Using the template at the off-axis angle of $0'$ gives a 0.04 lower value of β than using template at the off-axis angle of $5'$ for all clusters. According to the (θ_c, β) dependence of $PrDT$, its corresponds to the 10% increase of $PrDT$ for Cl0016+16 and A665. For A2218, since ΔT_r is relatively smaller than others, $PrDT$ has strong dependence on β (equation 7.10 and figure 7.3). Then 0.04 increase of β make $PrDT$ large, about 30%.

However, the position of the optical axis was determined with accuracy < 1 arcmin. Then the systematic error of 30% for H_0 is overestimated. It is necessary to reduce the uncertainty of β and to examine the uncertainty due to the positional error of 1 arcmin. Here, we adopt the 10% systematic error of H_0 for all three clusters.

8.1.2 Density and temperature distribution uncertainty

The spherical symmetry and iso-thermal condition has been assumed for the derivation of density distribution. However, from our image analyses in the two energy band (0.5 - 2.5, 2.5 - 10.0 keV) and spectral analyses, and the detailed spatial informations from *ROSAT* observations, some clusters shows the asymmetric distribution of the electron temperature. Then we should consider the effects of relaxing the assumptions.

Elongation

Except for A1413, the brightness distribution obtained with *ASCA* shows the circular symmetry. *Einstein* and *ROSAT* observations of the clusters give high quality images, which show no strong elongation and substructure. Neumann & Böhringer (1996) investigated the elongation of X-ray isophotes for Cl0016+16 (axial ratio ~ 0.82) from detailed analysis with *ROSAT* data. They obtained the results both of azimuthal averaged one dimensional and two dimensional β model fit and confirmed that the core radii for the major and minor axis are within the error of the core radius with one dimensional fit (the difference of central density is less than 1%, [Neumann & Böhringer 1996]). Then for our samples, the error of the Hubble constant due to the elongation seen in the projected image is less than the error due to the core radius uncertainty which has already been included.

Even if the gas distribution is elongated or contracted along the line of sight, the projected image has circular symmetry. However, that distribution causes a underestimation or overestimation of the Hubble constant using the Sunyaev-Zel'dovich effect because of the assumption of the spherical symmetric distribution (the diameter of the cluster along the line of sight should be the same as the transverse diameter). When the ratio of the

diameter along the line of sight to the transverse diameter is defined as ϵ , Pr is expressed as,

$$Pr = 4\sqrt{\pi}\epsilon \frac{\Gamma(3\beta)}{\Gamma(3\beta - 1.5)} \left(\frac{\Gamma(1.5\beta - 0.5)}{\Gamma(1.5\beta)} \right)^2 \quad (8.1)$$

(equation 7.9). Then Hubble constant is proportional to ϵ . Therefore, if the cluster is highly prolate (elongated along the line of sight), then $\epsilon \gg 1$, the true Hubble constant is much smaller than the derived value. For example, A1413 shows the elongation with the axial ratio ~ 1.3 . If this cluster is prolate (and shows the circular symmetric projected image), the true Hubble constant is larger by a factor 1.3 than the derived Hubble constant with the assumption of the spherical symmetry). Birkinshaw Hughes & Arnaud (1991) state that the likely error of the Hubble constant due to the elongation will be a factor 2 deduced from the statistical study of the galaxy distribution. Unfortunately, it is difficult to estimate this value from the observation. The value may be obtained by statistical study of nearby clusters with projected image.

Temperature distribution

ASCA has been investigated the temperature structure in several clusters. Though the Coma cluster (A1656) had been considered as a typical iso-thermal cluster, multiple pointing observations with *ASCA* revealed the structure of the projected temperature evidently ([Honda et al. 1996]). For A665 and A2163, the temperature drop in the outer portion was reported ([Markevitch *et al.* 1994], [Markevitch *et al.* 1996], [Markevitch 1996]).

Our results for some clusters dose not indicate the strong radial structure of the temperature because of the limitation of a radial range for the brightness profile fitting and the large systematic error for the spectral fitting. Considering the maximum profile difference of the radial brightness distribution between the higher (2.5 - 10keV) and lower (0.5 - 2.5 keV) energy band, the radial profile in higher energy band could have 0.06 larger β than the lower band (0.5-2.5) (figure 6.14, 6.18). The allowed range of θ_c of 2.5 - 10 keV range profile with 90% confidence level is too large to investigate the difference from the θ_c for 0.5 - 2.5 keV band. The β difference corresponds to the three-dimensional radial temperature structure, 9 keV at the center and decreasing to 3 keV at $r = 10'$ for A2218 and 11.5 keV at the center and decreasing to 5keV for A665. The central temperature was decided from the obtained temperature averaged over the radial range of $0' - 1.5'$. Assuming the decrease of the temperature described above, we simulated the averaged projected temperatures within the several radii and the results are listed in table 8.1 with the observed averaged projected temperatures. For both case of A2218 and A665, the computed temperature decrease with the integration radius faster than the observed temperature. Then even if a temperature drop exist in the outer part of cluster, the

slope of decrease may be smaller than the assumed temperature gradient for A2218. For A665, since the observed temperature with several integration radii is fairly constant, the temperature may fall down sharply at a large radius; $> 6'$ ([Markevitch 1996]).

In spite of using the strong temperature gradient in comparison to the observed data, Pr changes 10% small. This leads to 10% small H_0 . Then the systematic error due to the temperature gradient seems to be less than 10%.

Table 8.1: Computed averaged temperature with the temperature gradient

Target	Integration region	Computed temperature	Measured temperature
A2218	$0' < r < 1.5'$	7.3 keV	$7.3^{+0.6}_{-0.5}$ keV
	$0' < r < 3.0'$	6.6 keV	$7.3^{+0.4}_{-0.4}$ keV
	$0' < r < 6.0'$	6.1 keV	$6.8^{+0.3}_{-0.3}$ keV
	$0' < r < 9.0'$	6.0 keV	$6.7^{+0.3}_{-0.3}$ keV
A665	$0' < r < 1.5'$	8.8 keV	$8.8^{+0.8}_{-0.7}$ keV
	$0' < r < 3.0'$	7.9 keV	$8.8^{+0.5}_{-0.4}$ keV
	$0' < r < 6.0'$	7.4 keV	$8.7^{+0.3}_{-0.3}$ keV
	$0' < r < 9.0'$	7.2 keV	$8.6^{+0.4}_{-0.4}$ keV

The temperatures listed here are projected temperature.

8.2 Summary of the derived H_0

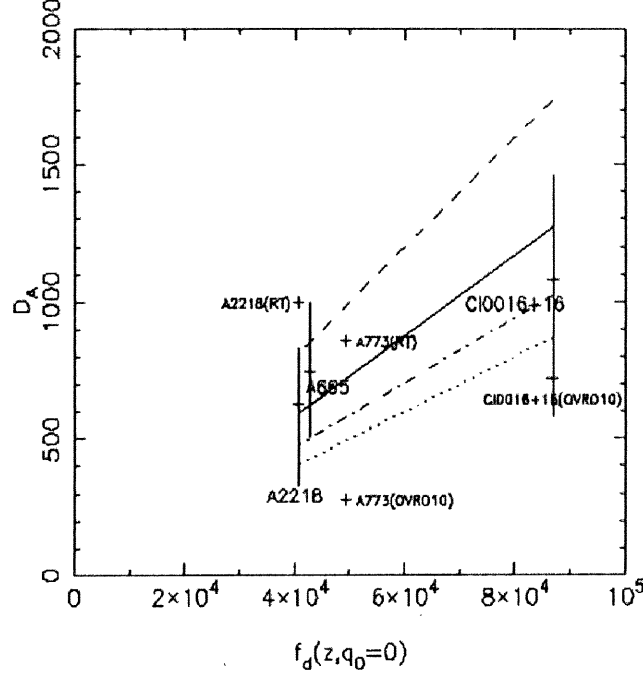
The value of the Hubble constant is obtained from a distance of source one by one. The angular diameter distances obtained from all sources are plotted with the value of $f_d(z, q_0 = 0)$ (equation 8.2) in figure 8.1. For OVRO40 data, quoted error bars include systematic error discussed above. For RT and OVRO10 data, since the central decrement with our best-fit (θ_c, β) could not be calculated because of the unknown telescope response, the values obtained from our results of the electron temperature, X-ray flux, and published ΔT_r with (θ_c, β) derived from other data (*Einstein* image or decrement image; see chapter 7) are plotted. The error bars of RT and OVRO10 do not include the systematic error.

The diameter distance can be expressed as,

$$D_A = H_0^{-1} f_d(z, q_0) \quad (8.2)$$

$$f_d = \frac{cz}{(1+z)^2} \left[1 + \frac{z(1-q_0)}{1+q_0z+(1+2q_0z)^{1/2}} \right]$$

Figure 8.1: Summary of the derived H_0 . Vertical axis expresses the measured diameter distance and horizontal axis is the value of $f_d(z, q_0 = 0)$. Solid line is the best-fit with $H_0 = 68$. Dashed line, dot-dashed line and dotted line corresponds to $H_0 = 50$, $H_0 = 85$ and $H_0 = 100$, respectively. Though the results from the incomplete data for RT and OVRO10 are also plotted, they were not used for fitting.



(equation 3.12).

Then using f_d and obtained D_A for each cluster and including all the systematic errors, H_0 can be obtained by fitting to the linear function.

Figure 8.1 shows the fitted results of H_0 using the OVRO40 data (A2218, A665 and C10016+16) as solid line. We obtained the best-fitted Hubble constant = 68 ± 22 km sec⁻¹ Mpc⁻¹ including the systematic error discussed above (only the systematic error due to the elongation is not included).

8.3 Difference from other methods

The distance measurement using the standard candles has been improved by HST observation. The distance measurement based on the P-L relation of Cepheids. The Cepheid in the Virgo cluster galaxy M100 have been observed and the derived Hubble constant is around 82 ± 17 km sec⁻¹ Mpc⁻¹ (Freedman et al 1994, Pierce et al 1994). Though it is

consistent with our result, somewhat larger than ours. There are several way to describe that discrepancy as follows,

1. Systematic error in the S-Z effect.
2. Systematic error in the distance measurement to Virgo cluster.
3. The Hubble constant is not '*constant*'.
4. Trick of the cosmological model. The Hubble constant is really '*constant*'.

8.3.1 Systematic error in the S-Z effect

The systematic errors for the determination with S-Z effect has been discussed, though the effect of a elongation of intracluster medium has not been included. If the Hubble constant is really '*constant*' and $80 \text{ km sec}^{-1} \text{ Mpc}^{-1}$, all clusters of our sample should be elongated along the line of sight and its axial ratio should be $1.3 \sim 1.6$. The value of the axial ratio is not unlikely. But it is hard to consider that all four clusters show the elongation along the same direction and such a large axial ratio. However, we should wait to discuss it until the increase of S-Z cluster sample.

Then next, we examine the reliability of the distance measurement to Virgo cluster briefly.

8.3.2 Systematic error in the distance measurement to Virgo cluster

Freedman et al. (1994) assumed that M100 is located at the same distance as the Virgo cluster core from us. The Virgo cluster has large extent even in the direction along the line of sight. If M100 is located at the near-side of the Virgo cluster, it may lead to underestimate the distance to the Virgo cluster. This uncertainty is comparable or large with their quoted error of the distance. Furthermore, there is difficulty to estimate the recession velocity of the Virgo cluster. The Virgo cluster has two main components of galaxy concentration and additional component which is more distant than the two main components. Since these subclusters seems to show the systematic motion respectively, the averaged Virgo recession velocity should be estimated carefully. The deduced recession velocity of the Virgo cluster are ranging $1100 \sim 1600 \text{ km/s}$ ([Tammann et al. 1996], [Freedman et al. 1994]). Considering the systematic error, the Hubble constant is in the range of $65 - 100 \text{ km sec}^{-1} \text{ Mpc}^{-1}$.

The distance measurement with SNe Ia is applicable to $\sim 400 \text{ Mpc}$ and the uncertainty noted above is not serious at large distance because of large recession velocity. The distance measurements using the peak magnitude of SNe Ia and the calibration

with the Cepheid distance has been developed ([Saha et al. 1994], [Sandage et al. 1996], [Schaefer et al. 1996]). However, the peak absolute magnitude dependence on the decline rate of the magnitude is suggested by Riess et al. (1995). They estimated the Hubble constant without limitation of the constant peak magnitude and obtained $67 \pm 7 \text{ km sec}^{-1} \text{ Mpc}^{-1}$ (with limitation of the constant peak magnitude, derived H_0 is $53 \pm 11 \text{ km sec}^{-1} \text{ Mpc}^{-1}$).

Though the Hubble constant obtained with nearby objects tend to prefer the short distant scale ($> 65 \text{ km sec}^{-1} \text{ Mpc}^{-1}$) to the long distant scale ($< 65 \text{ km sec}^{-1} \text{ Mpc}^{-1}$) except for the value from SN Ia method, it is impossible to decide at present. It must be noted that the large value of H_0 lead to the paradoxical problem on the age of universe. According to the age estimation of globular clusters based on the comparing the stellar populations and calibrated stellar models, the oldest globular cluster has the age of $15.8 \pm 2.1 \text{ Gyr}$ ([Bolte & Hogan 1995]). For Einstein - de Sitter universe, the age of universe is 8 Gyr with $H_0 = 80 \text{ km sec}^{-1} \text{ Mpc}^{-1}$ and 13 Gyr with $H_0 = 50 \text{ km sec}^{-1} \text{ Mpc}^{-1}$. To avoid the problem, the universe should be low density with $H_0 < 65 \text{ km sec}^{-1} \text{ Mpc}^{-1}$ or non zero Λ universe. According above discussions and our results, the Hubble constant is likely around this value.

8.3.3 Local and Global value of the Hubble constant

S-Z method has applied to much further objects than the Cepheid, Tully-Fisher methods. If all measurement are correct, it is considerable that the Hubble constant is not 'constant' and it has a distance dependence. If there is low density region in comparison to the global density and our local group is in that region, the Hubble constant has distance dependence because of the different deceleration rate of expansion. Wu et al. (1995) calculated the distance dependence of the 'local' Hubble constant with the simple density model which is the King model with the core radius is several tens Mpc and the central density as small as 0.0125 times of the 'global' density. This cause that the 'local' Hubble constant within the distance of 100 Mpc is larger than the 'global' one. Though it is only demonstration, it is one of the model to express the distance dependence of the measured Hubble constant.

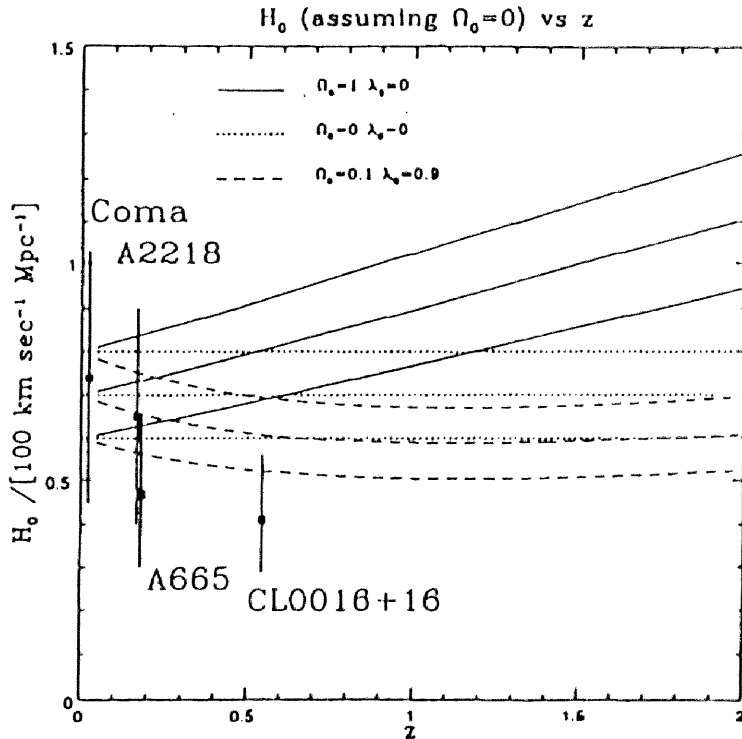
More sophisticated method to examine the effect of density fluctuation has been developed by Turner, Cen & Ostriker (1992) using the N-body simulation, Suto, Sugimoto & Inagaki (1995), Nakamura & Suto (1995) using the analytical formulation. They assumed the density fluctuation in the cold dark matter (CDM) model and obtained the probability distribution function (PDF) of the global Hubble constant with the local (observed) value of $H_0 = 80 \text{ km sec}^{-1} \text{ Mpc}^{-1}$. According their results of PDF, the probability of the global Hubble constant being below $50 \text{ km sec}^{-1} \text{ Mpc}^{-1}$ is 6% with $\Omega_0 = 1$ and 4% with

$\Omega_0 = 0.2$. This seems to be inconsistent with our results. This result has the CDM model dependency and the propriety of CDM model is still not reliable at present.

8.3.4 Dependence on the cosmological model (Ω_0 q_0)

We derived the Hubble constant assuming $q_0 = 0$. If Ω_0 and/or Λ is not zero, the obtained Hubble constant shows the apparent dependence on the distance because of the different expression of the angular diameter distance D_A (equation 3.12). In this case, the Hubble constant is really 'constant'. Figure 8.2 shows the apparent dependence of the Hubble constant obtained with $q_0 = 0$ on redshifts with constant H_0 and three cosmological model $(\Omega_0, \lambda_0) = (1.0, 0.0)$, $(0.0, 0.0)$ and $(0.1, 0.9)$ ([Sasaki 1995]). The case of $(0.0, 0.0)$ corresponds to $q_0 = 0$. According to this figure, the low density and non zero Λ universe is favor to describe the difference between the Hubble constant obtained with nearby object and that obtained with distant clusters. However, the error of the measured Hubble constant is too large to examine the cosmological model dependence.

Figure 8.2: Apparent distance dependence of the Hubble constant due to the use of different cosmological model.



Chapter 9

Conclusion

We analyzed 6 distant clusters of galaxies observed with *ASCA* data and obtained accurate averaged temperatures and luminosities. Furthermore, we developed the method of the image analyses using the β model fitting in the 2 energy bands including the effect of the XRT PSF, and obtained the structural parameters (θ_c, β) for each cluster.

ASCA observation of Cl0016+16 provide us the temperature and luminosity for the first time. This is the furthest cluster of which temperature has been obtained.

We found the point like emission from A1204. Detailed spectral analysis, it is identified as the thermal emission associated with A1204 by the redshifted iron line and continuum emission. The point like brightness distribution is produced by the strong peak at the center of the cluster and the radial distribution of the hardness ratio suggests the existence of a cool component in the central region.

For A665 and A1413, the strong iron $K\alpha$ and $K\beta$ line emission are seen in the X-ray spectra. We found the anomaly of the ratio of $K\alpha$ to $K\beta$ line intensity. This anomaly can not be described with the collisional ionization equilibrium. We made it sure that the anomaly of the ratio occur in the outer skirt of the cluster and suggest the breakdown of the condition in the collisional ionization equilibrium in the outer low density region of the cluster.

For the previous determination of the Hubble constant using the Sunyaev-Zel'dovich effect, the combined X-ray data with *Einstein* and *GINGA* are used. *GINGA* and *Einstein* which is the imaging and non-imaging instrument respectively, have much different in the energy range, spatial resolution and imaging capability.

We derive the Hubble constant using the Sunyaev-Zel'dovich effect with the complete radio data obtained with OVRO 40m single-dish radiometer and X-ray data obtained with only *ASCA* for the three clusters of galaxies, A2218, A665 and Cl001616+16, incomplete radio data obtained with OVRO 10m and MRAO Ryle telescope interferometer

and complete X-ray data for A2218, A773 and Cl0016+16.

In the process of the derivation, we introduced the observable physical parameters as 'the decrement index' (C_X) which is independent of the distribution function of the temperature and density, and 'the profile correction index' (Pr) which depends on the distribution function. These parameters make it possible to compare or to combine with the data obtained with the different missions (*e.g.* *Einstein* *ROSAT* *GINGA* and *ASCA*) without the immanent parameter coupling problem such as the coupling between a central density and structural parameters (θ_c, β).

Including the considerable systematic errors except for the elongation, the Hubble constant was obtained $68 \pm 22 \text{ km sec}^{-1} \text{ Mpc}^{-1}$. Since the targets are in the cosmological distance range ($0.17 \geq z \leq 0.54$), the obtained Hubble constant is not 'local' but 'global' value in the universe. The incomplete radio data except the radio data of OVRO 10m also provide $< 80 \text{ km sec}^{-1} \text{ Mpc}^{-1}$. The radio data obtained with OVRO 10m show the considerably higher value $> 120 \text{ km sec}^{-1} \text{ Mpc}^{-1}$ than our results and any previous result including the results from the nearby objects.

Our result from complete data of A2218, A665 and Cl0016+16 is relatively lower than the 'local' value of the Hubble constant; $80 \text{ km sec}^{-1} \text{ Mpc}^{-1}$ obtained from Cepheids HST observation in Virgo cluster.

At present, though there are several ideas to describe such a difference, it is hard to conclude because there is still uncertainty in the derivation of the 'local' value of the Hubble constant ($50 \text{ km sec}^{-1} \text{ Mpc}^{-1}$ derived with SNe Ia or $80 \text{ km sec}^{-1} \text{ Mpc}^{-1}$ Virgo Cepheids).

The best way to derive the precise Hubble constant is to measure distances to objects in the wide redshift range including the distance to the Virgo and Coma cluster based on the purely physical methods such as the Sunyaev-Zel'dovich effect. If the accurate radio data of nearby clusters are available, *ASCA* can derive the 'true' Hubble constant from the 'local' to 'global'.

ACKNOWLEDGMENTS

I am grateful to Profs. K. Yamashita, H. Kunieda, and Y. Tawara for their continuous support and guidance throughout my doctoral course. I would like to thank to Dr S. Miyoshi, Mr. M. Matsuura and Dr. M. Jones, for useful comments for the analyses and informations of radio observations. I would also like to express my thank to Dr. R. F. Mushotzky and Dr. M. Markevitch for useful discussion.

Thanks are due to all members in the X-ray laboratory for their help, particularly Dr. Y. Kamata, M. Watanabe and T. Yoshioka for their system management of Work stations. Also thanks to Ms. F. Akimoto, Mr. K. Misaki, M. Watanabe, T. Yoshioka for preparing the figures, and to Y. Terashima for valuable discussions and suggestions.

I am grateful to the XRT team, GIS team and ASCA-ANL/SimASCA team for their efforts and collaboration on the XRT calibration and tuning.

I would like to express my thank all the member of the *ASCA* team and duty scientists.

This research was made under the support of the JSPS.

Bibliography

- [Abell 1958] Abell, G. O. 1958, *Astrophys. J. Suppl.*, 302, 211
- [Abell, Corwin & Olowin 1989] Abell, G. O., Corwin, H. G., Olowin, R. P. 1989, *Astrophys. J. Suppl.*, 70, 1
- [Allen et al. 1992] Allen, S. W., Edge, A. C., Fabian, A. C., Böhringer, H., Crawford, C. S., Ebeling, H., Johnstone, R. M., Naylor, T., Schwartz, R. A., 1992, *Mon. Not. R. Astron. Soc.*, 259, 67
- [Allen et al. 1995] Allen, S. W., Fabian, A. C., Edge, A. C., Böhringer, H., White, D. A., 1995, *Mon. Not. R. Astron. Soc.*, 275, 741
- [Aschenbach 1988] Aschenbach, B., 1988, *Appl. Optics*, 27, 1404
- [Bautz & Morgan 1970] Bautz, L. P., Morgan, W. W. 1970, *Astrophys. J.*, 162, L149
- [Belloni & Röser 1996] Belloni, S., Röser, H. P., 1996, *Astron. & Astrophys.*, 118, 65
- [Birkinshaw & Gull 1984b] Birkinshaw, M., Gull, S. F., 1984, *Mon. Not. R. Astron. Soc.*, 206, 359
- [Birkinshaw & Hughes 1994] Birkinshaw, M., Hughes, J. P., 1994, *Astrophys. J.*, 420, 33
- [Birkinshaw, Gull & Hardebeck 1984a] Birkinshaw, M., Gull, S. F., Hardebeck, H., 1984, *Nature*, 309, 34
- [Birkinshaw, Hughes & Arnaud 1991] Birkinshaw, M., Hughes, J. P., Arnaud, K. A., 1991, *Astrophys. J.*, 379, 466
- [Birkinshaw 1991] Birkinshaw, M., 1991, in *Physical Cosmology*(ed. Tran Thanh Yan), 177
- [Bolte & Hogan 1995] Bolte, M., Hogan, C. J., 1995, *Nature*, 376, 399
- [Branch & Tammann 1992] Branch, D., Tammann, G. A., 1992, *Annu. Rev. Astron. Astrophys.*, 30, 359

- [Branch, Romanishins & Baron 1996] Branch, D., Romanishins, W., Baron, E., 1996, *Astrophys. J.*, 465, 73
- [Butcher & Oemler 1978] Butcher, H., Oemler, A., 1978, *Astrophys. J.*, 219, 18
- [Butcher & Oemler 1984] Butcher, H., Oemler, A., 1984, *Astrophys. J.*, 285, 426
- [Carlstrom *et al.* 1996] Carlstrom, J. E., Joy, M. & Grego, L., 1996, *Astrophys. J. Lett.*, 456, L75
- [Castander *et al.* 1995] Castander, F. J., Bower, R. G., Elis, R. S., Aragon-Salamanca, A., Mason, K. O., Hasinger, G., McMahon, R. G., Carrera, F. J., Mittaz, J. P. D., Perez-Fournon, I., Lehto, H. J. 1995, *Nature*, 377, 7
- [Crawford *et al.* 1993] Crawford, C. S., Edge, A. C., Fabian, A. C., Allen, S. W., Böhringer H., Ebeling, H., McMahon, R. G., Voges, W., 1993, *Mon. Not. R. Astron. Soc.*, 274, 75
- [Crone, Evrard & Richstone 1994] Crone, M. M., Evrard, A. E., Richstone, D. O., 1994, *Astrophys. J.*, 434, 402
- [David *et al.* 1993] David, L. P., Slyz, A., Jones, C., Forman, W. & Vrtillek, S. D., 1993, *Astrophys. J.*, 412, 479
- [de Korte *et al.* 1981] de Korte, P. A. J., Giralt, R., Coste, J. N., Ernu, C., Frindel, S., Flamand, J., Contet, J. J., 1981, *Appl. Optics*, 20, 1080
- [Edge & Stewart 1991] Edge, A. C. & Stewart, G. C., 1991, *Mon. Not. R. Astron. Soc.*, 252, 414
- [Edge *et al.* 1990] Edge, A. C., Stewart, G. C., Fabian, A. C., Arnaud, K. A. 1990, *Mon. Not. R. Astron. Soc.*, 245, 559
- [Fabian 1994] Fabian, A. C., 1994, *Annu. Rev. Astron. Astrophys.*, 32, 277
- [Fabricant, McClintock & Bautz 1991] Fabricant, D. G., McClintock, J. E., Bautz, M. W., 1991, *Astrophys. J.*, 381, 33
- [Forman & Jones 1982] Forman, W., Jones, C. 1981, *Annu. Rev. Astron. Astrophys.*, 20, 547
- [Freedman *et al.* 1994] Freedman, W. L., Madore, B. F., Mould, J. R., Hill, R., Ferrarese, L., Kennicutt Jr, R. C., Saha, A., Stetson, P. B., Graham, J. A., Ford, H., Hoessel, J. G., Huchra, J., Hughes, S. M., Illingworth, G. D., 1994, *Nature*, 371, 757

- [Friedman et al 1951] Friedman, H., Lichtman, S., Byram, E. 1951, Phys. Rev. Lett., 83, 1025
- [Giacconi et al 1962] Giacconi, R., Gursky, H., Paolini, F., Rossi, B. 1962, Phys. Rev. Lett., 9, 439
- [Grainge *et al.* 1993] Grainge, K., Jones, M., Pooley, G., Saunders R., Edge, A., 1993, Mon. Not. R. Astron. Soc., 265, L57
- [Grainge *et al.* 1996] Grainge, K., Jones, M., Pooley, G., Saunders R., Baker, J., Haynes, T., Edge, A., 1996, Mon. Not. R. Astron. Soc., 278, L17
- [Höflich & Khokhlov 1996] Höflich, P., Khokhlov, A., 1996, Astrophys. J., 457, 500
- [Henke et al. 1982] Henke, B. L., Lee, P., Tanaka, T. J., Shimabukuru, R. L., Fujikawa, B. K., 1982, Atomic Data and Nuclear Data Tables, 27, 1
- [Henke, Gullikson & Davis 1993] Henke, B. L., Gullikson, E. M., Davis, J. C., 1993, Atomic Data and Nuclear Data Tables, 54, 181
- [Henry et al. 1992] Henry, J. P., Gioia, I. M., Maccacaro, T., Morris, S. L., Stocke, J. T., Wolter, A., 1992, Astrophys. J., 386, 408
- [Honda et al. 1996] Honda, H., Hirayama, M., Watanabe, M., Kunieda, H., Tawara, Y., Yamashita, K., Ohashi, T., Hughes, J. P., Henry, J. P., 1996, Astrophys. J. Lett., 473, L71
- [Hughes & Birkinshaw 1995] Hughes, J. P. & Birkinshaw, M., 1995, Astrophys. J. Lett., 448, L93
- [Hughes & Tanaka 1992] Hughes, J. P., Tanaka, Y., 1992, Astrophys. J., 398, 62
- [Ikebe 1996] Ikebe, Y 1996, Ph. D. Thesis, Tokyo University
- [Inoue et al. 1978] Inoue, H. et al. 1978, Nucl. Inst. and Meth., 157, 295
- [Jones 1993] Jones, M., 1993, proceedings
- [Jones & Forman 1991] Jones, C., Forman, W., 1991, in “Clusters and Superclusters of galaxies”, ed A. C. Fabian, (Dordrecht:Kluwer), 49
- [Jones et al. 1993] Jones, M., Saunders, R., Alexander, P., Birkinshaw, M., Dillon, N., Grainge, K., Hancock, S., Lasenby, A., Lefebvre, D., Pooley, G., Scott, P., Titterton, D., Wilson, D., 1993, Nature, 365, 320

- [Kaastra and Mewe 1993] Kaastra, J. S., Mewe, R., 1993, *Astron. & Astrophys. Suppl.*, 97, 443
- [Kaiser 1991a] Kaiser, N., 1991, *Astrophys. J.*, 366, 388
- [Kaiser 1991b] Kaiser, N., 1991, *Astrophys. J.*, 383, 104
- [Kato 1978] Kato, T 1978, IPPJ-AM-4
- [King 1962] King, I. R. 1962, *Astron. J.*, 67, 471
- [Koo 1981] Koo, D. C., 1981, *Astrophys. J. Lett.*, 251, L75
- [Koyama et al. 1984] Koyama, K. et al. 1984, *Publ. Astron. Soc. Japan*, 36, 659
- [Kumada et al. 1996] Kumada, A., Furuzawa, A., Tawara, Y. & Yamashita, K., 1996, *Proceedings of "X-ray Imaging and Spectroscopy of Cosmic Hot Plasmas"*, in press
- [Kunieda et al. 1993] Kunieda, H., Tsusaka, Y., Suzuki, H., Ogasaka, Y., Awaki, H., Tawara, Y., Yamashita, K., Yamazaki, T., Itoh, I., Kii, T., Makino, F., Ogawara, Y., Tsunemi, H., Hayashida, K., Nomoto, S., Wada, M., Miyata, E., Hatsukade, I., 1993, *Japan J. Appl. Phys.*, 32, 4805
- [Makishima et al. 1996] Makishima, K. et al. 1996, *Publ. Astron. Soc. Japan*, 48, 171
- [Markevitch 1996] Markevitch, M., 1996, *Astrophys. J.*, 465, 1
- [Markevitch *et al.* 1994] Markevitch, M., Yamashita, K., Furuzawa, A., Tawara, Y., 1994, *Astrophys. J. Lett.*, 436, L71
- [Markevitch *et al.* 1996] Markevitch, M., Mushotzky, R. F., Inoue, H., Yamashita, K., Furuzawa, A., Tawara, Y., 1996, *Astrophys. J.*, 456, 437
- [Masai 1984] Masai, K., 1984, *Astrophys. Space Sci.*, 98, 367
- [Mathews, Morgan & Schmit 1964] Mathews, T. A., Morgan, W. W., Schmidt, M. 1964, *Astrophys. J.*, 140, 35
- [Matsuura et al. 1996] Matsuura, M., Miyoshi, S. J., Yamashita, K., Tawara, Y., Furuzawa, A., Lasenby, N., Saunders, R., Jones, M., Hatsukade, I., 1996, *Proceedings of "X-ray Imaging and Spectroscopy of Cosmic Hot Plasmas"*, in press
- [McHardy et al. 1990] McHardy, I. M., Stewart, G. C., Edge, A. C., Cooke, B., Yamashita, K., Hatsukade, I., 1990, *Mon. Not. R. Astron. Soc.*, 242, 215

- [Mitchell et al. 1976] Mitchell, R. J., Culhane, J. L., Davison, P. J., Ives, J. C. 1976, Mon. Not. R. Astron. Soc., 176, 29
- [Mitchell et al. 1977] Mitchell, R. J., Ives, J. C., Culhane, J. L. 1977, Mon. Not. R. Astron. Soc., 131, 25
- [Mitchell et al. 1979] Mitchell, R. J., Dickens, R. J., Bell Burnell, S. J., Culhane, J. L. 1979, Mon. Not. R. Astron. Soc., 189, 329
- [Moffet & Birkinshaw 1989] Moffet, A. T., Birkinshaw, M., 1989, Astron. J., 98, 1148
- [Mushotzky 1996] Mushotzky, R., 1996, The proceedings of Rontgenstrahlung from the Universe
- [Mushotzky et al. 1978] Mushotzky, R. F., Serlemitsos, P. J., Smith, B. W., Boldt, E. A., Holt, S. S. 1978, Astrophys. J., 225, 21
- [Nakamura & Suto 1995] Nakamura, T. T., Suto, Y., Astrophys. J. Lett., 447, L65
- [Neumann & Bohringer 1996] Neumann, D. M. & Bohringer, H., 1996, Mon. Not. R. Astron. Soc., in press
- [Ohashi et al. 1996] Ohashi, T. et al. 1996, Publ. Astron. Soc. Japan, 48, 157
- [Partridge et al. 1987] Partridge, R. B., Perley, R. A., Mandolezi, N., Delphino, F., 1987, Astrophys. J., 317, 112
- [Pello et al. 1992] Pello, R., Le Borgne, J. F., Sanahuja, B., Mathez, G., Fort, B., 1992, Astron. & Astrophys., 266, 6
- [Raymond and Smith 1977] Raymond, J. C., Smith, B. W., 1977, Astrophys. J. Suppl., 35, 419
- [Riess, Press & Kirshner 1995] Riess, A. G., Press, W. H., Kirshner, R. P., 1995, Astrophys. J. Lett., 438, L17
- [Rood & Sastry 1971] Rood, H. J., Sastry, G. 1971, PASP, 83, 313
- [Saha et al. 1994] Saha, A., Labhardt, L., Schwengeler, H., Macchetto, F. D., Panagia, N., Sandage, A., Tammann, G. A. ,1994, Astrophys. J., 425, 14
- [Sandage 1996] Sandage, A., 1996, Proc. of Science with the Hubble Space Telescope - II, in press
- [Sandage et al. 1996] Sandage, A., Saha, A., Tammann, G. A., Labhardt, L., Panagia, N., Macchetto, F. D., 1996, 460, L15

- [Sarazin 1986] Sarazin, C. L. 1986, *Rev. Mod. Phys.*, 58, 1
- [Sasaki 1995] Sasaki, S., 1995, private communication
- [Schaefer et al. 1996] Schaefer, B. E., 1996, *Astrophys. J. Lett.*, 460, L19
- [Schindler & Muller 1993] Schindler, S., Muller, E., 1993, *Astron. & Astrophys.*, 272, 137
- [Serlemitsos 1988] Serlemitsos, P. J. 1988, *Appl. Optics*, 27, 1447
- [Serlemitsos et al. 1977] Serlemitsos, P. J., Smith, B. W., Boldt, E. A., Holt, S. S., Swank, J. H. 1977, *Astrophys. J.*, 211, L63
- [Serlemitsos et al. 1995] Serlemitsos, P. J., Jalota, L., Soong, Y., Kunieda, H., Tawara, Y., Tsusaka, Y., Suzuki, H., Sakima, Y., Yamazaki, T., Yoshioka, H., Furuzawa, A., Yamashita, K., Awaki, H., Itoh, M., Ogasaka, Y., Honda, H., Uchibori, Y. 1995, *Publ. Astron. Soc. Japan*, 47, 105
- [Slezak, Durret & Gerbal 1994] Slezak, E., Durret, F., Gerbal, D., 1994, *Astron. J.*, 108, 1996
- [Squires et al. 1996] Squires, G., Kaiser, N., Babul, A., Fahlman, G., Woods, D., Neumann, D. M., Böhringer, H., 1996, *Astrophys. J.*, 461, 572
- [Stark et al. 1992] Stark, A. A., Gammie, C. F., Wilson, R. W., Bally, J., Linke, R. A., Heiles, C., Hurwitz, M., 1992, *Astrophys. J. Suppl.*, 79, 77
- [Struble & Rood 1987] Struble, M. F., Rood, H. J. 1987, *Astrophys. J. Suppl.*, 63, 555
- [Struble & Rood 1991] Struble, M. F., Rood, H. J. 1991, *Astrophys. J. Suppl.*, 77, 363
- [Sunyaev & Zel'dovich 1981] Sunyaev, A. R. & Zel'dovich, Y. B., 1981, *Astrophys. Space Sci. Rev.*, 1, 1
- [Suto, Sugimotohara & Inagaki 1995] Suto, Y., Sugimotohara, T., Inagaki, Y., 1995, *Prog. Theor. Phys.*, 93, 839
- [Tammann et al. 1996] Tammann, G. A., Labhardt, L., Federspiel, M., Sandage, A., Saha, A., Macchetto, F. D., Panagia, N., 1996, *Proc. of Science with the Hubble Space Telescope - II* in press
- [Tanaka, Inoue & Holt 1994] Tanaka, Y., Inoue, H., Holt, S. S., 1984, *Publ. Astron. Soc. Japan*, 46, L37